Luís A. Fernandes

Birefringence and Bragg grating control in femtosecond laser written optical circuits

Departamento de Física e Astronomia
da Universidade do Porto
2012

Luís A. Fernandes

Birefringence and Bragg grating control in femtosecond laser written optical circuits

Tese submetida à Faculdade de Ciências da Universidade do Porto para obtenção do grau de Doutor em Física

Departamento de Física e Astronomia
da Universidade do Porto
2012

Aye, I suppose I could stay up that late.
James Clerk Maxwell, on being told on his arrival at Cambridge University that there would be a compulsory 6 a.m. church service.

Acknowledgments

The time I spent pursuing a Doctor of Philosophy (PhD) degree in physics together with all the rest of my academic life at the University of Porto did not fall short of the great adventure I always dreamed that it would be, and it was much, much more!

So many memories with friends and colleagues, so many happy moments. The long days and the countless hours studying and working in the lab may be coming to an end (and perhaps the hours will remain), but I will miss my student years, and I will always cherish this amazing part of my life.

I would like to thanks all the people that helped shape my PhD work, as well as my own philosophy as a researcher:

First of all, I would like to express my greatest gratitude to my supervisor, Prof. Paulo V. S. Marques from the Faculdade de Ciências da Universidade do Porto (FCUP), for all of his support and advice that was key for the success of my PhD work. His dedication to the fulfillment of my goals was beyond his duty, his guidance and friendship were a constant source of inspiration, and the opportunities he gave me were my motivation to learn and achieved more than I ever imagined.

To Prof. J. Stewart Aitchison and Prof. Peter R. Herman for welcoming me in the Photonics group of the University of Toronto throughout most of my PhD work. Their experience and knowledge taught me a lot over the past three years, and their constant challenging discussions and comments made me achieve my potential and develop all the skills I learned under their guidance. All that I accomplished in my PhD would not have been possible without them.

To Prof. António Pereira Leite for all his support to my various projects, for the amazing optics classes and great discussions that taught me so much, and were ultimately responsible for my decision to pursue a research career in photonics.

To Prof. José Luís Santos for his dedication to all his students and for all the opportunities he gave me. To Prof. Bessa Sousa, Prof. Carla Rosa, Prof. Carlos Herdeiro, Prof. David Schmool, Prof. João Pedro Araújo, Prof. Luís Bernardo, Prof. Manuel Joaquim Marques, Prof. Maria Augusta Santos, and all the other professors at the Department of Physics for being such great teachers and for sharing their passion for science with me.

From INESC Porto, to Orlando Frazão and our collaborators from the Institute of Photonic Technology (IPHT) in Jena, Germany, Manfred Rothhardt, Sven Brückner, Kay Schuster, Jens Kobelke, Hartmut Bartelt and specially Martin Becker, for our work in suspended core fibers in my visit to Jena in 2009 under the COST 299 project. To Daniel Alexandre and Askari Ghasempour for all they taught me ever since I started working in my final year undergraduate project. To Ireneu Dias who supervised the year I joined INESC Porto - UOSE as young researcher and patiently walked me through the very beginning of my career. To all my friends and colleagues at INESC

Porto, namely Jaime Viegas, Joel Carvalho, Paulo Moreira, Susana Silva, and Luísa Mendonça for their support, friendship and for making the graduate students office such a better place to work.

From the photonics group and the University of Toronto, to Jason Grenier, who worked with me in all my projects since I arrived in Toronto in 2009. Our collaboration in the fabrication of Bragg gratings with phase shifts prompted major breakthroughs in both our research areas. His friendship and wisdom was a constant source of counsel and I achieved many of my goals thanks to him. I wish him and his newly wedded wife Tammy the best, in a long and happy life together. To Moez Haque for the countless hours spent working in the ultrafast lab, for the great discussions and research challenges, and for the multiple fun moments we shared in Toronto and at the numerous conferences we attended. To Ksenia Dolgaleva for all her advice and shared experience, and to our colleagues from the Institut National de la Recherche Scientifique (INRS) from Quebec, Canada, Antonio Malacarne, Pamela Tannouri, José Azaña and Roberto Morandotti, for the collaboration in the pulse shaping grating waveguides project. To Jianzhao Li, Stephen Ho, Michelle Xu, Mi Li Ng, Arash Joushaghani, Leon Yuan, Kyle Cheng, Kenneth Lee, Samira Karimelahi, Saeid Rezaei, Jason Ng, Chris Sapiano, Sean Wagner, Steven Rutledge, Dagmar Esser, Tina Weichelt, and all the graduate students at the Photonics group for the great, friendly environment, and for the shared learning that made us grow to be better scientists. To my students, Matin Esfahani, Jin Hee Kim, Tony Zhang, He Xu and Laura Shen, co-supervised between Jason Grenier and myself in Toronto, for the dedication they showed to their summer projects.

To all my friends from FCUP, Ricardo Silva, Julie Passos, Tiago Dinis, Diana Leitao, Sara Pinto, Arlete Apolinario and everyone who shared with me almost 10 years of university life.

I would also like to acknowledge the Fundação para a Ciência e Tecnologia for my doctoral fellowship (SFRH/BD/41743/2007) which made all my work for this thesis possible, and the SPIE - the international society for optics and photonics, for my Scholarship in Optical Science and Engineering in 2010.

To all my friends and family who are the best one could ask for. They are the reason for great joy every time I board a plane to go home.

Lastly, I would like to thank the most important people in my life, my parents and Joana, all their love and support made me what I am today.

Abstract

In this thesis, femtosecond lasers are explored for the fabrication of fiber Bragg gratings (FBGs) in suspended core fibers (SCFs) as well as direct writing of integrated optical devices in bulk fused silica glass.

The FBGs fabricated in suspended core fibers with different core geometries were demonstrated with femtosecond laser exposure through a Talbot interferometer. In this case, the use of a femtosecond laser system was crucial as it eliminates the need for the use of photosensitive fibers, which is the case for SCFs, while the Talbot interferometry setup provided flexibility in the definition of the grating periodicity, while simultaneously protecting the optical components used in the fabrication process from the high intensities reached during exposure in the proximity of the fibers. These Bragg gratings were employed to show simultaneous strain and temperature sensing.

Using a femtosecond laser direct writing system, novel point-by-point fabrication arrangements, with detailed attention to the computer controlled laser beam modulation, were developed in order to correctly introduce modulation of the refractive index profile during the waveguide fabrication process. This technique enabled the development of phase and frequency control required for advanced Bragg grating waveguide (BGW) fabrication and arbitrary spectral shaping. Procedures were demonstrated for the fabrication of chirped and phased shifted BGWs for applications in temporal pulse shaping and spectral shaping that showed significantly improved feature resolutions for sensing applications.

The BGWs were used as a practical sensitive tool to determine and study the waveguide birefringence inherent to the nonlinear absorption processes typical of femtosecond laser-material interaction. The control of form and stress birefringence was developed in order to accomplish the fabrication of integrated optical components for polarization control, like guided wave retarders and polarization beam splitters. Tuning of this waveguide birefringence was achieved by the introduction of stress inducing laser

modification tracks that enabled the ability to both enhance or reduce the inherent birefringence. Characterization techniques were developed for the absolute determination of the birefringence based on BGWs spectrum splitting, together with crossed polarizer measurements, while novel data analysis procedures were demonstrated for the study of polarization dependent and polarization independent directional couplers with the introduction of a polarization splitting ratio which is wavelength and coupling length dependent.

All of the improvements made in the understanding of waveguide birefringence control provided increased flexibility to simultaneously fabricate low polarization mode dispersion circuits, as well as more efficient and compact polarization dependent devices. The polarization aspects detailed here, together with the point-by-point fabrication system, may be further developed in the future towards the fabrication of more complex integrated devices that combine spectral, temporal, and polarization control, all achievable with the same femtosecond laser writing system. These flexible processing techniques will open new directions for writing additional functionalities in optical circuits with more compact three-dimensional geometries.

Resumo

Nesta tese, lasers de femtosegundos são explorados para a fabricação de redes de Bragg (*fiber Bragg gratings (FBGs)*) em fibras de núcleo suspenso (*suspended core fibers (SCFs)*) e para a escrita direta de dispositivos ópticos integrados em substratos de vidro compostos por sílica pura.

As redes de Bragg fabricadas em fibras de núcleo suspenso, com diferentes geometrias, foram demonstradas por exposição à radiação de um laser de femtosegundos através de um interferómetro de Talbot. Neste caso, a utilização de um sistema laser de femtosegundos foi crucial, uma vez que este elimina a necessidade de utilização de fibras fotossensíveis, que é o caso das fibras de núcleo suspenso, enquanto que a configuração interferométrica de Talbot proporciona flexibilidade na definição da periodicidade da rede, ao mesmo tempo que protege os componentes ópticos utilizados no processo de fabricação das intensidades elevadas atingidas durante a exposição, na proximidade das fibras. Estas redes de Bragg foram utilizadas para demonstrar medição simultânea de tensão e de temperatura.

Recorrendo a um sistema de escrita direta com laser de femtosegundos, novos processos de fabricação ponto-a-ponto, com especial destaque para o controlo computorizado da modulação do laser, foram desenvolvidos no sentido de introduzir modulação do perfil de índice de refracção durante o processo de fabricação de guias de onda. Esta técnica permitiu o desenvolvimento do controlo de fase e frequência necessários para a fabricação de redes de Bragg integradas (*Bragg grating waveguides (BGWs)*) com conteúdo espectral arbitrário. Os procedimentos foram demonstrados para a fabricação de redes de Bragg com saltos de fase (*phased shifts*) e com variação linear de frequência (*chirp*) e para aplicações em modulação temporal e espectral de impulsos, demonstrando também uma melhoria significativa da resolução para aplicações em sensores ópticos.

As redes de Bragg integradas foram utilizadas como ferramenta prática para a determinação e estudo da birrefringência em guia de onda, birrefringência esta que é inerente aos processos de absorção não-lineares típicos das interacções do laser de femtosegundos com vidros. O controlo da birrefringência de forma e de tensão foi desenvolvido no sentido de obter componentes ópticos integrados para o controle de polarização, como retardadores de onda e separadores de polarização baseados em acopladores direccionais. A variação da birrefringência dos guias foi conseguida através da introdução de zonas modificadas pelo laser criando estados de tensão localizada, permitindo o aumento ou redução da birrefringência. Técnicas de caracterização foram desenvolvidas para a determinação precisa e única da birrefringência com base na degenerescência espectral do modo fundamental das redes de Bragg juntamente com medições de polarização cruzada, ao mesmo tempo que novos procedimentos de análise de dados foram demonstrados para o estudo de acopladores direccionais, com e sem dependência na polarização, através da introdução de uma razão de divisão de polarização (*polarization splitting ratio*), que depende do comprimento de onda e do comprimento da região de acoplamento.

Todo o progresso feito na compreensão de formas de controlo da birrefringência em guias de onda integrados forneceram uma maior flexibilidade do sistema para a fabricação em simultâneo de dispositivos com pouca dispersão modal de polarização, assim como de dispositivos dependentes de polarização mais compactos e eficientes. Os aspectos de polarização em guias de onda aqui descritos, em conjunto com o sistema de fabricação ponto-a-ponto de redes de Bragg, podem ser desenvolvidos no futuro para a fabricação de dispositivos integrados mais complexos que combinam controlo espectral, temporal e de polarização, todos atingíveis com o mesmo sistema de escrita direta com laser de femtosegundos. Estas técnicas de processamento flexíveis proporcionarão novas direções para a escrita de dispositivos com funcionalidades adicionais em circuitos ópticos mais compactos e em geometrias tridimensionais.

Contents

List of Tables

List of Figures

List of Equations

List of Publications

Refereed Journals:

Luís A. Fernandes, J. R. Grenier, P. R. Herman, J. S. Aitchison and P. V. S. Marques, "Stress induced birefringence tuning in femtosecond laser fabricated waveguides in fused silica," *Optics Express*, Vol. **20,** Issue 22, pp. 24103-24114, 2012

J. R. Grenier, **Luís A. Fernandes**, J. S. Aitchison, P. V. S. Marques, P. R. Herman, "Femtosecond laser fabrication of phase-shifted Bragg grating waveguides in fused silica," *Optics letters*, Vol. **37,** Issue 12, pp. 2289-2291, 2012

Luís A. Fernandes, M. Becker, O. Frazao, K. Schuster, J. Kobelke, M. Rothhardt, H. Bartelt, J. L. Santos and P. V. S. Marques, "Temperature and Strain Sensing With Femtosecond Laser Written Bragg Gratings in Defect and Non-Defect Suspended-Silica-Core Fibers," *IEEE Photonics Technology Letters*, Vol. **24,** Issue 7, pp. 554-556, 2012

Luís A. Fernandes, J. R. Grenier, P. R. Herman, J. S. Aitchison and P. V. S. Marques, "Femtosecond laser writing of waveguide retarders in fused silica for polarization control in optical circuits," *Optics Express*, Vol. **19,** Issue 19, pp. 18294-18301, 2011

K. Dolgaleva, A. Malacarne, P. Tannouri, **Luís A. Fernandes**, J. R. Grenier, J. Aitchison, J. Azana, R. Morandotti, P. R. Herman and P. V. Marques, "Integrated Optical Temporal Fourier Transformer Based on Chirped Bragg Grating Waveguide," *Optics Letters*, Vol. **36,** Issue 22, pp. 4416-4418, 2011

Luís A. Fernandes, J. R. Grenier, P. R. Herman, J. S. Aitchison and P. V. S. Marques, "Femtosecond laser fabrication of birefringent directional couplers as polarization beam splitters in fused silica," *Optics Express*, Vol. **19,** Issue 13, pp. 11992-11999, 2011

M. Becker, **Luís A. Fernandes**, M. Rothhardt, S. Brückner, K. Schuster, J. Kobelke, O. Frazão, H. Bartelt and P. V. S. Marques, "Inscription of Fiber Bragg Grating Arrays in Pure Silica Suspended Core Fibers," *IEEE Photonics Technology Letters*, Vol. **21,** Issue 19, pp. 1453-1455, 2009

International conferences:

J. R. Grenier, **Luís A. Fernandes**, P. V. S. Marques, J. S. Aitchison and P. R. Herman "Femtosecond Direct Laser Writing of Fiber Cladding Photonic Devices," Oral presentation, OPTICS-6-19-4, SPIE: Non-linear optics and photonic materials, Photonics North, 2012

Luís A. Fernandes, J. R. Grenier, P. R. Herman, J. S. Aitchison and P. V. S. Marques, "Femtosecond laser writing of polarization devices for optical circuits in glass," Proc. SPIE 8247, 82470M, SPIE LASE: Frontiers in Ultrafast Optics: Biomedical, Scientific, and Industrial Applications XII, Photonics West, 2012

J. R. Grenier, **Luís A. Fernandes**, P. V. S. Marques, J. S. Aitchison and P. R. Herman, "Femtosecond laser fabrication of optical sensing devices in the cladding of optical fibers," Oral presentation, 8247-33, SPIE LASE: Frontiers in Ultrafast Optics: Biomedical, Scientific, and Industrial Applications XII, Photonics West, 2012

M. Haque, J. R. Grenier, S. Ho, **Luís A. Fernandes**and P. R. Herman, "Femtosecond direct writing of lab-on-a-fiber optofluidic sensors," Oral presentation, 8247-31, SPIE LASE: Frontiers in Ultrafast Optics: Biomedical, Scientific, and Industrial Applications XII, Photonics West, 2012

Luís A. Fernandes, J. R. Grenier, J. H. Kim, P. R. Herman, J. Aitchison and P. V. Marques, "Femtosecond laser direct fabrication of integrated optical wave plates in fused silica," Oral presentation in CLEO:2011 - Laser Applications to Photonic Applications, paper CWO6, 2011

J. R. Grenier, **Luís A. Fernandes**, P. V. Marques, J. Aitchison and P. R. Herman, "Optical Circuits in Fiber Cladding: Femtosecond laser-written Bragg Grating Waveguides," Oral presentation in CLEO:2011 - Laser Applications to Photonic Applications, paper CMZ1, 2011

K. Dolgaleva, A. Malacarne, P. Tannouri, **Luís A. Fernandes**, J. R. Grenier, J. Aitchison, J. Azana, R. Morandotti, P. R. Herman and P. V. Marques, "Integrated Temporal Fourier Transformer Based on Chirped Bragg Grating Waveguides," Oral presentation in CLEO:2011 - Laser Applications to Photonic Applications, paper CThHH6, 2011

Luís A. Fernandes, J. R. Grenier, P. R. Herman, J. S. Aitchison and P. V. S. Marques, "Femtosecond laser fabrication of birefringent directional couplers in fused silica," Oral presentation, SPIE, Photonics West Conference, 2010 [Received one Student Award for best oral presentations]

J. R. Grenier, **Luís A. Fernandes**, M. Esfahani, J. S. Aitchison, P. V. S. Marques and P. R. Herman, "Flexible tailoring of femtosecond laser-written Bragg grating waveguides," Oral presentation, SPIE, Photonics West Conference, 2010

Luís A. Fernandes, J. R. Grenier, P. R. Herman, J. S. Aitchison and P. V. S. Marques, "Femtosecond Laser Writing of Phase-Shifted Bragg Grating Waveguides in Fused Silica," Oral presentation in Femtosecond Laser Microfabrication, OSA Frontiers in Optics, paper LMTuC5, 2009

Luís A. Fernandes, M. Becker, O. Frazão, M. Rothhardt, S. Brückner, K. Schuster, J. Kobelke, J. L. Santos and P.V.S. Marques, "Temperature and strain characterization of Bragg gratings impressed with femtosecond laser radiation in suspended-silica-core fibers," Proc. SPIE 7386, 73861N, SPIE Photonics North, 2009

M. Becker, J. Bergmann, S. Brückner, E. Lindner, M. Rothhardt, K. Schuster, J. Kobelke, S. Unger, H. Bartelt, **Luís A. Fernandes** and P. V. S. Marques "Fiber Bragg grating inscription with DUV femtosecond exposure and two beam interference," Proc. SPIE 7386, 73862Y, SPIE Photonics North, 2009

Other papers and contributions:

Luís A. Fernandes, J. R. Grenier, P. R. Herman, J. S. Aitchison and P. V. S. Marques, "Escrita de dispositivos ópticos integrados com laser de femtosegundos," *Gazeta de Física*, Vol. **34,** n 1, pp. 17-21, 2011

Luís A. Fernandes, Jason R. Grenier, Peter R. Herman, J. S. Aitchison and Paulo V. S. Marques, "Femtosecond Laser Writing Of Polarization Devices For Optical Circuits In Glass," Oral presentation in Connections 2012, University of Toronto ECE Graduate Symposium, May, 2012

Jason R. Grenier, **Luís A. Fernandes**, Paulo V. S. Marques, J. Stewart Aitchison and Peter R. Herman, "Ultrafast Laser Fabrication of Optical Fiber Sensors," Oral presentation in Connections 2012, University of Toronto ECE Graduate Symposium, May, 2012

Luís A. Fernandes, Jason R. Grenier, Peter R. Herman, J. S. Aitchison and Paulo V. S. Marques, "Femtosecond laser direct writing of integrated polarization dependent devices," Oral presentation in Connections 2011, University of Toronto ECE Graduate Symposium, May, 2011

Jason R. Grenier, **Luís A. Fernandes**, Paulo V. S. Marques, J. Stewart Aitchison and Peter R. Herman, "Laser Fabrication of Lab-on-a-fiber devices," Oral presentation in Connections 2011, University of Toronto ECE Graduate Symposium, May, 2011

Luís A. Fernandes, J. R. Grenier, P. R. Herman, J. S. Aitchison and Paulo Vicente Marques, "Escrita Directa Ponto-a-ponto de Redes de Bragg com Impulsos Laser Ultracurtos," Oral presentation in Física 2010, Vila Real, Portugal, September, 2010

Jason R. Grenier, **Luís A. Fernandes**, Paulo V. S. Marques, J. Stewart Aitchison and Peter R. Herman, "Laser Fabrication of Optical Circuits," Oral presentation in Connections 2010, University of Toronto ECE Graduate Symposium, May, 2010

Glossary

Gaussian A Gaussian function is defined by Equation 0.1, with x_0 being the position of the peak and the value at the maximum point is $G(x_0) = A$.

$$G(x) = Ae^{-\frac{(x-x_0)^2}{2c^2}} \tag{0.1}$$

The diameter at $1/e^2$ of the maximum is $2\omega_0 = 4c$ and the full width at half maximum (FWHM) is $2\sqrt{2\ln 2}c$. 43, 46, 53

GPIB General Purpose Interface Bus, IEEE-488, is a digital communication bus specification. It is used for computer control of many laboratory equipment. 50, 141

hyperbolic secant squared The hyperbolic secant squared (sech^2) function is defined by Equation 0.2, with x_0 being the position of the peak.

$$S(x) = A\ \text{sech}^2\left(\frac{(x-x_0)}{\tau}\right) \tag{0.2}$$

The value at the maximum point is $S(x_0) = A$ and the FWHM is given by $2\ln(\sqrt{2}+1)\tau \approx 1.76\tau$. 43

Levenberg-Marquardt The Levenberg-Marquardt algorithm is a numerical method that provides a solution to the problem of minimizing a nonlinear function over a space of parameters of that function [1, 2]. In this thesis the python implementation of this algorithm from the SciPy module was used. 106, 141

Lorentzian A Lorentzian function is defined by Equation 0.3, with x_0 being the position of the peak.

$$L(x) = \frac{A}{\pi} \frac{\frac{1}{2}\Gamma}{(x - x_0)^2 + (\frac{1}{2}\Gamma)^2} \tag{0.3}$$

The value at the maximum point is $L(x_0) = \frac{A}{\pi\Gamma}$ and the FWHM is given by Γ . 42, 43

retardance Also known as the relative retardation, is the phase difference accumulated between two polarization eigenmodes in a given length of a birefringent material. The linear retardation, measured in units of length, corresponds to the difference between the space the two eigenmodes propagate in the same time through a given length of a retardance medium [3]. 93

Acronyms

ACF autocorrelation function. 42, 43

AOM acousto-optic modulator. 43–45, 74, 75, 77–79, 84, 89, 93, 105, 113, 117, 128

ArF argon fluoride. 59

ASE amplified spontaneous emission. 50, 118

BGW Bragg grating waveguide. 9–11, 41, 50, 54, 56, 73–82, 84, 85, 87–89, 93, 94, 96–99, 105, 106, 110, 111, 113–124, 127, 128, 131–134

CCD charge-coupled device. 52, 96

CL coupling loss. 53

CW continuous wave. 34

DFB distributed feedback laser. 73

DUV deep ultra violet. 57, 59–61, 63

EELED edge-emitting LED. 50

FBG fiber Bragg grating. 9, 11, 42, 57, 58, 60–64, 66–69, 71, 73, 75, 76, 127

FTSI fourier transform spectral interferometry. 82, 83

FWHM full width at half maximum. 25, 26, 42, 43, 77

HF hydrofluoric acid. 36

IPA isopropyl alcohol. 67–70

KOH potassium hydroxide. 36

LBO lithium triborate. 45

MFD mode field diameter. 52, 53, 96, 97, 102, 104, 113, 115–118

NA numerical aperture. 38, 46, 48, 49, 55, 56, 93, 94, 104, 105, 113

OBPF optical bandpass filter. 82, 83

OD optical density. 48

OSA optical spectrum analyzer. 39, 50, 51, 85, 87, 94, 95, 105, 118, 131, 133

PCF photonic crystal fiber. 38, 58

PSBGW phase shifted Bragg grating waveguide. 84–88

PSO position-synchronized output. 74, 84

SCF suspended core fiber. 9, 11, 57, 58, 60–62, 65, 66, 68, 71, 127

SMF single mode fiber. 38, 52, 53, 60, 96, 113, 117

UV ultraviolet. 38

voxel volumetric pixel. 44, 74, 75

WDM wavelength division multiplexing. 103, 125

Introduction

The development of fabrication processes compatible with a high degree of miniaturization has been pursued for decades for applications in many different areas of scientific knowledge. Since the invention of the laser, the use of these radiation sources has been key for many micro-fabrications processes, with special interest in direct laser writing of devices. Recent progress in pulsed ultrafast lasers has been responsible for a great number of fabrication applications that rely on sub-micrometer resolutions achievable with these systems, as well as the ability to perform direct three-dimensional fabrication of optical devices.

Society relies heavily on optical technologies for many aspects of human life. Today's information is transported around the world by optical fibers, from the long transatlantic backbones to home installations in some regions of the globe. Besides being the main channel for communications, optical fibers are also used for many sensor applications, such as distributed stress and temperature detection, image collection and chemical and environmental monitoring, to name a few.

While optical fibers have become arguably the main component for the world's communication infrastructure, integrated optical devices have also found many important applications, bringing together the advantages provided by optical sensing and optical processing technologies, with the compactness and reliability of miniaturized integrated systems.

Beyond passive optical components, active devices have also provided a huge thrust to science and technology since the theoretic foundation of *light amplification by stimulated emission of radiation* was proposed by Albert Einstein in 1917. This was followed with efforts by many researchers that culminated in the demonstration of the first laser in 1960. Lasers became the ideal source of energy for many applications such as: industrial material processing, where lasers are used for cutting, welding, marking, and cleaning of various materials; scientific experiments in spectroscopy and

interferometry for all kinds of accurate measurements, from astronomical distances to microscopic scale sizes; medical applications such as cancer treatment, eye and cosmetic surgery and as a cutting tool for general surgery; and many others where the characteristics of light coherence or the ability to create high optical intensities makes the laser impossible to replace by any other kind of tool.

Photonics technologies have many advantages when compared to other sensing and communication methods. For example, all-optical components have the advantage of being ideal to deploy in environments typically hazardous to electronic equipment. Their immunity to electromagnetic interference makes them suitable for use in high power environments while the robustness of the platforms makes them great for withstanding extreme pressures, like deep water explorations, or extreme heat environments. With the choice of appropriate dielectric materials, integrated optical devices can be used in situations of exposure to considerable amounts of ionizing radiation, such as space stations, satellites or nuclear plants. The stability and performance of current integrated optical devices also provides an ideal platform to be used in quantum optics experiments, opening opportunities for the design of quantum entanglement cryptography applications or quantum bit processing on a chip. The fabrication of devices for these applications requires very deep knowledge of light-matter interactions, as well as exploration of materials, fabrication techniques and optical circuits design to fully achieve the possibilities of this technology.

The photonic science and technology available today already appear in a great part of everyday life and yet there are endless opportunities to explore and expand further the applications of optical devices. Areas such as medicine, communications and industrial processing can readily benefit from better devices with faster components, increased functionality or simpler manufacturing techniques that provide lower costs. Other possibilities such as integrated optical computers, based on optical processors, are still far from being available, yet their discovery and demonstration may very well represent a paradigm shift in information technology, for the new possibilities that may become available.

Femtosecond laser technologies have enabled the prospects of producing integrated optical circuits in three dimensions with a single writing step [4, 5, 6]. Fused silica is a widely favored material in femtosecond laser processing due to formation of low loss and stable optical devices.

Since the discovery of induced refractive index modification of transparent material with femtosecond laser exposure [7], many devices have been demonstrated, including directional couplers [6], Bragg grating waveguides [8], waveguides in active materials [9], and integrated lasers [10]. This method of forming waveguides opens up the prospects of producing three-dimensional integrated optical circuits in a single writing step [4, 5] like three-by-three directional couplers [11], or for high density volume data storage [12].

This thesis is focused on the study and fabrication of new optical circuits and devices within the current framework of optical ultrafast fabrication and characterization technologies, taking advantage of scientific knowledge about nonlinear light-matter interaction, waveguides, and integrated optics design. The focus is on bulk fused silica glass as the material of choice for creating optical devices with good optical properties. Advances in point-by-point writing of segmented waveguides are explored for application in spectral shaping and high resolution sensing, while interferometric femtosecond fabrication is used for the development of Bragg gratings in pure silica optical fibers for temperature and strain sensing. In addition, new approaches to control waveguide birefringence are presented towards the fabrication of polarization dependent spectrally selective components. Together, segmented waveguides and polarization components define the thesis objective of improving the state-of-the-art of optical circuits with new advanced fabrication control processes.

Chapter 1

Background

Ultrafast laser pulses with durations on the order of hundreds of femtoseconds (fs) to picoseconds (ps) and with pulse energies of hundreds of nanojoules (nJ) can reach peak powers on the order of megawatts (MW). If pulses with such high peak power are tightly focused onto micrometer square (μm^2) size areas, the intensity on the focal spot can reach terawatts per centimeter square (TW/cm^2) [1]. If the laser pulses are focused below the surface of a transparent dielectric material, these intensity levels are sufficient to trigger nonlinear optical absorption through processes that are not yet completely understood, but can generally be simplified into the generation of a free electron plasma by multiphoton ionization [13, 14] and avalanche photoionization [15, 16], and energy relaxation followed by permanent modification of the material properties. With appropriate laser and focusing conditions, this permanent modification may provide an increase in the refractive index of the material [7]. The refractive index changes inside glasses can result from chemical alterations after plasma formation or from the generation of low and high densification zones and stress fields in the material.

The nonlinear absorption process in dielectric materials enables the possibility of writing modification regions directly inside these transparent materials, which further enables fabrication of three dimensional integrated optical circuits [17]. The development of ultrafast pulsed lasers, with pulse widths of sub-picosecond dimension, was a key factor for the introduction of high resolution three dimensional micro-machining processes that take advantage of nonlinear light-matter interaction.

[1] For perspective, the average lightning strikes have peak powers of terawatts.

If a high peak power ultrashort pulse is focused inside a transparent material, the light intensity necessary to produce these effects is only reached in the focal volume of the beam [16], as represented in Fig. 1.1 by the comparison between a continuous wave (CW) laser in a linear absorption medium and a pulsed laser in a transparent medium. This nonlinear absorption enables the ability to directly define three dimensional circuits [18] inside a transparent substrate. In contrast, the standard photolithography methods rely on linear absorption of radiation in a photosensitive material, when the emission wavelength of a laser is in resonance with an absorption band of that material, and this process is typically restricted to two dimensional fabrication.

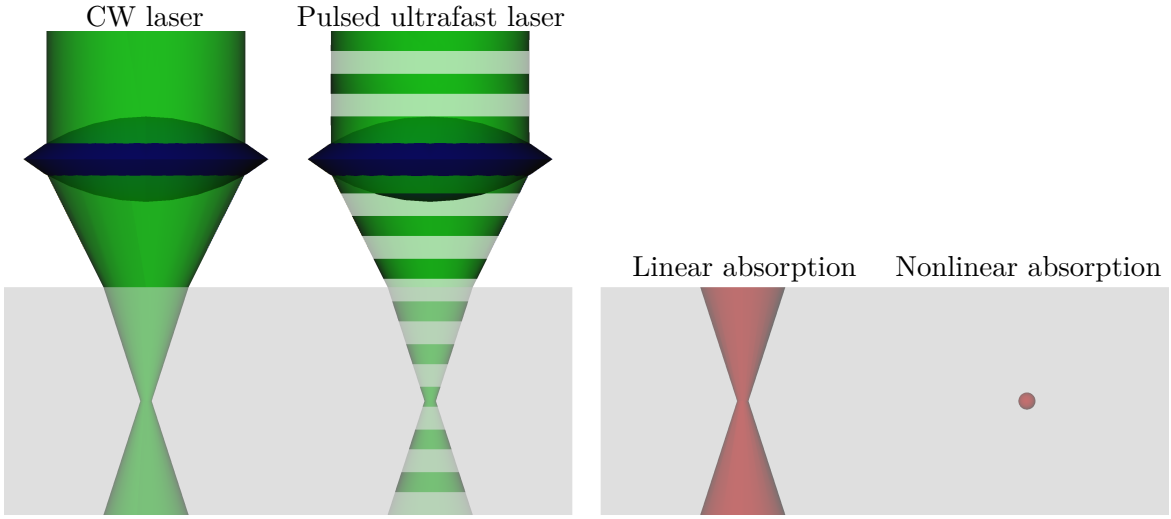

Figure 1.1: Comparison between linear absorption, produced by a CW laser (or long pulsed light source) in a photosensitive material, and nonlinear absorption produced by an ultrafast laser focused in a transparent material.

In a similar way, fabrication in photosensitive materials can also benefit from ultrafast laser fabrication. The chemical alteration required for the process of photopolymerization can happen nonlinearly if the wavelength used is not linearly absorbed by the material. This approach can reduce the resolutions to values under the diffraction limit [19]. This high resolution selective photopolymerization can be used for the fabrication of photonic band gap devices (or photonic crystals) with tens of nanometers size features. These devices can exhibit a photonic stop band, analogous to the electronic band gap present in semiconductors; however, for this effect to occur, the photonic crystals structure requires a high index contrast, which is seldom the case for polymers. Nanostructures fabricated this way can, instead, be used as a template for the replication of the structures with higher index of refraction materials, like silicon,

by methods of double inversion (or simple inversion in case the template is the negative of the desired structure) [20].

Ultrafast lasers suitable for waveguide fabrication can be classified according to their pulse energy and repetition rate. High repetition oscillators, with rates typically around 80 MHz, provide per pulse energies on the order of nanojoules to tens of nanojoules, while high power amplifiers can reach hundreds of milijoules of energy per pulse with repetition rates on the order of kilohertz to hundreds of kilohertz[2]. High repetition rate systems have a time period between pulses which is shorter than the thermal dissipation time for many glasses. This may produce thermal accumulation effects [21] which produce volumes larger than the focal volume of the laser [22], a beneficial effect that has been explored to fabricate low loss waveguides [23]. In contrast, the low repetition rate systems may be viewed as single isolated pulses arriving at the sample and hitting "cold material," where all effects from previous laser pulses at the focal volume are negligible when the next pulse arrives. The high energy per pulse available with these lasers triggers higher nonlinear effects that are not reachable with high repetition rate, low energy systems, making them also useful for waveguide writing, as well as micro fabrication by glass ablation [24], hole drilling [25, 26] or glass cutting [27, 28].

A demonstration of the capabilities of ultrafast laser writing is shown in Fig. 1.2. The logos of the University of Toronto and INESC Porto were imprinted 10 µm under the surface of a fused silica substrate without any modification to the surface of the glass.

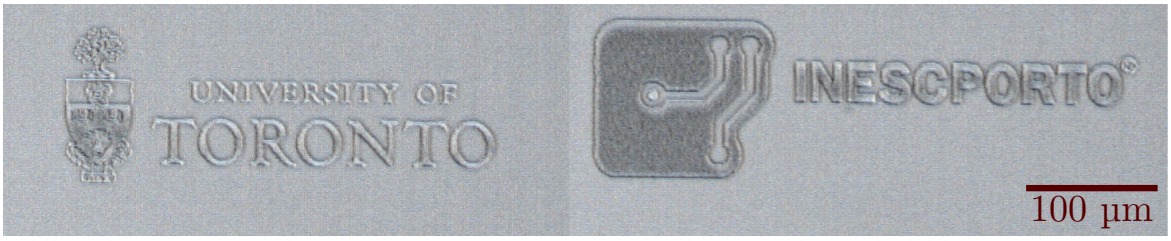

Figure 1.2: Optical microscope image of the logos of the University of Toronto and INESC Porto, written by femtosecond laser exposure 10 µm under the surface of a fused silica substrate.

A common solid state femtosecond laser system approach is based on a Ti:sapphire gain medium (due to the large gain bandwidth required for ultrashort pulses), typically emitting on the near infrared spectral band (800 nm - 1000 nm) that can be used with

[2]A high pulse energy, low repetition rate laser was used in Chapter 3 to make fiber Bragg gratings in suspended core fibers.

a mode locked oscillator to produce high repetition rate lasers with low power. These lasers can serve as a seed source for a chirped pulse amplification [29] stage, where a regenerative amplifier cavity, for example, also using a Ti:sapphire gain medium, is used to increase the pulse energy at the expense of producing a beam at a lower repetition rate, resulting in the high power, low repetition rate laser systems mentioned earlier.

Another approach to produce ultrafast laser pulses has been greatly developed in the last decade, and is based on using rare earth (mainly ytterbium) doped fiber laser systems emitting at 1044 nm. These lasers can provide various combinations of repetition rates and pulse energies, and have the advantage of being more stable than their solid state counterparts. This particular advantage is a key factor for waveguide writing, where the quality of the optical circuits is greatly influenced by the stability of the laser source. Particularly for prototyping experiments and basic interaction studies, a stable laser allows for more precise probing of device parameters that influence the quality of the integrated optical circuits[3].

The material of choice for optical applications is fused silica due to its high transparency to optical wavelengths and also due to its stable physical properties, such as temperature and chemical stability and durability. Fused silica is transparent to the laser wavelengths typically available from ultrafast lasers and thus meets the criteria for nonlinear absorption process in the laser focal volume, enabling the fabrication of waveguides. A summary of fused silica properties relevant for optical applications is given in Appendix B.

Fused silica is also chemically stable and does not react with most acid or organic solvents. One exception is hydrofluoric acid (HF) acid, for example, which can dissolve fused silica. While this may be a challenge if an application requires devices to be HF resistant, it also provides an opportunity for microfluidic channel fabrication [30, 31] and their combination with integrated optical components. The structural changes created in fused silica by ultrafast laser exposure greatly enhance the susceptibility of the glass to HF etching, making possible the selective patterning of bulk glass and fabrication of microfluidic channels. Hence, the same laser can be used for waveguide and microfluidic fabrication. Solutions such as potassium hydroxide (KOH) are also capable of selectively etch femtosecond laser patterned fused silica [32] with better aspect ratio and without significant saturation as compared with HF.

[3] A fiber laser was the basis for all the fabrication work presented in Chapter 4 and Chapter 5 to make waveguides in bulk fused silica glass.

The mechanism for selective chemical etching is influenced by the creation of nanogratings (shown in Fig. 1.3) in the focal volume of an ultrafast laser as well as the amount of energy deposited in the glass [33]. The phenomenon of nanograting formation is present in fused silica as well as in other glasses and consists of periodic nano-structures with sizes smaller that the wavelength of the laser, that are formed perpendicular to the laser polarization.

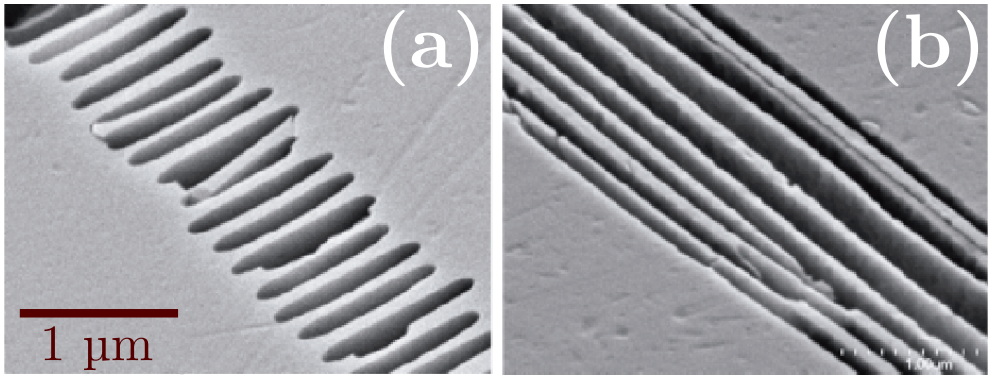

Figure 1.3: Scanning electron microscope image of nanogratings oriented perpendicularly (a) and parallel (b) to the waveguide direction [34, 35].

Many materials, besides fused silica, have been explored for waveguide laser writing. Borosilicate glass, for example, has shown great potential by exhibiting thermal accumulation effects with moderate repetition rates of hundreds of kilohertz, leading to low loss waveguides [23]. Such heat accumulation effects have not been advantageously demonstrated in femtosecond laser writing of waveguides in fused silica. Rare earth doped glasses have been explored for direct fabrication of laser cavities [10], while the fabrication of waveguides in crystals has also been explored [36, 37, 38]; however, in this case, femtosecond laser exposure typically reduced the refractive index of the material, rather than increasing it like in glasses. This is a challenge that has been addressed by the fabrication of depressed claddings [39], in order to outline a pattern for waveguide operation. All the currently available fabrication techniques, together with the improvements favored by ultrafast laser technology, provide an excellent framework for lab-on-a-chip device fabrication [40]. Another advantage of fused silica is that after fabrication the samples do not require grinding and polishing to provide good coupling of light into the waveguide. Other, lower fusion temperature glasses suffer from waveguide tapering at the edges of the glass substrate, where the laser beam is asymmetrically focused passing partially through the surface and partially through air. This effect is negligible in fused silica, which provides for faster fabrication and testing cycles to be performed by eliminating the time consuming polishing step.

Another aspect worth noting is the possibility of self focusing [14, 41], which in practice produces a focal volume inside the glass that is closer to the writing lens than if linear propagation alone is considered. Furthermore, this shift in the focus position depends on the writing power and the numerical aperture (NA) of the focusing lens and this effect has to be taken into account when designing three dimensional structures at different depths.

The laser fabrication of structures, being microfluidics or waveguides, has also found application in optical fibers, where the availability of substrates and their flexibility provides the perfect platform for distributed sensing. Standard single mode fiber (SMF) have the core made of germanium doped fused silica which adds a 0.36% refractive index increase to the background fused silica cladding. The doped core can be photosensitive to ultraviolet (UV) radiation but is still transparent at longer wavelengths. At the same time, other types of fibers, such as photonic crystal fibers (PCFs), have no doped core and are therefore good candidates for femtosecond laser writing. Both standard or micro-structured fibers can also take advantage of ultrafast laser writing to develop optical devices in the cladding of those fibers. This approach promises to greatly enhance the availability of devices towards the fabrication of lab-on-a-fiber systems.

Both lab-on-a-fiber and lab-on-a-chip devices present fabrication challenges, ranging from the availability of reliable and flexible laser sources to understanding the theories governing the nonlinear absorption phenomena. Further developments in these areas promise to generate new opportunities for applications in optical telecommunications, distributed or in-situ sensing, in-vivo biophotonics sensing, and quantum optics.

1.1 Challenges and opportunities

Due to the nonlinear nature of ultrafast light-matter interactions, many parameters that influence experimental results quickly become very complex and complicated to analyze or to isolate clean-cut relationships between the exposure conditions and the resulting modification structures.

An example of this complexity can be found in the formation of nanogratings, which happen in a select number of materials. The nanogratings provide selective etching, influence the waveguide losses and also, due to their orientation, may produce form birefringence, which is the topic of Chapter 5 of this thesis.

Generic asymmetries in the laser beam focus have been found to create regions of low and high refractive index, which in turn create stressed material around the focal volume [42]. These stressed regions, combined with the presence or absence of heat accumulation, lead to birefringence in the sample that depends primarily on the writing laser pulse energy. The power distribution or the presence of spatial chirp in the writing laser beam has also been shown to be a source of non-reciprocal writing [43], commonly called the "quill effect." This effect creates waveguides with optical properties that depend on the writing direction, i.e., on the relative positions of the laser to the glass and on the writing direction. This effect, while non-negligible, can be circumvented by choosing a writing configuration and direction that provides relatively good propagation properties for a waveguide and then exploring other parameters without changing the "quill effect" condition[4]. Most of the experiments in this thesis do not address the "quill effect" as processes and devices were selectively written in only one direction where the "quill effect" was constant across all devices studied. It was found that while absolute values may not be the same, the trends between fabrication conditions and waveguide properties are generally the same regardless of this non-reciprocal effect.

Nearly all the writing parameters such as pulse energy, writing speed, writing wavelength, pulse duration, focusing and material properties, will greatly influence the waveguide properties, such as propagation loss, mode field distribution, and birefringence with wavelength dependency. This can be turned into an opportunity to control the spectral properties of the fabricated devices where their wavelength dependent properties are easy to be recorded with broadband sources and optical spectrum analyzers (OSAs), providing another dimension of experimental results which can offer a great amount of information about the writing process.

These technical fabrication aspects are a challenge to produce waveguides with high repeatability and predictability of their optical properties. Because many of these issues remain fairly unexplored, they constitute a big study opportunity that can offer on one hand a deeper understanding of nonlinear light-matter interaction, and at the same time the possibility of exploring these properties in the implementation of new kinds of integrated optical devices.

[4]While this approach is suitable for prototyping experiments and novel demonstrations, future reproducibility of results is subject to the reproduction of the original laser condition that replicates the effect.

Chapter 2

Fabrication and characterization methods

This chapter describes the methods used for the fabrication and characterization of waveguides produced using femtosecond laser exposure. Most of the contents of this thesis, with the exception of Chapter 3, rely on these experimental procedures specifically applied to planar fused silica glass substrates. The femtosecond laser described in Section 2.1 has characteristics, like pulse duration and energy per pulse, ideal to produce nonlinear absorption in glasses and therefore to produce the required permanent changes in the substrate that make the definition of waveguides possible. These specifications are in the range between the required intensity[1] threshold for nonlinear absorption and the intensity threshold for damage and ablation. Additional components in the laser delivery system, also described in Section 2.1, further allow for the manipulation of the femtosecond laser beam to facilitate the fabrication of segmented waveguides and to obtain Bragg grating waveguides (BGWs). The characterization methods described in Section 2.2 provide the means to measure the key physical quantities of the femtosecond laser written waveguides with sufficient accuracy to draw meaningful conclusions from the experiments designed in each chapter.

[1] The peak power achievable from this laser is the important parameter to consider (which depends on the energy per pulse and the pulse duration). The intensity thresholds are reached after the laser is focused inside the material, so the intensity depends also on the focusing power used for this purpose; however, the focusing is limited by diffraction, and in practice, under the conditions explained later in this chapter, spot sizes of $\approx 1\,\mu m$ are the smallest achievable here for practical waveguide fabrication.

2.1 Femtosecond laser fabrication system

For the work described in this thesis, two main femtosecond laser writing systems were used. One system will be described in detail here, and is based on a femtosecond fiber laser that was used for the work related to the fabrication of waveguides in bulk fused silica substrates. The other system is a regenerative amplified Ti:Sapphire laser, producing 130 fs pulses with 800 nm center wavelength. This system was used for the fabrication of fiber Bragg gratings (FBGs) in suspended-silica-core fibers and its characteristics will be described in detail in Chapter 3.

The femtosecond fiber laser system used for fabrication of waveguides in bulk fused silica is shown in Fig. 2.2 and consists of an Yb-doped fiber chirped pulse amplified system (IMRA America µJewel D-400-VR), with a center wavelength of 1044 nm and variable repetition rates from 100 kHz to 5 MHz. The key characteristics of this system are summarized in Table 2.1.

Table 2.1: µJewel D-400-VR specifications

Parameter	Specification*
Repetition rate (MHz)	0.1 - 5
Center wavelength	1044 nm
Emission bandwidth FWHM	<10 nm
Polarization contrast ratio	>20 dB
Pulse contrast ratio	38 dB
Pulse energy noise	< 5% rms
Output power stability	<5%
Beam quality, M^2 (X, Y)	1.4, 1.3
Output beam diameter $(1/e^2)$ (X, Y)	3.7 mm, 3.4 mm
Beam divergence (X, Y)	0.83 mrad, 0.55 mrad
ACF width	450 fs

*Provided by the manufacturer.

The fiber laser produces uncompressed ≈500 ps width pulses that are aligned through a compressor composed by three mirrors, one grating and one prism. After compression the pulse width is ≈300 fs full width at half maximum (FWHM); the distance between the prism and the grating is adjustable in order to optimize the compression of the pulses according to the repetition rate provided by the laser. An example of an autocorrelation function (ACF) measurement performed on infrared pulses is shown in Fig. 2.1, where the experimental data was fitted to a Lorentzian function in order

to determine an autocorrelation FWHM value of 469 fs. This value corresponds to a pulse width[2] of 235 fs. The pulse compression step has a ∼66% efficiency, significantly reducing the power of the laser beam but, much more significantly, increasing the pulse peak power, by virtue of achieving a three order of magnitude compression. The difference between the power of the laser before and after compression for different repetition rates is shown in Table 2.2.

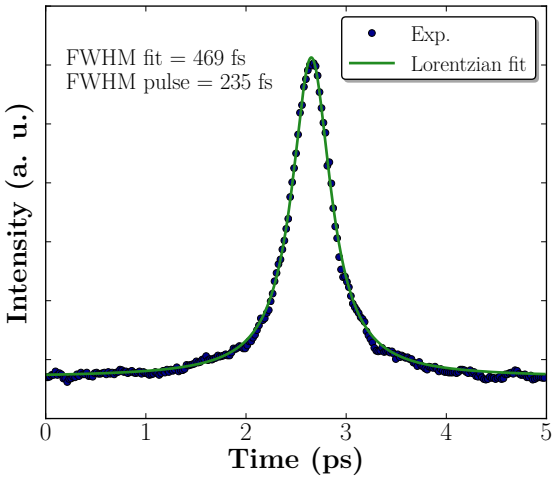

Figure 2.1: ACF measurement for infrared (1044 nm) compressed femtosecond pulses from the fiber laser.

During the course of this research, the laser system had to undergo a significant repair. This resulted in a variation of performance which is summarized in Table 2.3. After this repair the output power of the laser was more than doubled for repetition rates above 1 MHz.

The laser is linearly polarized (parallel to the optical table) and perpendicular to the z-axis (as defined in Fig 2.2). The computer controlled wave plate (Aerotech ART310 rotation stage) and the polarization beam splitter provide a way of tuning the beam power while guaranteeing the linear polarization of the laser. The laser path can then be selected between two alternatives, the non-AOM path and the acousto-optic modulator (AOM) path.

[2]The 469 fs measured for the ACF width agrees well with the value specified by the manufacturer (450 fs); however, the 235 fs of pulse width, assumed from the deconvolution factor of the Lorentzian function (with a value of 2) is smaller than the reported 300 fs used to characterize the laser. This is due to the use of a conservative hyperbolic secant squared (sech^2) function with a deconvolution factor of 1.54 instead of a Lorentzian profile or even a Gaussian profile (with a deconvolution factor of $\sqrt{2}$). Regardless of the distribution used to fit the ACF data, as long as that distribution is specified, the results can be replicated. Also, the pulse duration is only used to calculate the light intensity, which is only relevant if two different laser systems (or different pulse durations) are to be compared, which is not the case in this thesis.

Table 2.2: Fiber laser (µJewel D-400-VR) power comparison before and after compression for the laser after 02/07/2010

Repetition rate (MHz)	Power (mW)	
	Uncompressed	Compressed
0.1	495	320
0.2	735	483
0.5	752	503
1.0	1567	1059
2.0	1770	1195
5.0	2000	1345

Table 2.3: Fiber laser (µJewel D-400-VR) performance for different repetition rates. The power is represented in (mW) and the pulse energy is represented in (µJ)

Repetition rate (MHz)	Before 22/03/2010		After 02/07/2010*		
	Power	Pulse energy	Power	Pulse energy	Pulse width (fs)
0.1	330	3.300	320	3.200	340
0.2	490	2.450	483	2.415	340
0.5	500	1.000	503	1.006	420
1.0	510	0.510	1059	1.059	420
2.0	510	0.255	1195	0.597	450
5.0	650	0.130	1345	0.269	530

*The laser was shipped to the manufacturer for repair and upgrade.

The AOM path passes the laser beam through two telescopes, composed by four lenses, and an AOM (TeO_2 based Neos 23080-3-1.06-LTD). The first two lenses are a positive and a negative lens, respectively, that reduce the beam size to fit the AOM aperture; and the last two lenses produce the opposite effect and revert the beam to its original size. The AOM is also computer controlled by either a digital (Neos 21080-2DS) or an analog (Neos 21080-2AS) RF driver signal, and is optimized to create one first order diffraction beam with ≈60% of the total power of the input beam; this configuration serves as a fast *on/off* switch for the laser beam and can reliably operate at frequencies up to ∼1 MHz with the current setup. The ability to modulate the laser beam with the AOM allows the direct fabrication of Bragg grating waveguides (BGWs) [8], by creating a waveguide composed of periodic segments, or volumetric pixels (voxels), of refractive index higher than that of the background refractive index of fused silica.

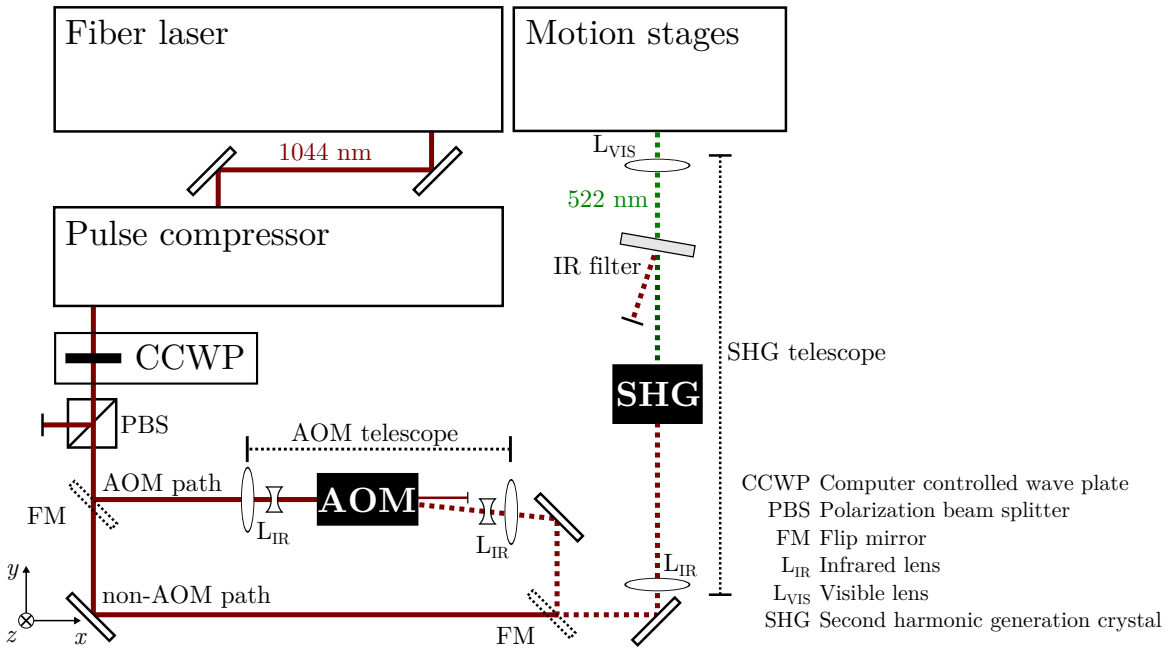

Figure 2.2: Diagram of the femtosecond fiber laser fabrication system.

This beam modulation, translates into a refractive index modulation on the waveguide, and will be further described in detail in Chapter 4.

At this point in the fabrication setup of Fig. 2.2, the laser wavelength is 1044 nm and the pulse width is 300 fs with a variable repetition rate ranging from 100 kHz to 5 MHz and the possibility of AOM modulation. As described before [44], the second harmonic wavelength ($\lambda = 522$ nm) produces a larger refractive index change in fused silica than when using the fundamental wavelength. For second harmonic generation the laser beam can be focused inside a lithium triborate (LBO) crystal, phase matched through temperature at 170 ℃ (which produces pulses at a wavelength of 522 nm with a conversion efficiency of 50%). The beam passes through a spectral filter to remove the unconverted fundamental wavelength and the polarization state of the second harmonic beam is linear and perpendicular to that of the fundamental beam. The green laser light generated by the LBO crystal is therefore polarized parallel to the z-axis (perpendicular to the optical table, Fig 2.2).

The laser beam is then aligned inside the target delivery system described in Fig. 2.3 and focused into the glass sample that is mounted in the computer controlled air-bearing motion XY-stages (Aerotech ABL1000) having a resolution of 2.5 nm and a reproducibility of 200 nm.

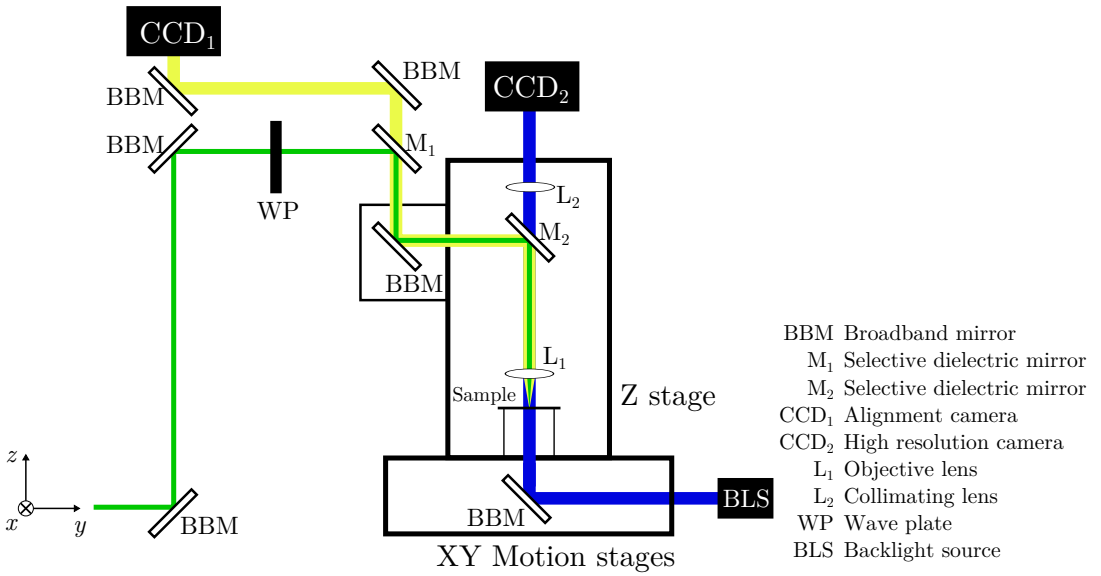

Figure 2.3: Diagram of the beam delivery system with the motion stages in Fig. 2.2.

The computer controlled Z-stage (Aerotech ALS130) positions the laser spot typically at 75 µm below the surface of the glass substrate. Aspheric lenses with numerical apertures (NAs) ranging from 0.16 NA to 0.65 NA were used to create spot sizes with diameters ranging from 5.6 µm to 1.4 µm (1.6 µm for 0.55 NA). The diameter is calculated at $1/e^2$ of the maximum intensity with Equation 2.1, where ω_0 is the spot radius for the infrared 1044 nm wavelength, considering a beam quality of $M^2 = 1.35$, and assuming a Gaussian distribution.

$$\omega_0 = \frac{M^2 \lambda}{\pi \mathrm{NA}} \tag{2.1}$$

The intensity in the laser spot can be approximated[3] by Equation 2.2, with the energy per pulse, E_p, and the laser pulse duration, τ, limited by the laser, and ω_0 limited by the diffraction limit as given by Equation 2.1.

$$I = \frac{E_p}{\tau \pi \omega_0^2} \tag{2.2}$$

[3]This approximates the beam to a rectangular distribution whose width is equal to the Gaussian spot diameter obtained from Equation 2.1, instead of the more realistic Gaussian beam.

The wave plate pictured in the diagram of Fig. 2.3 further permits the control of the laser beam polarization state to be linear along the y-axis, linear along the x-axis, circularly polarized, or any polarization state in between at the sample position. Using this freedom to control the laser polarization, together with the XY motion control, it is possible to have the polarization of the laser beam oriented parallel or perpendicular with respect to the laser scanning direction in the glass sample[4].

Figure 2.4 illustrates the laser being focused into a fused silica sample and a waveguide being formed by scanning the sample through the laser spot. The geometry shown in Fig. 2.4 also illustrates the orientation of the birefringence proper polarization axis of the waveguide modes, or polarization eigenmodes, which are formed by the orthogonal directions: Vertical, V, and Horizontal, H, defined with respect to the optical table.

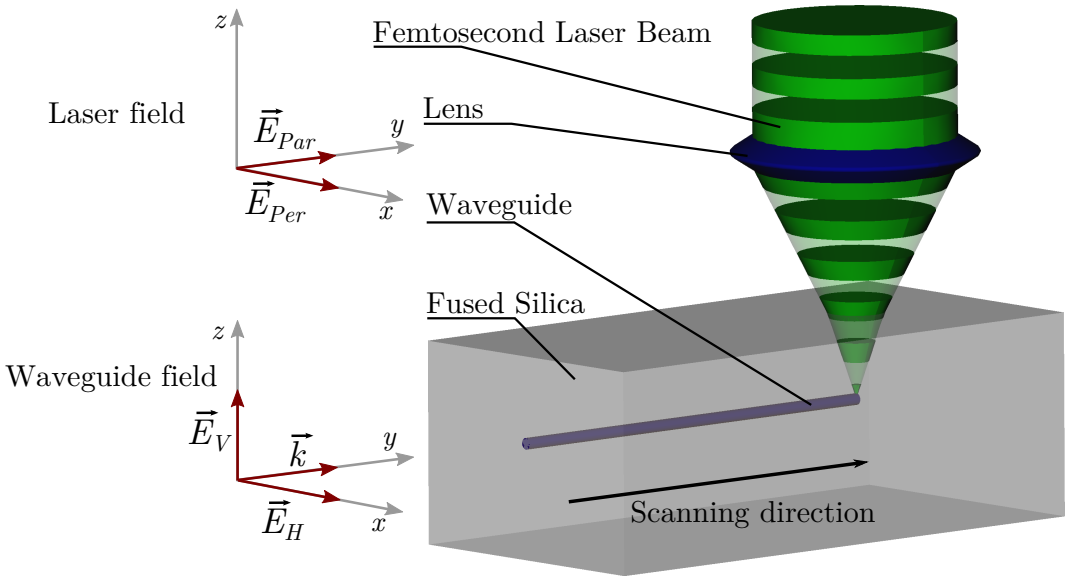

Figure 2.4: Schematic diagram of the waveguide fabrication where $\vec{E}_{Par}$ and $\vec{E}_{Per}$ represent the parallel and perpendicular polarizations of the writing laser, respectively. $\vec{E}_V$ and $\vec{E}_H$ indicate the electric field orientation of Vertical, V, and Horizontal, H, waveguide polarization modes, respectively.

Throughout this work, the substrates used were Corning 7980 fused silica with dimensions of 25.4 mm or 50.8 mm length, 50.8 mm width, and 1 mm thickness, with all

[4]For this purpose, the wave plate and the XY motion control stages are redundant, as this flexibility can either be achieved using the wave plate, to change the polarization in respect to the scanning direction, or keeping the same laser polarization but changing the scanning direction using the XY motion stages. Using the wave plate has the advantage of ignoring the effects of the non-circular laser beam shape, which also affects the writing of waveguides. By changing the polarization and keeping the same writing direction (X in the case of the waveguides used for this thesis) the effects of X versus Y writing can be ignored and differences between perpendicular or parallel writing studied with higher accuracy.

facets optically polished. The length chosen in each case depended on the minimum length required for each particular experimental device.

Figure 2.5 shows two pictures taken during the waveguide writing process. The green light (second harmonic) visible in Fig. 2.5(a) is the femtosecond laser being focused inside a fused silica sample; above the position of the aspheric lens. Lines of previous exposures are also visible inside the glass. In Fig. 2.5(b) the same picture is taken using a filter designed to have a high optical density (OD) for the green wavelength (same filter used for eye protection goggles). In this picture, a small point of white light is visible in the focal volume of the objective lens, which demonstrates the nonlinear absorption and emission of broadband visible light from the laser-matter interaction volume.

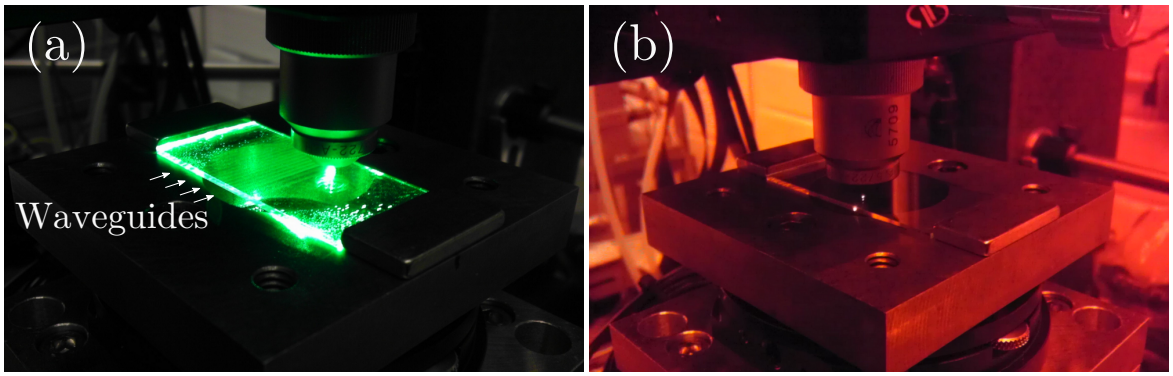

Figure 2.5: (a) Waveguide writing picture with the green femtosecond beam focused by a 0.55 NA lens into a fused silica sample. (b) Waveguide writing picture taken with a high OD filter, the kind used as eye protection, that attenuates the green wavelength from the femtosecond laser.

For the alignment of the laser for waveguide fabrication, pin holes were used throughout the set up in order to align the laser beam parallel to the optical table as in Fig. 2.2, and parallel to the vertical plate support shown in Fig 2.3. The reflection from each of the mirrors is preferred to be at 90° in order to maximize the reflection from the dielectric coatings and maximize the amount of power available for waveguide writing. Lastly, the last mirror, before the objective lens that focuses the laser beam inside the glass substrate, must be aligned such that the laser beam is perpendicular to the sample. This reduces aberrations produced by the air glass interface which can distort the intensity profile of the beam focal spot and change the shape of the waveguides.

2.2 Waveguide characterization

Waveguides were characterized using the setups described in Fig. 2.6 and Fig. 2.7. Both use two Luminos I3000 (3-axis) precision stages with three degrees of freedom (x, y and z) to position the input and the output, fiber or lens, of the system. The sample is also positioned in an independent Luminos I5000 (5-axis) precision stage and held in place by vacuum; this stage has the ability to move the sample in the x, y, and z directions and also to rotate in the z-axis (yaw) and in the y-axis (pitch), allowing for five degrees of freedom to correctly position the waveguides with respect to the other two stages. Both Luminos I3000 (3-axis) and I5000 (5-axis) have manual control with 100-nm resolution.

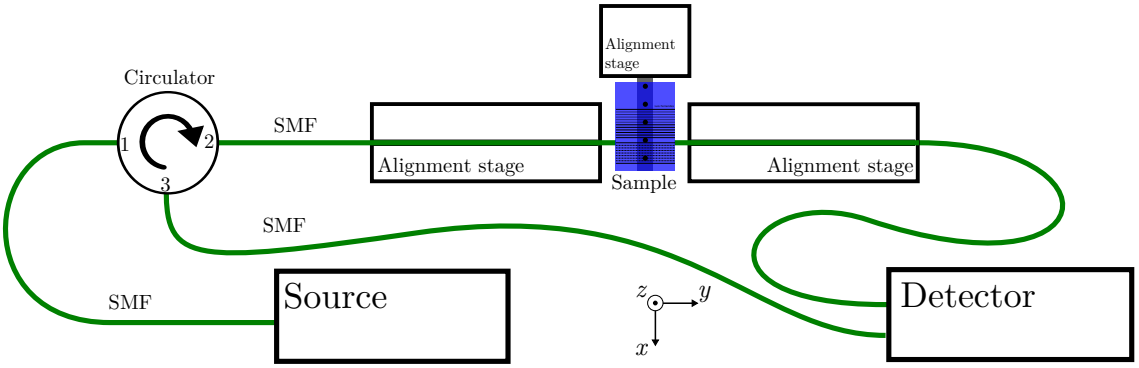

Figure 2.6: Fiber based waveguide characterization system.

Figure 2.6 shows an all-fiber arrangement where the waveguides in the sample are aligned between two cleaved optical fibers that rest on the two lateral Luminos I3000 (3-axis) precision stages. This permits the precise lateral and angular alignment of the fiber facets with the waveguide faces for efficient coupling of the probe light. This arrangement has the advantage of being easy to align and stable for long optical measurements. An optical circulator may also be used to provide the simultaneous recording of reflected and transmitted light from the waveguide structure in the detector.

Figure 2.7 shows a free space setup, where the light coming from the source is launched into free space by a free space coupler and focused onto the waveguide facet by an aspheric objective lens 30×, 0.4 NA resting on the input precision stage. The output of the waveguide is collected by another objective lens, resting on the output precision stage and recoupled into an optical fiber to be brought to the detector. One advantage of this measurement configuration is that before and after the objective lenses the

beam can go through any number of bulk optical components. In Fig. 2.7 the simple case of a linear polarizer and an analyzer in the optical path is shown, permitting, for example, probing of the birefringence properties of the waveguides under study. Other components may be used to prepare an arbitrary polarization state before the sample. For the purpose of measuring the birefringence properties of uniform waveguides and Bragg grating waveguides (BGWs), broadband nanoparticle linear film polarizers (Thorlabs LPNIR) were used with very large spectral coverage (650 nm to 2.0 µm), covering all the unpolarized broadband sources available for this work. The ability to perform birefringence measurements as a function of the wavelength greatly improved the quality of the results presented in Chapter 5 by retrieving more information than the typical experiments where a single wavelength polarized laser is used instead.

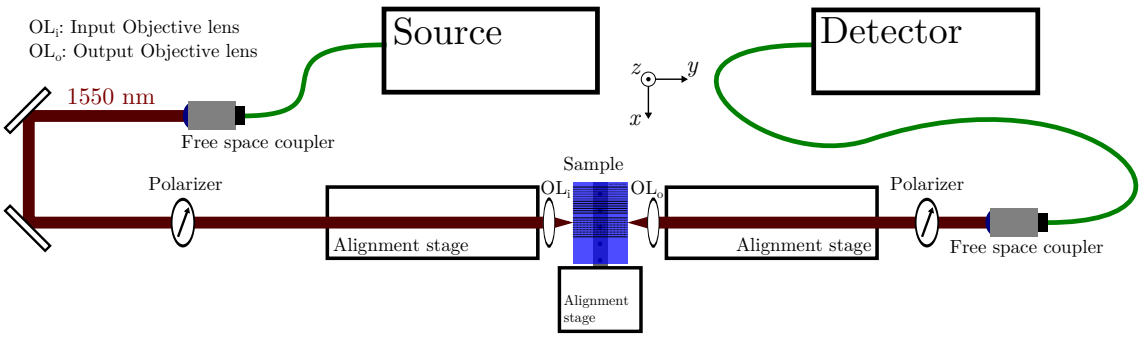

Figure 2.7: Free space based waveguide characterization system.

The optical sources available for this characterization system included a broadband erbium amplified spontaneous emission (ASE) light source (Thorlabs ASE-FL7002), emitting from 1530 nm to 1610 nm (Fig. 2.8), four coupled edge-emitting LEDs (EELEDs), each centered at a different wavelength (Agilent 83437A), with a combined broadband from 1250 nm to 1700 nm (Fig. 2.9), and a tunable laser (Photonetics Tunics-BT). The detectors available included an Ando 6317B optical spectrum analyzer (OSA) capable of measuring wavelengths from 600 nm to 1750 nm with a 0.01 nm maximum resolution and power photodetectors (Newport 818-IG).

For further flexibility of the measurement systems, the power meters and the tunable laser were also synchronized together, taking advantage of GPIB connectivity, in a computer controlled scan which enabled the possibility of simultaneously measuring two optical spectra (reflection and transmission) with 1 pm resolution. However this

method is considerably slower than using the OSA, and therefore it was only used when higher resolution was required and typically for narrow bandwidths[5].

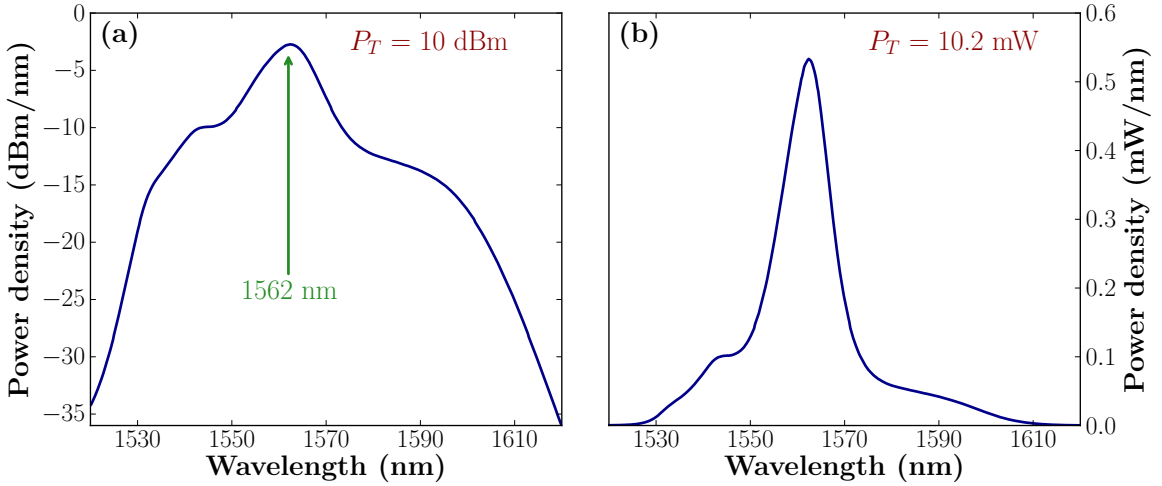

Figure 2.8: Power density on a log scale (a) and linear scale (b) for the Thorlabs ASE-FL7002 broadband source.

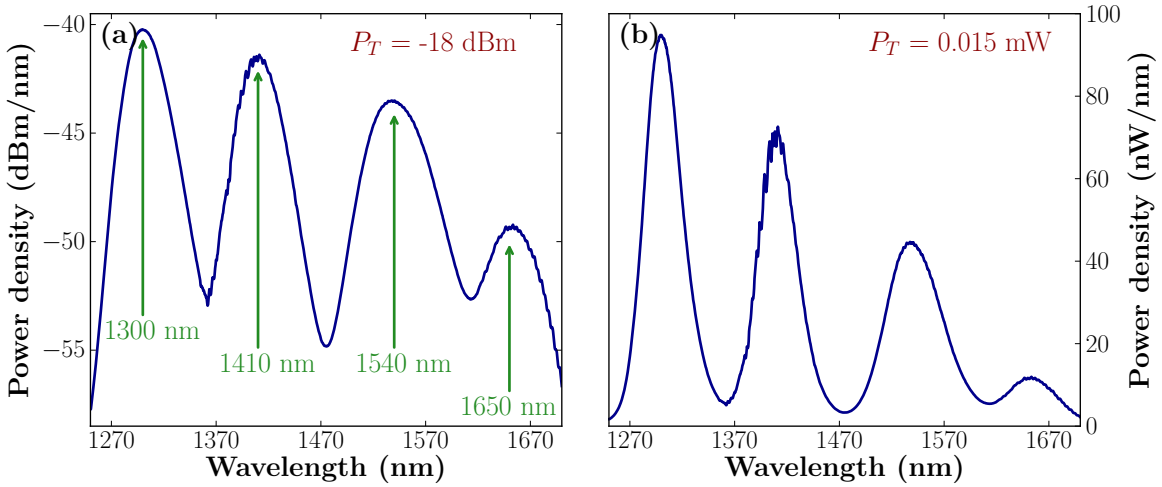

Figure 2.9: Power density on a log scale (a) and linear scale (b) for the Agilent 83437A broadband source.

[5]This approach was appropriate for scans with bandwidths on the order of nanometers (a 1 nm scan would take ≈ 30 s to record).

2.3 Mode profiles

To obtain the mode field diameters (MFDs) and account for the mode mismatch with optical fibers, the intensity profile of the modes propagating in the waveguides can be recorded as shown in Fig. 2.10, by coupling the light from a tunable laser (Photonetics Tunics-BT) with a single mode fiber (SMF) to the waveguides and imaging the output onto a phosphor-coated silicon charge-coupled device (CCD) camera (Spiricon SP-1550M) by a 60× magnification lens. The camera has a 1600 × 1200 resolution in an area of 7.0 × 5.3 mm^2, with a pixel size of 4.4 × 4.4 μm^2, and spectral response from 190 nm to 1100 nm and from 1440 nm to 1605 nm.

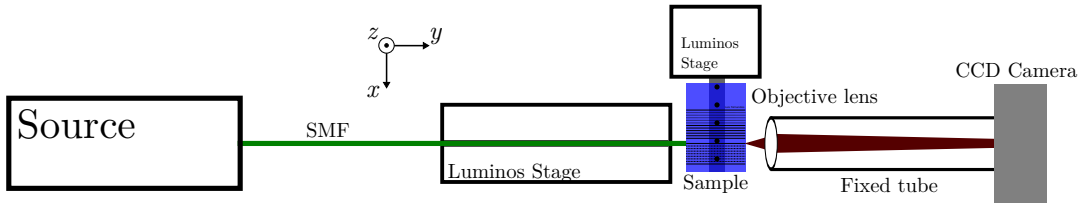

Figure 2.10: Characterization system used to record the MFD of waveguides and fibers.

Figure 2.11 shows the mode profile of a SMF recorded at 1560 nm. This profile is used to calibrate the image scale, with the mode size of the fiber known to be 10.4 µm at this wavelength. The pixel size of the camera together with the 60× magnification lens and a ∼20 mm tube length, resulted in a system resolution of 16 nm/pixel.

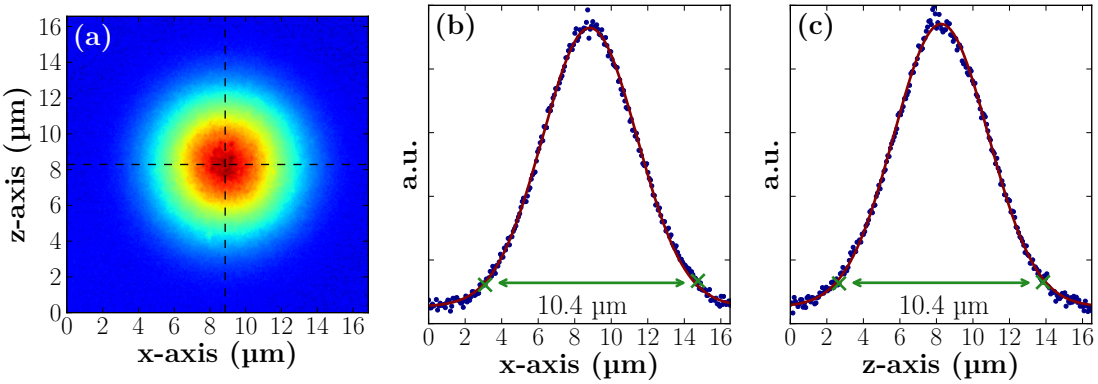

Figure 2.11: (a) SMF intensity mode profile. (b) Intensity mode profile for one dimension in the x-axis selected at the maximum intensity point. (c) Intensity mode profile for one dimension in the z-axis selected at the maximum intensity point.

It is useful to estimate the mode mismatch losses created by the difference between the MFD of an SMF and the waveguides fabricated in bulk glass. The MFD can

be measured with the setup described in Section 2.2 and the coupling efficiency, η, between any two given waveguide modes can be estimated by the overlap integral between the two modes, shown in Equation 2.3, where the $u_m(x,z)$ functions are the electric field mode distributions of the two coupling waveguides.

$$\eta = \frac{\left|\int_{\infty}^{\infty} u_1(x,z)u_2(x,z)\mathrm{d}x\mathrm{d}z\right|^2}{\int_{\infty}^{\infty}|u_1(x,z)|^2\,\mathrm{d}x\mathrm{d}z\int_{\infty}^{\infty}|u_2(x,z)|^2\,\mathrm{d}x\mathrm{d}z} \tag{2.3}$$

For Gaussian shaped mode distributions, Equation 2.3 can be simplified to Equation 2.4, where a is the mode diameter of a SMF and d_x and d_z are the mode diameters of the waveguide in the x and z directions, respectively, and with all the diameters measured at $1/e^2$ of the intensity profile ($1/e$ of the electric field).

$$\eta = \frac{4a^2d_xd_z}{(d_x^2+a^2)(d_z^2+a^2)} \tag{2.4}$$

The coupling efficiency, η, can be converted into coupling loss (CL) (in dB scale) by Equation 2.5.

$$\mathrm{CL} = 10\log_{10}(\eta) \tag{2.5}$$

In order to determine the mode diameters, d_x and d_z, for the given recorded mode profiles, first, the center point of the intensity profile is chosen by fitting to a two-dimensional Gaussian function. The center points are noted in the intensity profiles (Fig 2.12(a) and Fig 2.13(a)) as two orthogonal dashed lines. The $1/e^2$ intensity points are then determined by either fitting the one-dimensional profiles in x and z directions (red lines in Fig 2.12(b), Fig 2.13(b), Fig 2.12(c) and Fig 2.13(c)) or by finding the experimental data points which are closest to the $I_{\max}/e^2$ level for the same x and z directions (green marks in Fig 2.12(b), Fig 2.13(b), Fig 2.12(c) and Fig 2.13(c)).

These two methods occasionally provide inconsistent results as the intensity distributions are not always fitted well to a Gaussian function. The MFDs reported with either method have an uncertainty of $\pm 0.2\,\mu\mathrm{m}$ associated with the measurements.

Another method to estimate the waveguide coupling loss is based on numerically solving Equation 2.3 using the recorded intensity profiles. The electric filed distribution is the square root of the intensity values and the integrals are treated as sums inside the recorded window. This is more accurate that using the simplified coupling efficiency in Equation 2.4, but is also more difficult to perform, as the results in the form of intensity matrices have to be centered and the noise in the recorded values negatively affects the final loss result.

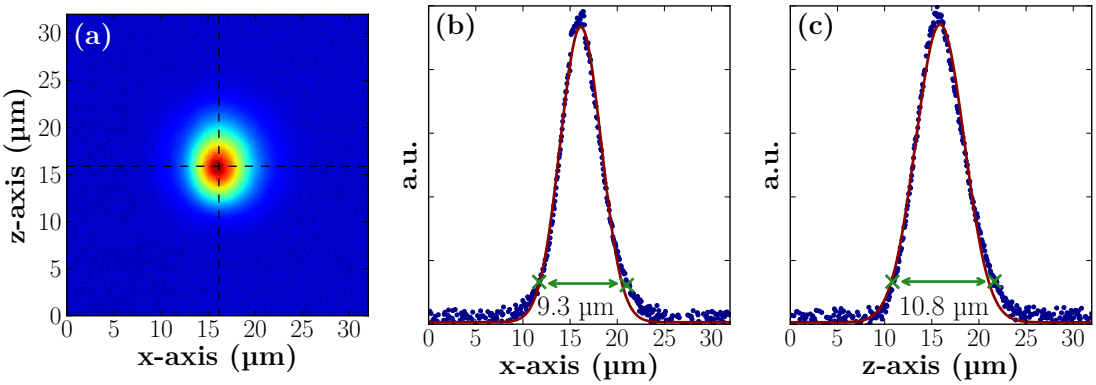

Figure 2.12: (a) Uniform waveguide intensity mode profile. (b) Intensity mode profile for one-dimension in the x-axis selected at the center intensity point. (c) Intensity mode profile for one-dimension in the z-axis selected at the center intensity point.

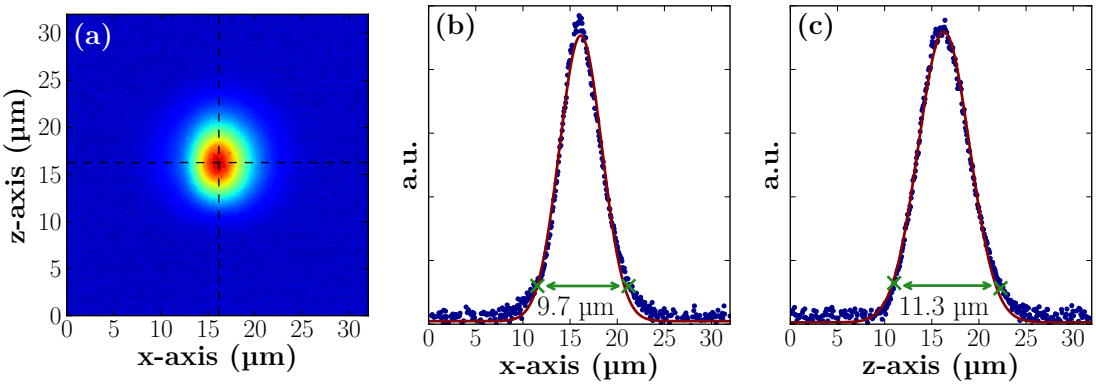

Figure 2.13: (a) BGW intensity mode profile. (b) Intensity mode profile for one-dimension in the x-axis selected at the center intensity point. (c) Intensity mode profile for one-dimension in the z-axis selected at the center intensity point.

Figure 2.12(a) shows an intensity mode profile recorded for the example of an uniform waveguide where values of $d_x = 9.3\,\mu m$ and $d_z = 10.8\,\mu m$ were calculated and used to infer a coupling loss of (0.03±0.02) dB/facet. Figure 2.13 shows the results for a BGW with $d_x = 9.7\,\mu m$ and $d_z = 11.3\,\mu m$, yielding a coupling loss of (0.03±0.02) dB/facet.

Numerically determining the losses based on Equation 2.3 and on the mode profile in Fig. 2.12 resulted in a coupling loss of 0.05 dB/facet, which was the best value achievable by manually centering the matrices and by minimizing the noise contribution, with the calculation made considering only a small window around the profile center (13 µm).

All these results provide an underestimation of the coupling losses because other factors, like alignment, perpendicularity of the waveguides relative to the sample edge, quality of the glass polishing, and quality of fiber cleaving, all increase the coupling losses in a real measurement. The propagation loss, α (measured in dB per unit of length), for a waveguide can be determined with Equation 2.6, where IL is the total insertion loss measured for a device and L is the length of the waveguide.

$$\alpha = \frac{\mathrm{IL} - 2\mathrm{CL}}{L} \tag{2.6}$$

Since the underestimated coupling loss per facet, CL, is used to subtract from the total insertion loss, IL, measured on every device, the final reported results for propagation loss, α, are always overestimated.

2.4 Summary of fabrication conditions

The best laser writing conditions for low loss waveguides in fused silica have been found with 0.55 NA focusing, 522 nm writing laser wavelength and laser polarization parallel to the scanning direction [45, 46].

Table 2.4: Summary of propagation losses reported for waveguides fabricated in fused silica (Corning 7980) at 1550 nm

Rep. rate (kHz)	Pulse energy (nJ)	Scan speed (mm/s)	α (dB/cm)	Ref.
500	200	0.50	0.43	[45]
1000	175	0.75	0.35	[45]
500	150	0.25	0.5	[46]
1000	150	0.50	0.3	[46]

The losses reported here were obtained at 1550 nm; there is a wavelength dependency on the waveguide propagation loss and an absorption band at 1384 nm which is due to a high concentration of OH impurities in the substrate.

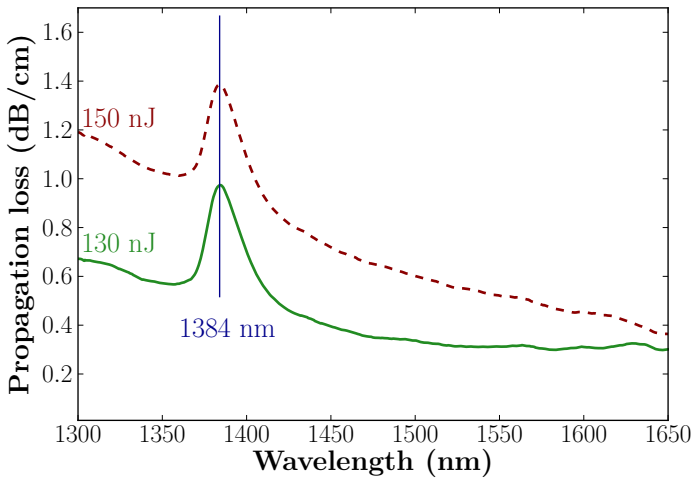

Figure 2.14: Propagation loss as a function of wavelength for two waveguides fabricated with 130 nJ and 150 nJ pulse energies.

Figure 2.14 shows the propagation losses of two waveguides as a function of the wavelength for the entire spectral region studied in this thesis (1300 nm – 1650 nm). The waveguides were fabricated with pulse energies of 130 nJ and 150 nJ, and using a 0.55 NA lens, with the laser operating at 500 kHz and 522 nm center wavelength, and with the sample scanned at a constant speed of 0.27 mm/s with the laser polarization being parallel to the scanning direction.

The waveguide devices studied here were based on known parameters summarized in Table 2.4. This gave the lowest loss waveguides as a good starting point for the fabrication of waveguides, BGWs and directional couplers. The fabrication conditions may depart from these optimum values for various reasons: for example, to consider shifts in the laser characteristics over time, or for the study of waveguide properties as a function of any of the fabrication variables. Although the lowest losses for waveguides in fused silica can be found with a repetition rate of 1 MHz, this is not ideal for the fabrication of BGW where a repetition rate of 500 kHz is preferred [46]. For this reason, 500 kHz was the repetition rate used for the fabrication of devices in this thesis.

Chapter 3

Fiber Bragg gratings in suspended silica core fibers

In this chapter, fiber Bragg grating (FBG) arrays in pure silica four-leaf clover shaped suspended core fibers (SCFs) were fabricated by two-beam interference of a deep ultra violet (DUV) femtosecond laser source (3.6 W at 800 nm, 130 fs, 1 kHz frequency tripled to 350 fs, 650 mW at 267 nm) using a Talbot interferometer. The types of fiber used here are made of pure silica, they were not treated with hydrogen before grating inscription and did not contain any dopants to increase photosensitivity. The flexibility provided by the Talbot interferometer allowed for the determination of the effective index and the confinement factors of the guided modes, providing a repeatable method of tuning the FBG resonance wavelength and also the fiber's response for sensing applications.

The spectral behavior in the C-band of FBGs was analyzed as a function of temperature and strain. A defect fiber (with a hollow hole in the core) and non-defect fiber were compared, both yielding ≈1 pm/με sensitivity to strain but different sensitivity to temperature (from 3.0 pm/°C to 8.4 pm/°C for the defect fiber and 10 pm/°C for the non-defect fiber). The 16% to 70% relative difference between the thermal coefficients of the two fibers, together with their similar strain sensitivity, enables the simultaneous measurement of strain and temperature.

3.1 Background

FBGs have been extensively used in sensing applications for strain and temperature measurements due to the attractiveness of the platform which can be used for distributed sensing or applications in hazardous environments. Besides the standard single mode fibers commonly used, other fibers have been found to be particularly interesting for sensing applications, such as photonic crystal fibers (PCFs) [47] or SCFs [48]. Suspended core fibers are microstructured fibers with a small core suspended by extremely fine glass bridges, defining a core surrounded by hollow holes between the bridges, as seen in Fig. 3.1. The hollow holes around the core provide the confinement needed for single mode waveguide operation in the C-band.

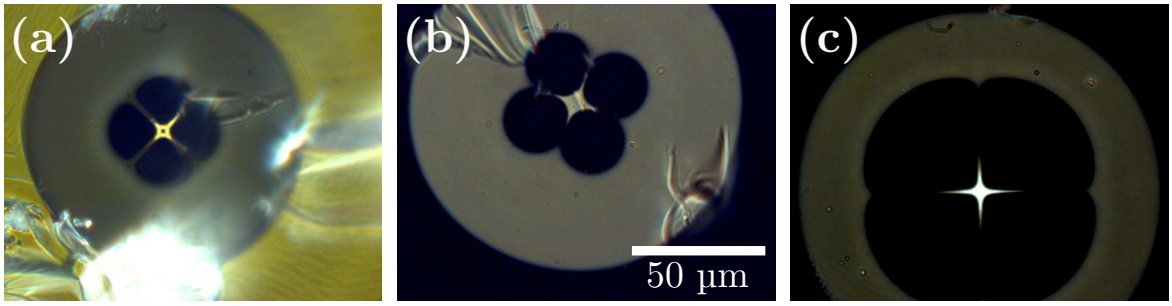

Figure 3.1: Microscope images of the facets of three pure silica SCFs: (a) defect IPHT-256b2, (b) non-defect IPHT-256b5 and (c) non-defect IPHT-256b1.

The geometry of SCFs increases the extension of the evanescent wave (decreased confinement), making them specially attractive for a new generation of evanescent field sensors [49] and for fluorescence spectroscopy [50]. The reduced filling factor of the guided mode in the suspended core also shifts the zero-dispersion wavelength to shorter wavelengths, and makes this type of fiber attractive for supercontinuum generation [51]. The SCFs used here were previously tested in the implementation of an interferometric sensor [52].

To generate FBGs in SCFs, the standard method of employing fibers with germanium-doped cores and hydrogen loading can be used [49]. However, the small dimensions of the core and the presence of the hollow holes speed the hydrogen out-diffusion by orders of magnitude when compared to standard fibers. One possible approach to reduce the out-diffusion is by sealing the end faces of the fiber [53]. This method has the disadvantage of producing extra losses in the coupling between the SCFs and the detection system which reduces the visibility of the FBGs during grating inscription. To avoid the standard methods and produce photoinduced refractive index

changes in pure silica fibers, high photon energies and intensities are required. The use of femtosecond laser pulses [7] opens the possibility of creating refractive index modulation in the pure silica core.

Phase mask inscription with 193 nm argon fluoride (ArF) excimer lasers [54, 55] and with IR femtosecond laser sources [56] have already been demonstrated. The use of DUV sources allows for minimization of structural dimensions [57], and phase mask inscription with 267 nm femtosecond lasers [58] can also be applied to pure silica fibers [59, 60].

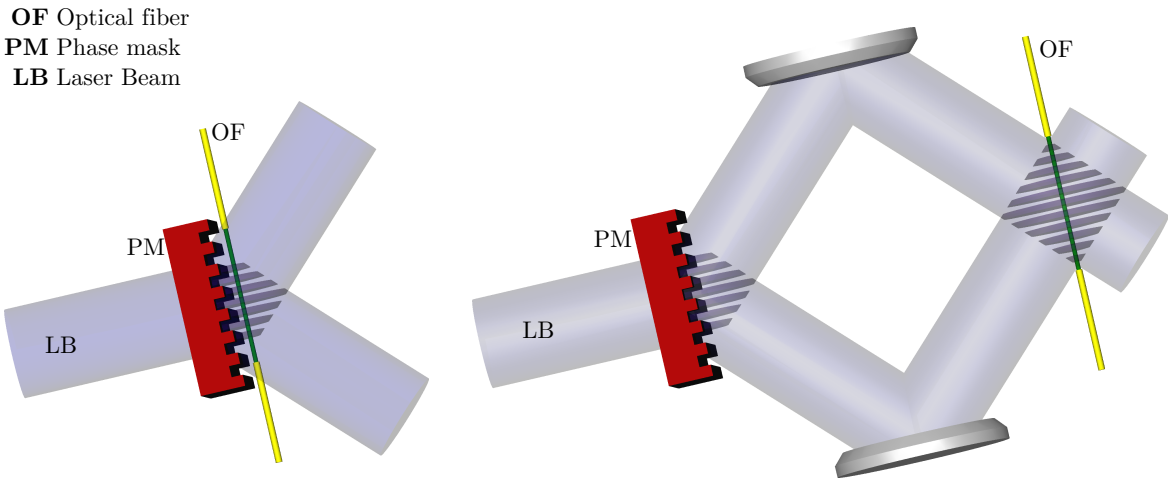

Figure 3.2: Comparison between positioning the optical fiber close to the phase mask (left) and placing the fiber further away with a Talbot interferometer (right). A cylindrical lens placed before the phase mask focuses the beam in the fiber position.

In the typical phase mask approach, the fiber has to be placed directly behind a phase mask, close to the surface, where the interference pattern is formed. This requires the photosensitivity of the fiber to be higher than that of the phase mask; if both fiber and mask are made of the same material, fused silica in this case, degradation starts to happen in the phase mask, accompanied by red luminescence caused by nonbridging oxygen hole centers [61, 62]. In order to avoid this problem, the space between the phase mask and the target has to be increased [63], therefore reducing the light intensity at the phase mask position. This can be efficiently achieved by the use of a Talbot interferometer which consists of two mirrors that reflect the two first order diffraction beams and produces another interference pattern further way from the phase mask. This interferometric configuration has the added advantage of being tunable, since the periodicity of the interference pattern can be changed by

controlling the angles on the mirrors. Fig. 3.2 illustrates the difference between these two methods.

3.2 Fabrication

The fabrication system used for the SCF gratings [64] consists of a femtosecond infrared master oscillator pulse (Coherent Mantis) and a regenerative Ti:Sapphire femtosecond amplifier (Coherent Legend Elite). Laser pulses of 130 fs pulse width, 800 nm center wavelength, 3.6 W average power and 1 kHz maximum repetition rate were produced with the possibility of selecting a fraction of the maximum repetition rate, but maintaining the laser pulse energy constant. A third harmonic generation unit produces DUV laser pulses of ≈350 fs pulse width and 650 mW average power centered at 267 nm.

To define the Bragg grating structures, the beam is focused through a 335 mm focal length cylindrical lens into a Talbot interferometer setup [65, 66] composed of a phase mask (1065.3 nm periodicity optimized for 267.2 nm wavelength) that splits the beam, and two computer controlled rotation mirrors, as shown in Fig. 3.3. The first two diffraction orders from the phase mask are reflected by the mirrors and interfere in the focal plane of the cylindrical lens, where the fiber is positioned, creating the standing wave pattern for FBG inscription, while the non-diffracted (zero-order) beam is blocked. The total transmission efficiencies of the interferometer are 18% and 20% for the first diffraction orders, and the power density at the fiber position is approximately 47 GW/cm^2. The angle of the mirrors together with the phase mask period define the periodicity of the interference pattern [67, 68].

Contrary to the standard phase mask fabrications setups, this approach provides the ability to tune the Bragg grating reflection wavelength by varying the angles of the mirrors, limited by the coherence length and the requirement for parallel pulse fronts at the target [67]. At the same time, this setup increases the distance between the phase mask and the fiber, effectively reducing the laser intensity at the mask position and overcoming the degradation problems in the phase mask discussed before.

To measure the reflected spectrum during fabrication, the SCFs were spliced with standard single mode fibers (SMFs) using an arc-discharge fusion splicer (Sumitomo F36). A previous method [69] was modified and optimized for this purpose in order

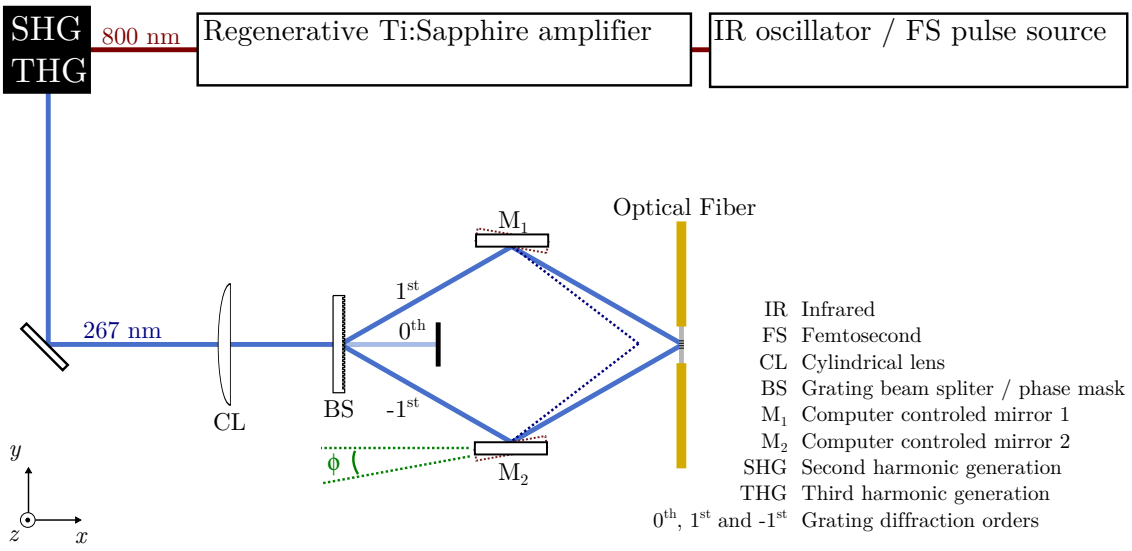

Figure 3.3: FBG fabrication system for SCFs, based on two-beam interference with a DUV femtosecond laser.

to prevent the collapse of the core and the bridges and in order to reduce reflections and prevent interference with the FBGs signal. The propagation losses in the SCFs is on the order of tens of dB/km.

The fibers used here are shown in Fig. 3.1 and were manufactured by the Institute of Photonic Technology (IPHT). The IPHT-256b1 fiber (Fig. 3.1c) has a 5 µm diameter core and a 135 µm diameter cladding, while the IPHT-256b5 fiber (Fig. 3.1b) has a 7.2 µm diameter core and a 123 µm diameter cladding. These are considered non-defect fibers because the core is entirely made of fused silica. On the other hand, the IPHT-256b2 (Fig. 3.1a) has a 4.9 µm diameter core, a defect hollow hole inside the core with 1.4 µm diameter and a 106 µm diameter cladding. This hollow hole is considered a defect when its dimensions are similar to the wavelength and, therefore, small enough not to affect the single mode propagation while still significantly contributing to the effective index of the waveguide. The characteristics of these SCFs are summarized in Table 3.1. The three fibers shown in Fig. 3.1 and described in Table 3.1 were exposed to the femtosecond DUV radiation for approximately 30 min. The growth of the Bragg grating resonance was observed in real time and the experiments ended when further exposure would not produce an increase in the reflection spectrum peak.

Table 3.1: Suspended core fibers characteristics

SCF name	Diameter (µm)			Width (µm)
	Core	Hole	Cladding	Bridge
IPHT-256b1	5	92	135	1.5
IPHT-256b2	4.9 (1.4)*	41	106	1.0
IPHT-256b5	7.2	57	123	0.9

*Fiber IPHT-256b2 has a hollow hole with 1.4 µm of diameter inside the 4.9 µm diameter core.

3.3 Fiber Bragg Gratings results

Different laser pulse repetition rates, from 333 Hz to 1 kHz, were used in order to study the fabrication of FBGs in SCFs. It was observed that the rate of growth of the grating and the maximum achievable grating reflectivity were both proportional to the repetition rate. This suggests that the cumulative effects of femtosecond laser pulses plays an important role, together with the single pulse energy in the refractive index change produced in fused silica.

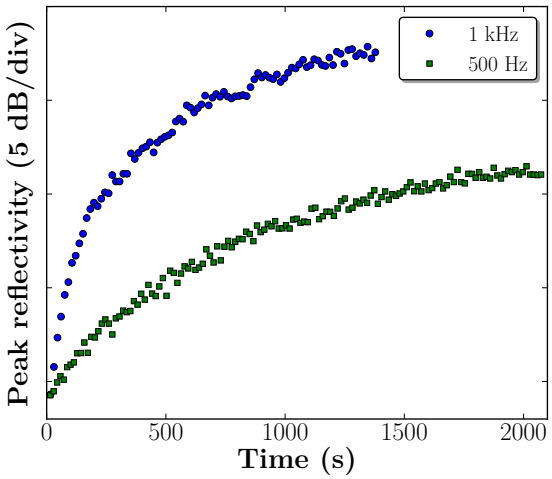

Figure 3.4: FBG reflectivity as a function of the exposure time for the IPHT-256b1 fiber, using the laser at 1 kHz and 500 Hz repetition rates.

Fig. 3.4 shows the Bragg grating reflectivity increasing with exposure time for the IPHT-256b1 fiber. After approximately 25 min, with the laser operating at 1 kHz

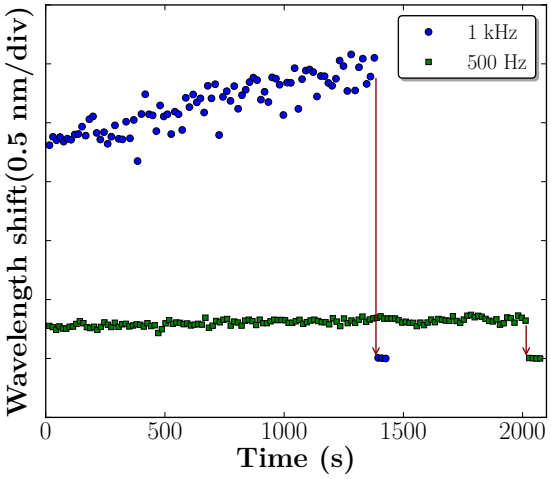

Figure 3.5: Variation of the Bragg wavelength as a function of the exposure time for the IPHT-256b1 fiber, using the laser at 1 kHz and 500 Hz repetition rates. The vertical red line indicates when the laser exposures ended.

repetition rate, no further increase in the grating reflectivity was observed. The Bragg grating resonance increased in wavelength along the exposure time as shown in Fig. 3.5. Additionally, by blocking the DUV femtosecond laser exposure, there was a sudden shift in the Bragg wavelength (marked in the plot by the red vertical arrow). The magnitude of this shift depended mainly on the laser repetition rate, as well as the fiber type, and was attributed to temperature increase in the fiber during FBG fabrication. Considering a FBG sensitivity of approximately 10 pm/℃, the wavelength difference suggests a temperature in the exposed regions greater than 200 ℃ for 1 kHz and 30 ℃ for 500 Hz repetition rates.

In Fig. 3.6, a comparison is shown for the Bragg wavelength variation as a function of the exposure time between the IPHT-256b2 and the IPHT-256b5 fibers. The same shift in the Bragg wavelength is observable when the laser is blocked. Here, the temperature variation was close to 300 ℃ for the IPHT-256b5, and approximately 150 ℃ for the IPHT-256b2 fiber.

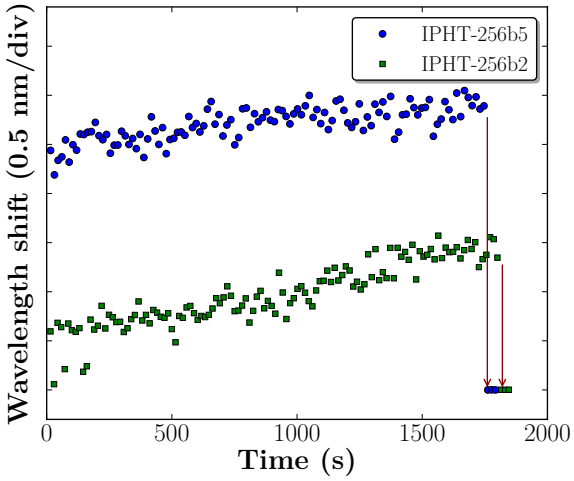

Figure 3.6: Variation of the Bragg wavelength as a function of the exposure time for the IPHT-256b2 and IPHT-256b5 fibers, using the laser at 1 kHz repetition rate. The vertical red lines indicate when the laser exposure ended.

3.4 Effective mode field refractive index

The geometry of the Talbot interferometer, together with the periodicity of the phase mask, determine the Bragg grating resonant wavelength according to Equation 3.1. Here, ϕ is the tilt angle of the mirrors, λ_B is the Bragg wavelength, and α is defined by Equation 3.2, where λ_{laser} is the wavelength of the femtosecond laser used for the FBG inscription and Λ_{pm} is the phase mask period.

$$\sin(2\phi + \alpha) = \frac{n_{\text{eff}}\lambda_{\text{laser}}}{\lambda_B} \tag{3.1}$$

$$\alpha = \arcsin\left(\frac{\lambda_{\text{laser}}}{\Lambda_{\text{pm}}}\right) \tag{3.2}$$

The effective refractive index of the guided mode can be calculated from the measured Bragg wavelength (λ_B) and, subsequently, used to predict the tilt angle of the mirrors (ϕ) required to obtain a specific Bragg wavelength reflection.

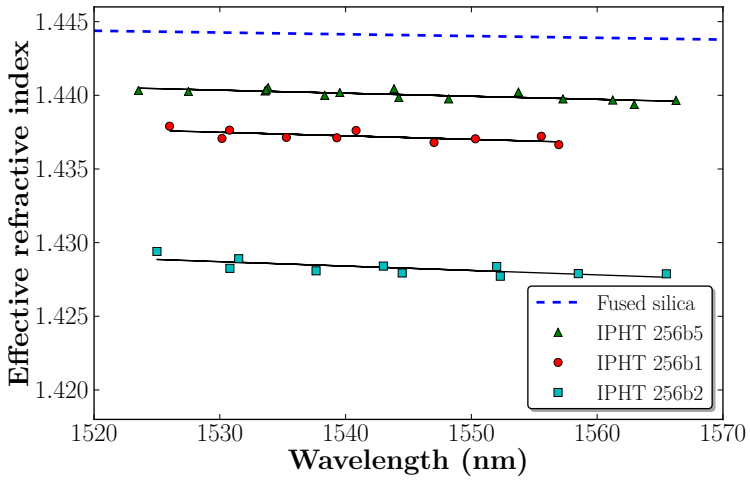

Figure 3.7: Effective index of the fiber mode for the SCFs as a function of wavelength. The straight line for Suprasil was calculated based on the Sellmeier coefficients for pure silica. *Courtesy of Martin Becker* [64].

The effective index values as a function of wavelength were calculated based on Equation 3.1 with different tilt angles for the three different SCFs, as shown in Fig. 3.7. In the same picture the refractive index of pure silica, as determined by the Sellmeier equation, is shown for comparison. As expected, the effective indices of the SCFs are smaller than the values for fused silica and the lower values obtained for the IPHT-256b1 and IPHT-256b2 suggest a significant field overlap with the air holes around the silica fiber cores.

The confinement factor f of such fibers can be determined by Equation 3.3, where n_{air} and n_{silica} are the indices of refraction of air and fused silica, respectively.

$$n_{\text{eff}} = (1 - f)n_{\text{air}} + f n_{\text{silica}} \tag{3.3}$$

With $n_{\text{air}} = 1$ and n_{silica} determined by the Sellmeier equation, the confinement factors found were 0.96 for the IPHT-256b2, 0.98 for the IPHT-256b1, and 0.99 for the IPHT-256b5. As expected, the confinement factor for the IPHT-256b2 is much smaller when compared with the other two fibers. This is mostly due to the air hole inside the fiber, which interacts strongly with the fiber mode, and suggests that this geometry can have higher evanescent field sensitivity to materials other than air present in the holes.

An array of cascaded FBGs with different periods, written at different positions along a SCF, is shown in Fig. 3.8.

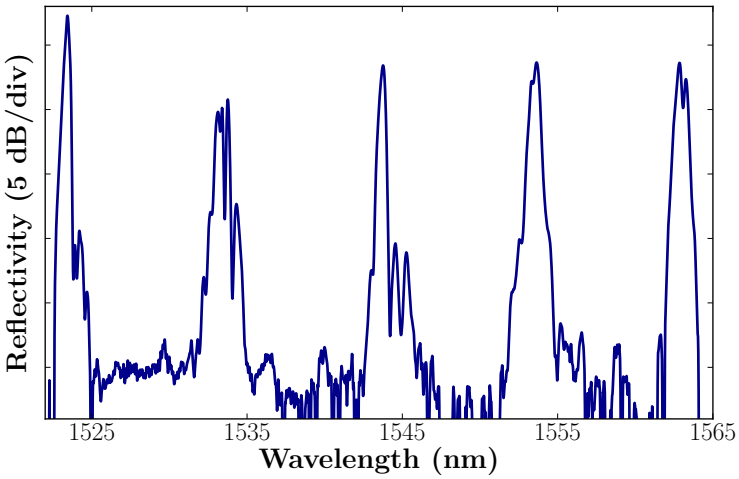

Figure 3.8: Reflection spectrum of an array of FBGs written in the IPHT-256b5 fiber.

3.5 Temperature and strain sensor

Simultaneous temperature and strain measurements were demonstrated using FBGs written with the method described in Section 3.2, and two different SCFs. The main advantage provided by these fibers is the possibility of controlling the temperature sensitivity using different core geometries.

3.5.1 Theoretical Analysis

The first derivative of the Bragg relation, $\lambda_B = 2n_{\text{neff}}\Lambda$, with respect to temperature T is given by Equation 3.4, where λ_B is the Bragg resonance, n_{neff} is the effective index of the waveguide mode and Λ is the periodicity of the FBG.

$$\frac{d\lambda_B}{dT} = 2\frac{d\Lambda}{dT}n_{\text{neff}} + 2\Lambda\frac{dn_{\text{neff}}}{dT} \tag{3.4}$$

The term $d\lambda_B/dT$ is the temperature sensitivity of the FBG, and $d\Lambda/dT = \Lambda\alpha_L$, where α_L is the linear thermal expansion coefficient. The dn_{neff}/dT term is the thermo optic

coefficient of the waveguide mode. A similar analysis can be done for evanescent field sensing [70].

The rewriting of Equation 3.4 by taking into account the thermal expansion coefficient and the Bragg relation yields:

$$\frac{d\lambda_B}{dT} = \lambda_B \alpha_L + \frac{\lambda_B}{n_{\text{neff}}} \frac{dn_{\text{neff}}}{dT} \tag{3.5}$$

In Equation 3.5 it is clear that the temperature variation has two effects over the Bragg wavelength shift: the thermal expansion coefficient of the FBG is considered in the first term, increasing the reflected wavelength with temperature, while the second term reflects the thermo optic effect, which changes the effective refractive index of the waveguide mode with temperature. For pure silica, the thermal expansion coefficient, α_L, is 5.5×10^{-7} K^{-1} [71] and the thermo optic coefficient is 8.6×10^{-6} K^{-1} at 300 K and 1.5 µm wavelength [72]. For air, the thermo optic coefficient is -9×10^{-7} K^{-1} [73].

In Equation 3.5, the presence of air in the defect located at the center of the core of the IPHT-256b2 fiber will reduce the overall thermo optic coefficient of the guided mode, thereby reducing the temperature sensitivity of the FBG when compared to the IPHT-256b5 fiber. Other materials like water (with a thermo optic coefficient of -8×10^{-5} K^{-1} [74]) or isopropyl alcohol (IPA) (with a thermo optic coefficient of -3.4×10^{-4} K^{-1} [75]) will have an even higher effect in reducing the FBG's temperature sensitivity. Table 3.2 summarizes the material properties relevant to this work.

The presence of the defect in the IPHT-256b2 fiber will then have a significant contribution to the temperature sensitivity of the written FBG since it will change the thermo optic coefficient of the waveguide mode. This can be useful to tune the sensitivity and perform simultaneous temperature and strain sensing, as well as refractive index sensing with higher sensitivity than that obtained by evanescent field based measurements.

Table 3.2: Material properties for suspended core fiber sensor

Material	Linear thermal expansion coefficient, α_L (K^{-1})	Thermo optic coefficient, dn/dT (K^{-1})
Fused Silica	5.5×10^{-7}	8.6×10^{-6}
Air	- -	-9×10^{-7}
IPA	- -	-3.4×10^{-4}

3.5.2 Sensor results

The strain characterization of the fabricated FBGs was performed by carefully attaching the fibers to a translation stage with 1 µm resolution that was used to apply tension to the grating region. The grating response to temperature was studied using a tubular oven with a temperature control error smaller than 0.1 ℃.

Figures 3.9 and 3.10 show the Bragg resonance wavelength and the Bragg resonance wavelength variation, respectively, as a function of strain (Fig. 3.9) and temperature (Fig. 3.10) for both IPHT-256b2 and IPHT-256b5 SCFs. The strain dependence displayed in Fig. 3.9 shows that both fibers have very similar behaviors with strain, yielding a sensitivity, $d\lambda_B/d\epsilon$, of (1.15±0.01) pm/µϵ and (1.14±0.01) pm/µϵ for the IPHT-256b2 and IPHT-256b5 fibers, respectively. The thermal sensitivity is clearly shown to be different by the Bragg resonance wavelength variation, plotted as a function of the temperature in Fig. 3.10.

Sensitivities of (8.42±0.05) pm/℃ for the IPHT-256b2 fiber with air filling the defect, and (10.0±0.2) pm/℃ for the IPHT-256b5 fiber were found. If IPA is used in the IPHT-256b2 fiber defect instead of air, the sensitivity to temperature further decreases to (3.0±0.1) pm/℃, with the IPA filling not only the central air hole but also the four lateral air holes in the SCF.

Table 3.3: Experimental sensitivity results

Fiber type	Temperature sensitivity $d\lambda_B/dT$ (pm/℃)	Strain sensitivity $d\lambda_B/d\epsilon$ (pm/µϵ)
IPHT-256b5	10.0±0.2	1.14±0.01
IPHT-256b2 (Air)	8.42±0.05	1.15±0.01
IPHT-256b2 (IPA)	3.0±0.1	- -

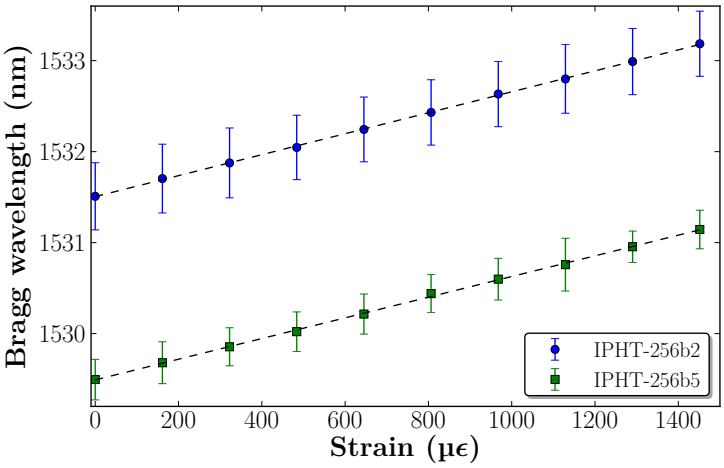

Figure 3.9: Bragg wavelength as a function of applied strain for the two fibers tested: (●) blue circle for the IPHT-256b5 and (■) green square for the defect IPHT-256b2. The dashed lines (- -) represent the best linear fit of each experimental data set.

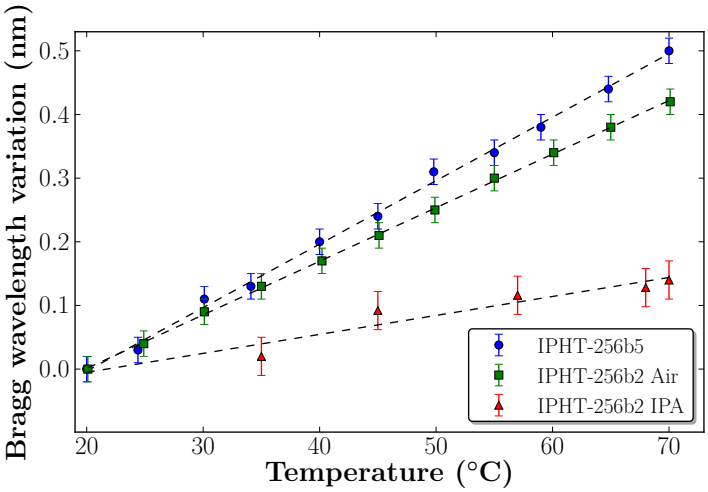

Figure 3.10: Variation, as a function of the temperature, of the Bragg wavelength compared to the FBG resonance at the starting temperature of 20 ℃. (●) blue circle for the IPHT-256b5, (■) green square for the IPHT-256b2 fiber with air in the hollow defect and (▲) red triangle for the IPHT-256b2 fiber with IPA in the hollow defect. The dashed lines (- -) represent the best linear fit of each experimental data set.

With the physical constants summarized in Table 3.2 for fused silica and using Equation 3.5, an approximate theoretical value of 10 pm/℃ (matching typical values found for fused silica fibers [76]) was found for the temperature sensitivity of the non-defect IPHT-256b5 fiber, assuming that the thermo optic coefficient in the waveguide is approximately the same as in bulk fused silica ($dn_{\text{neff}}/dT \approx dn/dT$). This result agrees well with the 10.0±0.2 pm/℃ experimental result. The temperature sensitivity

variation between the two fibers (from 16% to 70% smaller for the IPHT-256b2 when compared to the IPHT-256b5) may be accounted for by the difference in the thermo optic coefficient between fused silica, air and IPA. Using the sensitivity results from Table 3.3, it is possible to find a solution for a measurement of unknown temperature and strain based on Bragg grating shift measurements made in both fibers, according to:

$$\begin{aligned} \Delta\lambda_{b5} &= K_{T_1}\Delta T + K_{\epsilon_1}\Delta\epsilon \\ \Delta\lambda_{b2} &= K_{T_2}\Delta T + K_{\epsilon_2}\Delta\epsilon \end{aligned} \tag{3.6}$$

$$\begin{vmatrix} K_{T_1} & K_{\epsilon_1} \\ K_{T_2} & K_{\epsilon_2} \end{vmatrix} = D \neq 0 \tag{3.7}$$

Here, K_ϵ is the strain sensitivity, $d\lambda_B/d\epsilon$, and K_T is the temperature sensitivity, $d\lambda_B/dT$. The determinant of the matrix, D, in Equation 3.7 is different from zero which proves that a solution of the set of Equations 3.6 is possible. Using the sensitivity values from Table 3.3, the determinant of the set of equations using the IPHT-256b2 fiber with air in the defect is $D = 1.9\ \mathrm{pm^2 \mu\epsilon^{-1} {}^\circ C^{-1}}$, while using the same fiber with IPA in the defect will result in $D = 8.1\ \mathrm{pm^2 \mu\epsilon^{-1} {}^\circ C^{-1}}$. As it has been demonstrated [77] a larger determinant value than the one obtained with IPA allows for higher accuracy in the simultaneous measurement of temperature and strain. The IPHT-256b2 fiber was also characterized in terms of pressure response, with a 1 MPa of pressure variation applied, but no measurable shift in the Bragg wavelength was found.

3.6 Conclusion

The fabrication of cascaded fiber Bragg grating arrays in pure silica suspended core fibers was successfully demonstrated, using a femtosecond laser and a Talbot interferometer setup. This interferometric geometry eliminates the limitation introduced by the high peak laser intensity inherent to traditional FBG fabrication systems, and adds flexibility since it allows tuning of the Bragg grating reflection wavelength for different SCF types without the need for different phase masks. The confinement factors found for these fibers allows the assessment of the amount of overlap between the guided modes and the hollow holes in the SCFs, which is an important factor for evanescent field sensing applications.

These sensor results show that the fibers presented can be used to make simultaneous measurements of temperature and strain. In such a configuration where both fibers are subject to the same amount of applied tension, both would shift the resonance by approximately the same amount due to stress, while a variation in the resonance difference between the two FBGs would account for the temperature change. The temperature sensitivity dependence in the material filling the defect inside the core of the defect IPHT-256b2 fiber may be used to tune the temperature sensitivity of a FBG in such fiber, further increasing the flexibility for sensor design. Furthermore, if the temperature sensitivity is tuned to be negligible in a certain range, a strain sensor immune to temperature fluctuations could be demonstrated.

The fact that the hollow hole in the IPHT-256b2 fiber is in the center of the fiber core, and therefore in the center of the guided mode, makes the sensitivity of a FBG higher when compared to evanescent field sensing. For a temperature independent refractive index sensor, two FBGs fabricated in the IPHT-256b2 fiber could be spliced in such a way that one has the hollow holes sealed while the other has the holes open. In this case the first FBG would be sensitive to temperature according to the results reported in Fig. 3.10, while the second FBG would be sensitive to temperature and refractive index of the material, hence enabling a temperature independent index determination.

Chapter 4

Bragg grating waveguides in fused silica

Bragg gratings, specifically gratings in waveguide devices, have been shown to have numerous applications since the invention of the first fiber Bragg gratings (FBGs) [78]. The Bragg grating waveguides (BGWs) shown in this chapter are Bragg gratings that simultaneously form a waveguide. Their applications match those of their FBG counterparts, with the advantage of being fabricated in bulk glass and being integrated with other components like microfluidics [34], or uniform waveguides, to form more complex structures. Furthermore, these BGWs are point-by-point written devices and their modulation (grating) component and their waveguide (average effective index) component are both achieved in a single fabrication process. This is in contrast to the standard technique used for FBGs where the grating component is fabricated, typically by side interferometric illumination [79], after the original background waveguide was formed.

The gratings presented here can be used as narrow linewidth Bragg mirrors for sensing applications, like temperature or strain sensing [80], in laser structures such as distributed feedback lasers (DFBs) [10], integrated into optofluidics sensing structures [81, 82, 83], etc. The improvement of the current system to include enhanced spectral controls, like the inclusion of chirp and phase-shifts, further upgrades the toolkit of devices available, opening the opportunity for integration of advanced pulse shaping features together with the already established functionalities.

4.1 Background

The acousto-optic modulator (AOM) was used in the femtosecond laser fabrication system (Fig. 2.2), as described in Section 2.1, as a fast *on/off* switch, to enable the modulation of the femtosecond beam for the fabrication of BGWs. The electrical AOM modulation electrical signal is computer controlled and synchronized with the movement of the XYZ motion stages, as shown in Fig. 2.3, by a position-synchronized output (PSO). This serves the purpose of enabling or disabling the laser beam depending on the sample position, in order to define waveguide segments or gaps.

The AOM can be controlled by either a digital (Neos 21080-2DS) or an analog (Neos 21080-2AS) RF driver; the digital driver was the one most commonly used in this work and allows for simply switching between *on* and *off* states, while the analog driver allows for the definition of intermediate RF voltage steps which control the AOM efficiency, and therefore provide variable laser power between the *off* state and the maximum power.

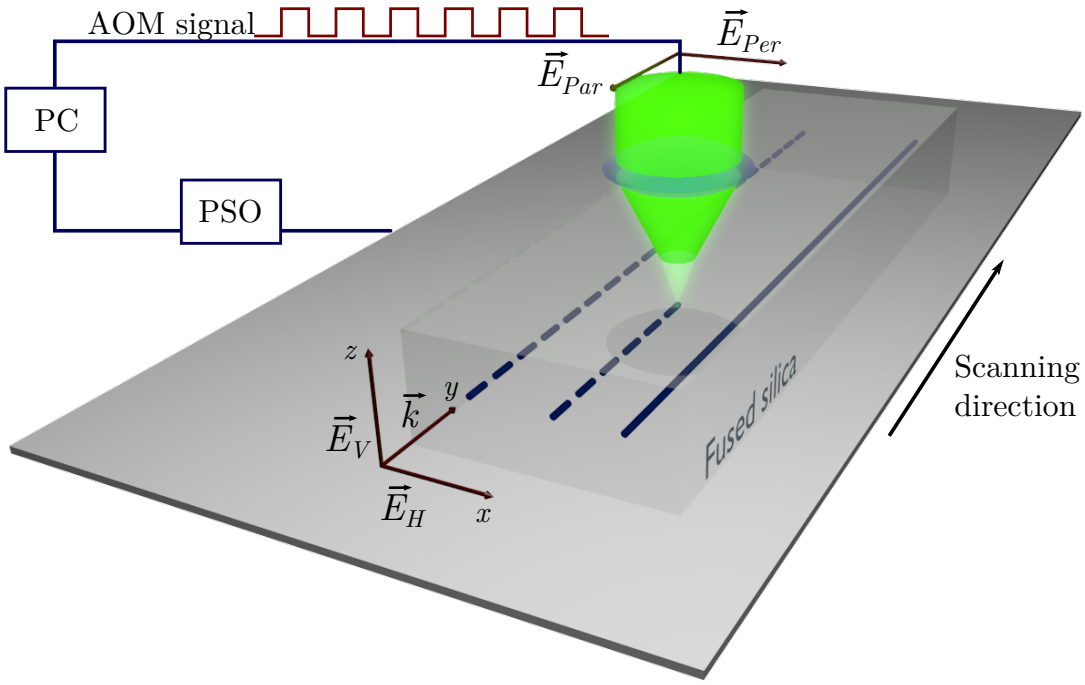

Figure 4.1: Representation of the BGW fabrication principle.

For the fabrication of uniform BGWs [8], the AOM is driven by a square wave with a given frequency smaller than the laser repetition rate, producing burst trains of femtosecond pulses that in turn create volumetric pixels (voxels) of increased refrac-

tive index. These voxels form an uniformly segmented waveguide with a periodicity (Equation 4.1) that depends on the ratio between the linear scan speed of the motion stages, v, responsible for defining the waveguides, and the AOM signal frequency, f.

$$\Lambda = \frac{v}{f} \tag{4.1}$$

For low repetition rate systems, the ratio between the scan speed and the repetition rate of the laser can also be used to define a segmented waveguide and produce a Bragg grating [84]. The duty cycle, which is defined as the ratio between the *on* time interval and the period of the modulation signal, is also a key parameter in optimizing the gratings fabrication. A lower duty cycle increases the contrast between the refractive index voxels and the surrounding glass which in turn increases the strength of the Bragg reflection peak. However, the increased grating strength also increases the propagation losses (specially radiation mode loss, see Fig. 4.2), while a higher duty cycle provides a closer resemblance to a standard[1] waveguide, which has lower loss but weaker reflection. The grating length is the other parameter that influences the BGWs strength, as longer gratings will have higher reflection, but also produce higher total loss. A duty cycle value of 60% has been found [8] to be a good compromise between the grating strength and the loss, for centimeter long devices. A representation of two Bragg grating segmented waveguides and a uniform non-BGW waveguide is shown in Fig. 4.1.

These Bragg structures have similar applications as FBG, while the bulk glass platform provides an ideal medium for integration towards lab-on-chip devices. For example, sensing applications, together with microfluidics, have already been demonstrated [82]. With appropriate programming, this technique is capable of controlling the laser power at the sample location for each index voxel. This capability enables true point-by-point fabrication capabilities for tailoring the spectral response of BGWs to suit different needs. Chirped, phase-shifted, apodized, and any combination of segmented structures can all be fabricated without the need for designing specific phase masks for each device. This makes this system ideal for prototyping devices with application in signal processing, temporal pulse shaping, etc.

[1] A standard waveguide is a non-modulated or unmodulated waveguide. A 100% duty cycle applied in the fabrication of a BGW would be equivalent to a non-modulated waveguide.

Figure 4.2 shows the transmission and reflection spectra of a BGW fabricated with a duty cycle of 60%, a modulation frequency of 500 Hz and a scanning speed of 0.268 mm/s. The transmission dip located to the left (lower wavelength side) of the main Bragg resonance is due to radiation mode loss, and therefore is not present on the reflected spectrum.

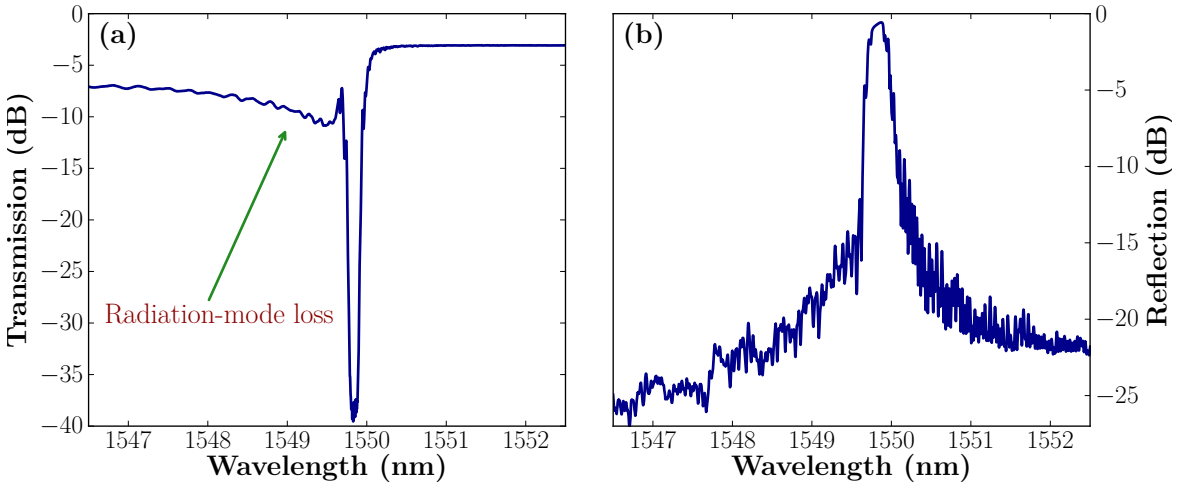

Figure 4.2: (a) Transmission and (b) reflection spectra of a BGW. The radiation mode loss is visible in transmission but not in reflection, as expected. *Courtesy of Jason R. Grenier.*

This radiation mode loss follows the same mechanism responsible for the coupling to cladding modes in FBGs [85, 86, 87, 88], where typically type II gratings produce significant losses for wavelengths shorter than the Bragg resonance, while transmitting longer wavelengths [89, 90].

The reflection peak in Fig. 4.2(b) and the transmission depth in Fig. 4.2(a) correspond to the resonance measured in reflection and transmission, respectively, of the BGW segmented structure. The resonance corresponds to the Bragg wavelength and can be calculated based on the Bragg relation shown in Equation 4.2, where λ_B is the Bragg wavelength, n_{eff} is the effective index of the waveguide mode and Λ is the periodicity of the BGW, which depends on the fabrication condition obtained from Equation 4.1.

$$\lambda_B = 2\Lambda n_{\text{eff}} \tag{4.2}$$

Based on theses conditions ($v = 0.268$ mm/s and $f = 500$ Hz), the periodicity of this BGW, Λ, is 536 nm; this value, together with the measured λ_B =1550 nm, infers an effective refractive index, n_{eff}, of 1.446.

The BGWs shown here can therefore be used to determine the chromatic dispersion characteristics of femtosecond fabricated waveguides, by determining the effective index as a function of the Bragg wavelength, using Equations 4.1 and 4.2.

Figure 4.3 shows the results, summarized in Table 4.1, of the effective index measured for BGWs fabricated with different AOM frequencies, compared to the index of refraction of bulk fused silica, determined according to the Sellmeier equation shown in detail in Appendix B. The Bragg wavelength measurements have an uncertainty of 0.2 nm, which corresponds to the BGW bandwidth (full width at half maximum (FWHM)) and produces an average uncertainty of 0.0002 in the effective refractive index determination over the wavelength range of interest (1300 nm – 1650 nm).

Table 4.1: BGWs dispersion compared to fused silica dispersion.

AOM frequency (Hz)	Bragg wavelength λ_B (nm) ±0.2 nm	Effective index ±0.0002	Fused silica index (Corning 7980)
595	1305.9	1.4488	1.4469
574	1353.1	1.4482	1.4463
533	1455.6	1.4466	1.4451
500	1550.5	1.4456	1.4440
484	1601.0	1.4449	1.4434
470	1647.9	1.4442	1.4428

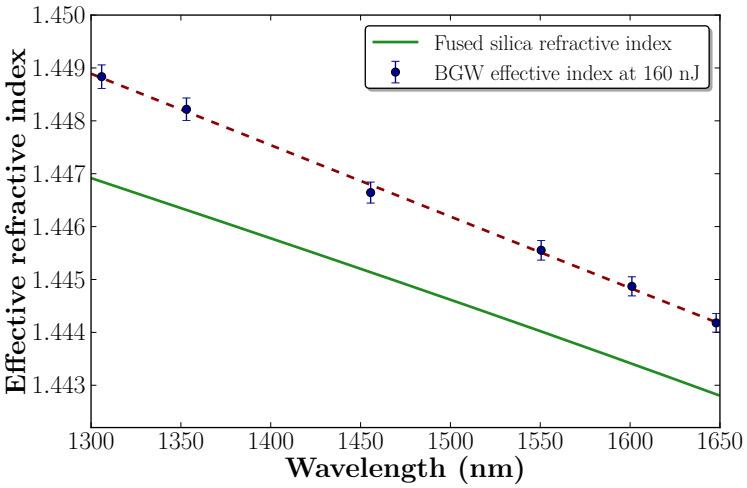

Figure 4.3: Measured effective index of BGWs as a function of wavelength, compared to the refractive index of fused silica.

4.2 Chirped BGWs

In chirped BGWs, the periodicity of the Bragg structure changes as a function of the position in the waveguide. This can be achieved by either changing the scanning velocity, through the application of a constant acceleration to the motion of the sample, or by changing the AOM frequency as a function of the position along the grating. The method of accelerating the motion stages has been used in the past [80]; however, extra loss was introduced. For example, a chirped BGW with a 20 nm bandwidth can exhibit twice as much propagation loss when compared to a 0.2 nm bandwidth grating due to the waveguide inhomogeneities created by the acceleration of the motion stage.

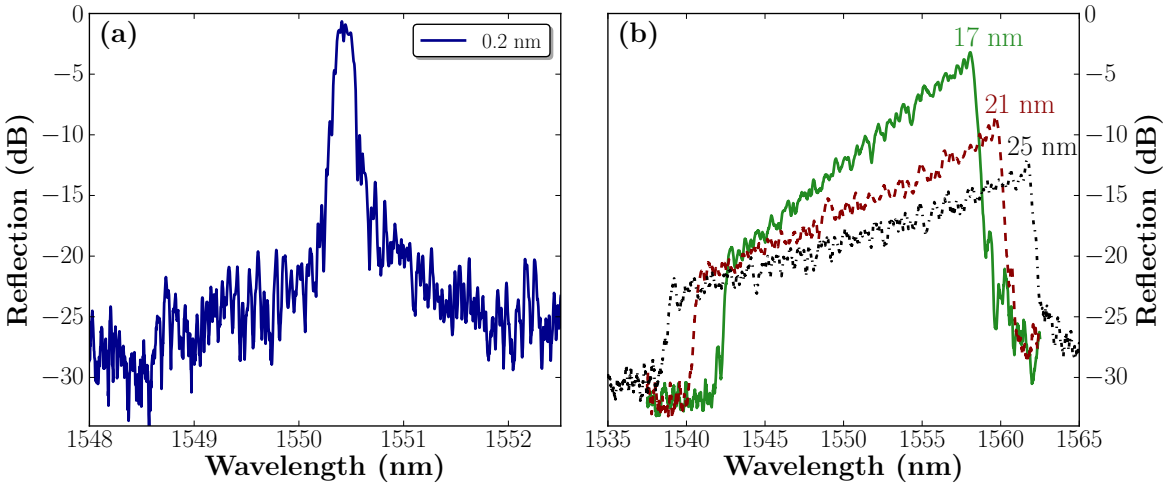

Figure 4.4: Reflected spectrum of (a) uniform BGW and (b) chirped BGWs with different bandwidths, all fabricated in a 5.08 cm sample. The BGWs in (b) have chirp rates[3] of 1.16 nm/cm, 1.43 nm/cm, and 1.70 nm/cm for the 17 nm, 21 nm, and 25 nm bandwidth chirps, respectively.

Figure 4.4(a) shows the reflected spectrum of a uniform, non-chirped BGW written with 0.26815 mm/s scan speed and 500 Hz modulation frequency over a 50.8 mm long glass substrate side. This combination produces a grating with a period of $\Lambda = 536.3$ nm and a Bragg wavelength of (1550.5±0.2) nm, measured from the spectrum of Fig. 4.4(a). The 0.2 nm is the narrowest bandwidth of a uniform BGW reproducible with this method (while probed with unpolarized light). Based on the Bragg relation in Equation 4.2 and on the measurements and fabrication conditions mentioned, the effective index of the waveguide, n_{eff}, was calculated to be 1.4456±0.0002.

[3]The chirp rate is defined as the variation of the grating period per unit length, $\Delta\Lambda/\Delta L$.

To fabricate the chirped BGWs shown in Fig. 4.4(b), the AOM frequency was externally controlled by a function generator, capable of providing a linear frequency chirp around 500 Hz with 0.001 Hz resolution. The frequency depends on the main AOM frequency and on the target bandwidth desired for the chirped BGW, according to the approximation of Equation 4.3.

$$\Delta f \approx f \frac{\Delta \lambda_B}{\lambda_B} \tag{4.3}$$

For the chirped BGWs shown in Fig. 4.4(b), with bandwidths of 17 nm, 21 nm, and 25 nm, frequency variations of 5.484 Hz, 6.774 Hz, and 8.065 Hz around the main modulation frequency of 500 Hz were used, respectively.

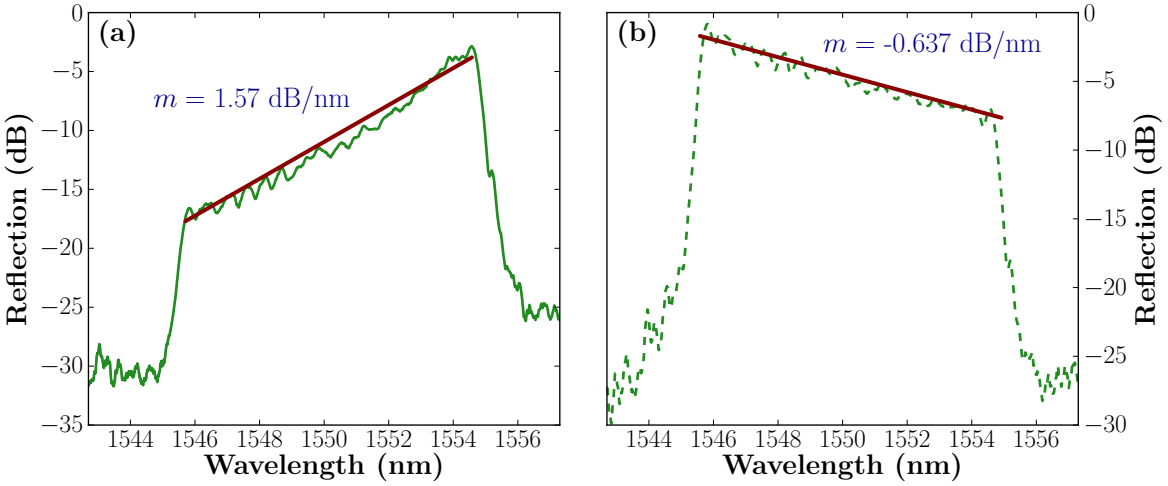

Figure 4.5: Reflected spectrum of chirped BGWs with 10 nm bandwidths probed in two different directions. (a) Spectrum probed from the waveguide side which corresponds to the higher period of the chirped grating and (b) spectrum probed from the waveguide side which corresponds to the lower period of the chirped grating.

The reflectivity of the chirped BGW changes within the grating bandwidth due to the waveguide loss, and therefore the change with wavelength depends on which side the waveguides are probed from. Figure 4.5 shows the responses of a 10 nm bandwidth BGW fabricated with a linear frequency chirp of 3.226 Hz centered at 500 Hz, that produced a grating with a period variation of (3.46±0.07) nm. In Fig. 4.5(a) the waveguide is probed from the side of the sample corresponding to the high wavelength side of the spectrum, while in Fig. 4.5(b) the probing is done from the opposite side, corresponding to the low wavelength side of the spectrum.

The difference observed in the absolute value of the slope between the two chirped structures in Fig. 4.5 is due to the contributions of radiation mode loss, which occurs at the short wavelength side of the spectrum (Fig. 4.2): while the spectrum in Fig. 4.5(a) is affected by both propagation losses and radiation mode loss (causing the nonlinearity in the slope), the reflection in Fig. 4.5(b) is only affected by the propagation losses. To confirm the origin for this asymmetry, we can evaluate the propagation loss, using the values of the slope m from Fig. 4.5(b), the device length, $L = 50.8$ mm, and the grating bandwidth, $\Delta\lambda = 10$ nm, according to Equation 4.4.

$$\alpha = \frac{m\Delta\lambda}{2L} \tag{4.4}$$

The value found for the propagation loss was $\alpha = 0.63 \pm 0.03$ dB/cm, which compares well with the 0.7 dB/cm obtained by the fiber coupling method, described in Section 2.3, for this device.

This point-by-point spectrum control can be used for pulse shaping applications. The chirped BGW shown in Fig. 4.5 was used to demonstrate the first integrated temporal Fourier transformer produced in bulk fused silica glass with a femtosecond laser [91].

The temporal Fourier transformer relies on the fact that the phenomena of paraxial (Fresnel) diffraction of monochromatic optical beams and narrow-band dispersion of optical pulses [92] can be described by mathematically identical equations.

It is thus possible to achieve effects similar to those that exist in space in the temporal domain. Using the first-order chromatic dispersion introduced by the chirped BGW, it is possible to map the energy spectrum of the input optical signal to the output temporal waveform.

Real-time Fourier transformation based on linear dispersion can be used for real-time optical spectrum measurements [93, 94], temporal magnification of broadband waveforms [95], high-frequency arbitrary microwave waveform generation [96], real-time spectroscopy [97], complex-field characterization of low intensity ultrafast optical waveforms [98], and programmable optical pulse shapers with ultrahigh update rates [99].

A simulation of the reflectivity and group delay of the chirped BGW is shown in Fig. 4.6(b, c), respectively, obtained by the transfer matrix method and accounting

for the known propagation loss. The refractive index of the grating is represented by Equation 4.5.

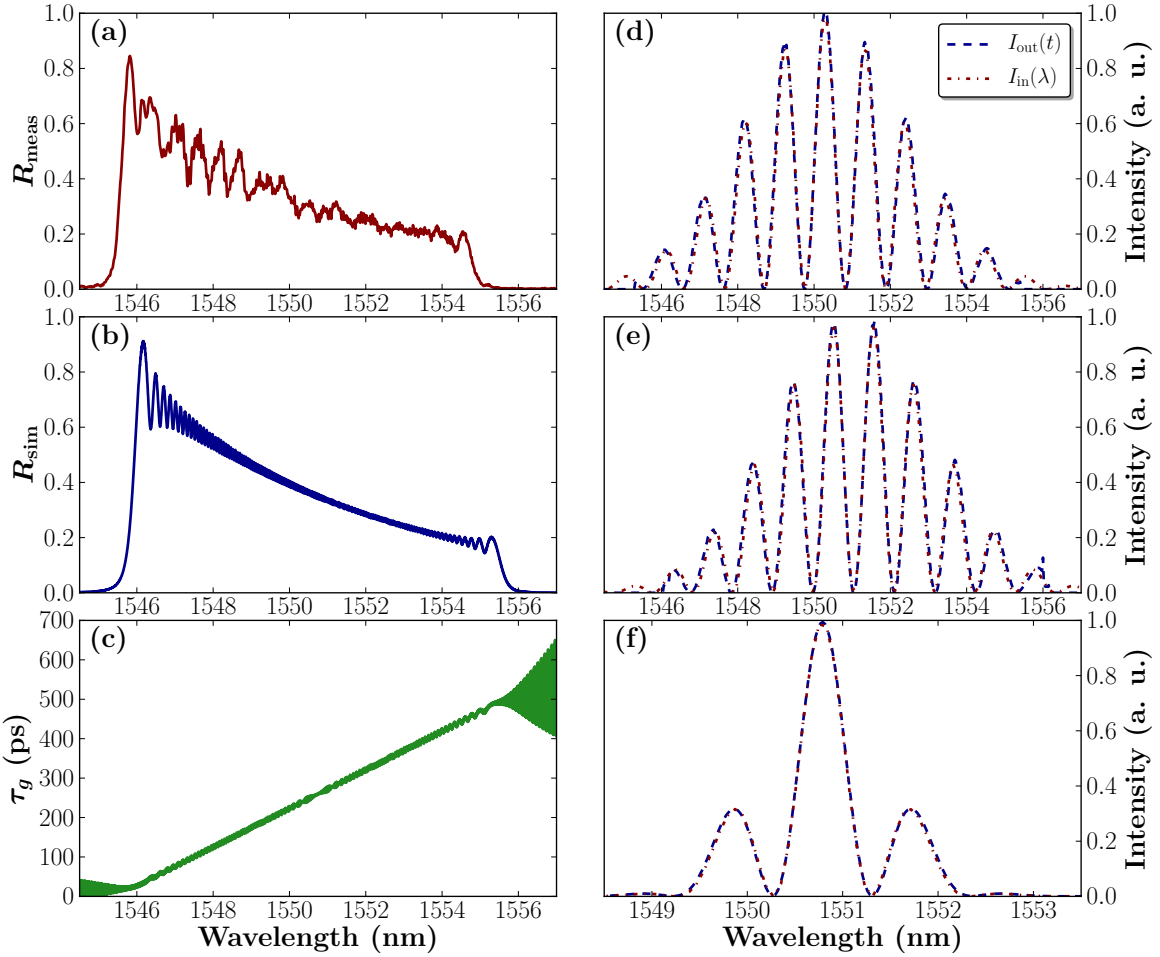

Figure 4.6: (a), (b) Reflectance spectra of a chirped BGW: (a) measured (R_{meas}), (b) simulated (R_{sim}). (c) Simulated group delay of the chirped BGW. (d)–(f) Simulated incident spectra (- - red dashed lines) and reflected temporal waveforms (- - blue dashed lines): (d), (f) for in-phase and (e) π-phase shifted incident pulses. The simulation results shown in (d), (e) and (f) correspond to the experimental data presented in Figs. 4.8(a), 4.8(b), 4.8(c), respectively. *Courtesy of Ksenia Dolgaleva [91].*

$$n(z) = n_{\text{eff}} + \eta(n_{\text{dc}} + n_{\text{ac}}[1 + \cos(\theta(z))]) \tag{4.5}$$

Here, $\theta(z)$ is related to the position-dependent period of the grating $\Lambda(z)$ according to $\Lambda(z) = 2\pi/(d\theta(z)/dz)$; $n_{\text{eff}} = 1.4452$ is the effective refractive index of the mode of the waveguide in the absence of the periodic index modulation of the grating; $n_{\text{dc}} = 10^{-2}$

and $n_{ac} = 2.83 \times 10^{-3}$ are the *dc* refractive index change and the amplitude of the *ac* refractive index variation in the BGW core, respectively; and $\eta = 0.06$ is the fraction of the modal power within the waveguide core boundaries. A linear dispersion coefficient of $\Phi_\lambda \approx 48$ ps/nm was found from the simulated group delay.

By using the reflection spectrum of the 10 nm band chirped BGW, a temporal Fourier transformer operation can be accomplished for pulses as short as 20 ps [100]. The experimental demonstration of this application was done by colleagues in the *Institut National de la Recherche Scientifique* (INRS) using the fourier transform spectral interferometry (FTSI) technique [101] and measuring intensity and phase of the reflected waveform. This technique does not provide real-time measurements like others [102], but requires less reflected power when compared to other techniques [103, 104].

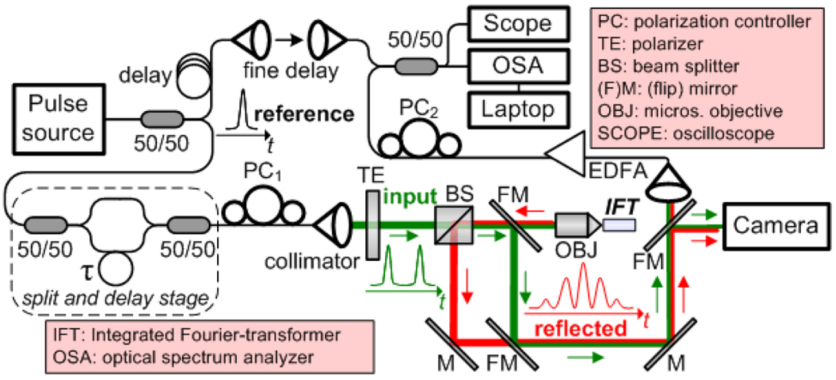

Figure 4.7: Experimental setup for the measurement of pulse shaping with a chirped BGW. *Courtesy of Ksenia Dolgaleva [91].*

The experimental setup for this demonstration is shown in Fig. 4.7, and consists of a tunable passively mode-locked fiber laser source with a switchable optical bandpass filter (OBPF), which generates pairs of in-phase and π-phase shifted pulses. These pulses are coupled into the chirped BGWs and the reflected output is recorded (Fig. 4.8).

Figures 4.8(a, b) show the spectra of the incident and reflected signals for a 5 nm OBPF with the scaled temporal reflected signals for the in-phase and π-phase shifted pulse cases, respectively. Figure 4.8(c), shows the spectrum with a 3 nm filter in the fiber source for the reflected signal and the scaled temporal waveform for in-phase pulses. The pulse duration was ≈1.2 ps while the output temporal duration was ≈150 ps. Figure 4.8(d) shows the reconstructed phase of the reflected signal, and demonstrates the waveform Fourier transform operation.

The simulation results are in agreement with the experimental results, as demonstrated by the comparison between the simulated reflected temporal waveforms and the incident spectra shown in Fig. 4.6(d, e, f), which correspond to the results presented in Fig. 4.8(a, b, c).

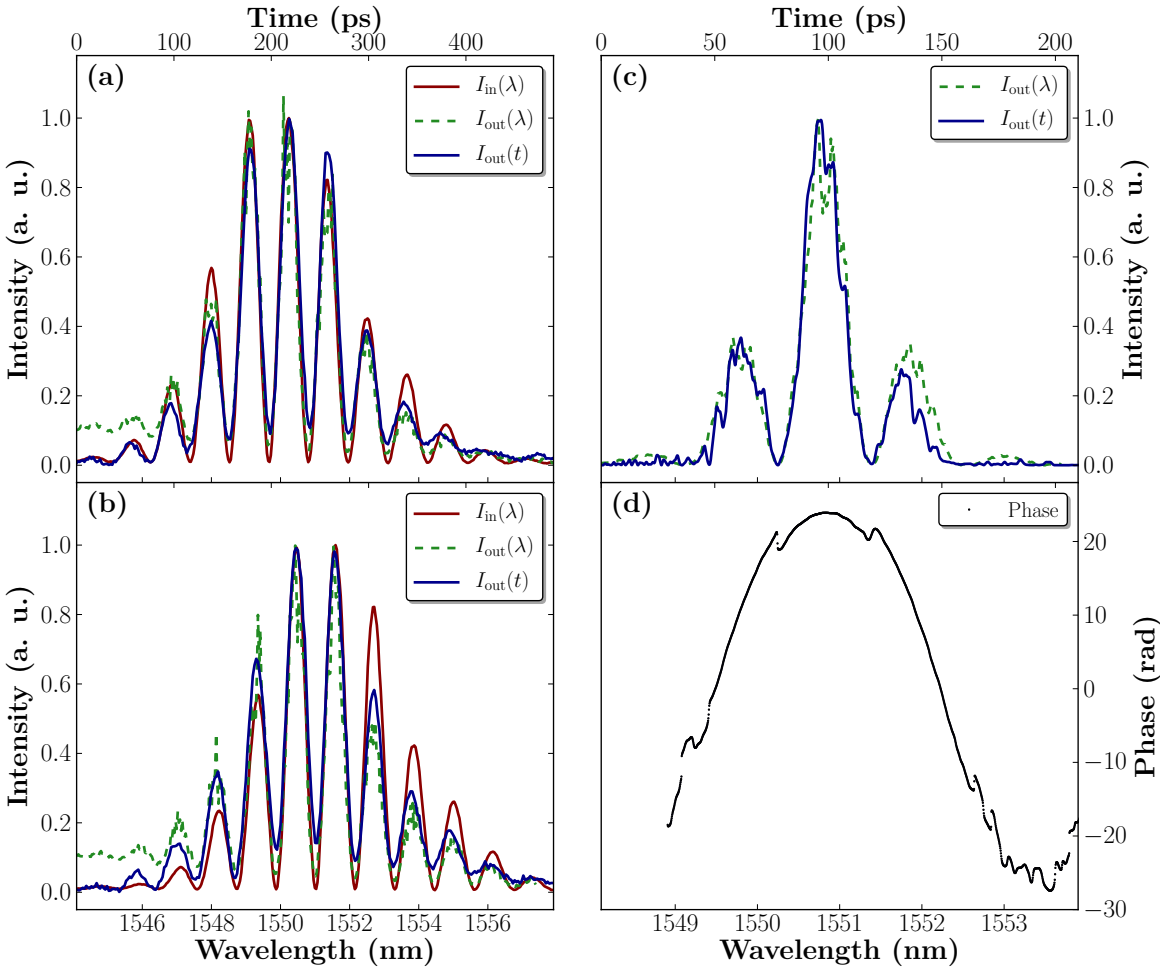

Figure 4.8: Incident (– solid red curve) and reflected (- - dashed green curve) spectra superimposed on the scaled oscilloscope traces of the output temporal waveforms (– solid blue curve), obtained with a 5 nm OBPF: (a) for the in-phase incident pulses and (b) for the π-phase shifted incident pulses. (c) Spectrum (- - dashed green curve) and the scaled temporal waveform (– solid blue curve) of the reflected in-phase double pulse signal reconstructed through FTSI, obtained with a 3 nm OBPF. (d) The phase of the reflected signal reconstructed through FTSI. *Courtesy of Ksenia Dolgaleva [91].*

4.3 Phase-shifted BGWs

For the introduction of phase shifts in the BGW and the definition of phase shifted Bragg grating waveguides (PSBGWs), the AOM signal can be modified in two ways. The position-synchronized output (PSO) can be used directly, taking advantage of the features available in the Aerotech ABL1000 motion stage, or the AOM signal can be computer controlled externally in the same way the function generator was used to fabricate the chirped BGWs. By using the PSO features of the motion stage, a precise phase shift can be introduced anywhere along the waveguide structure. But there are systematic errors in the PSO system that make the designed time shift to translate into a real time shift at the sample position that depends on the grating length. For this reason, for different BGW lengths, a separate compensated shift parameter has to be found to provide the desired result. The PSO is also limited in the number of grating features that can be included at the same time to define the BGW structure, which may be challenging for the fabrication of more complex gratings, like the ones required for the inclusion of phase shifts together with chirp. These limitations can be overcome by externally generating the AOM signal, and using the PSO only to provide trigger signals to start and stop each waveguide fabrication. With this approach, virtually any AOM amplitude signal as a function of time (or sample length) can be defined and used for the fabrication of complex structures[4].

Furthermore, the development of externally computer controlled AOM signals offers more flexibility for fast prototyping, which can open the door to point-by-point fabrications of structures that are traditionally difficult to obtain with standard lithography fabrication techniques, and that typically require the fabrication of expensive phase masks, specifically designed and manufactured for a single structure.

In order to demonstrate the fabrication capabilities of this system, gratings with different phase shifts ($\frac{\pi}{2}$, π and $\frac{3\pi}{2}$) were fabricated and their reflection spectra are shown in Fig. 4.9. Both reflection and transmission spectra are shown in Fig. 4.10, for another experimental sample.

For Fig. 4.9, the fiber characterization system described in Section 2.2 (Fig. 2.6) was used with the addition of polarization control paddles and an in-fiber polarizer, in

[4]The PSBGWs demonstrated in this chapter were fabricated using the two techniques described above and the results were similar, confirming that the only difference between the two approaches was the flexibility and fast prototyping capabilities that the latter approach provided.

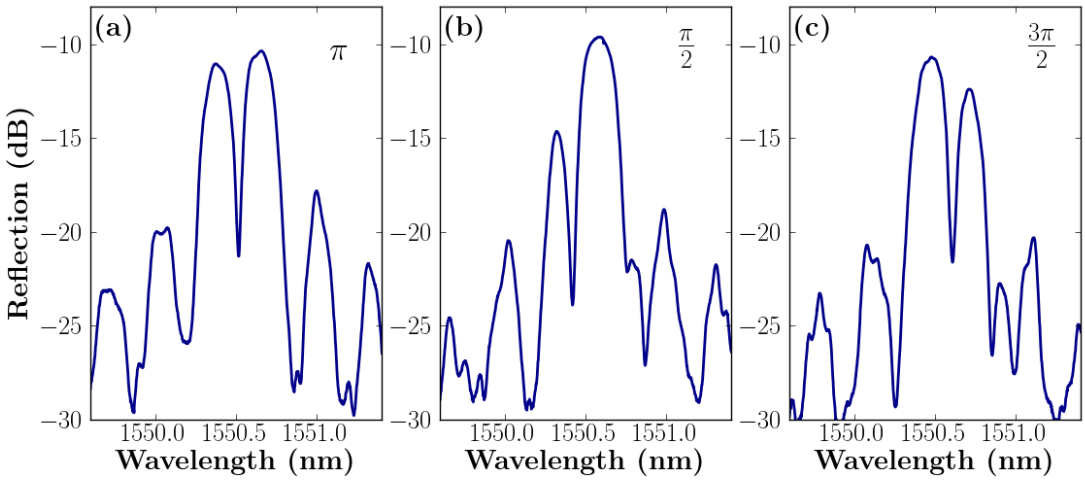

Figure 4.9: Reflection spectra for 2.54 cm long PSBGWs with phase shifts in the middle of the waveguide with values of (a) π-phase shift, (b) $\frac{\pi}{2}$ phase shift, and (d) $\frac{3\pi}{2}$ phase shift.

order to record the spectrum with the optical spectrum analyzer (OSA) at 0.01 nm resolution and with polarization control[5].

Figure 4.9 confirms the existence of transmission peaks within the gratings stopbands, with their position depending on the magnitude of the phase step. These peaks have the same approximate bandwidth as the OSA resolution and, therefore, a higher wavelength resolved measurement technique should be used in order to gain sufficient knowledge about these features. For this reason, Fig 4.10 was recorded using the same fiber characterization system, but using a tunable laser system with 1 pm resolution.

More advanced features are demonstrated in Fig. 4.12, where five cascaded π-PSBGWs were combined in order to obtain a rectangular shaped passband. The π-shifts were positioned along the BGW between six segments with length ratios of 1:2:2.17:2.17:2:1 following the design presented in [106]. A schematic of this design is shown in Fig. 4.11.

This structure was theoretically predicted to have a passband ripple of 0.3 dB and a quality factor of 0.85 [106]. The quality factor is defined as the ratio between the bandwidths measured at -1 dB and - 10 dB, $s = \frac{B_{-1}}{B_{-10}}$ ($s = 1$ for a perfect, rectangular shaped filter). The performance of the BGW transmission (Fig. 4.12(a)) and reflection

[5]The birefringence present in the PSBGWs is on the order of the linewidth of the features shown in Fig 4.9. In order for these features to become apparent, linearly polarized light aligned with the polarization eigenmodes of the waveguides had to be used. This birefringence will be explained in more detail in Section 4.4.

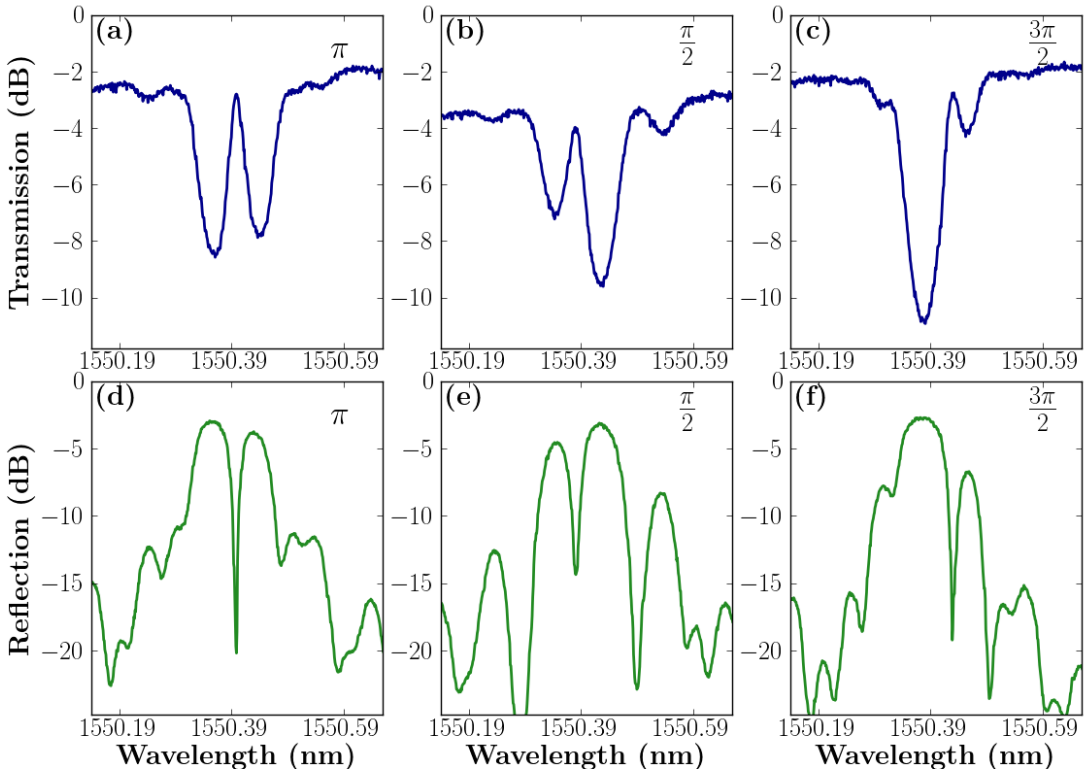

Figure 4.10: Transmission (blue curve: a, b and c) and reflection (green curve: d, e and f) spectra for PSBGWs with (a, d) π-phase shift, (b, e) $\frac{\pi}{2}$ phase shift, and (d, f) $\frac{3\pi}{2}$ phase shift. *Courtesy of Jason R. Grenier [105].*

(Fig. 4.12(b)) spectra showed a passband ripple of 0.46 dB and a quality factor of 0.7, which was 3.5 times larger than the quality factor obtained for single π-PSBGWs.

The measurements performed on all PSBGWs and shown in Fig. 4.10 and Fig. 4.12 were obtained by using linearly polarized light (aligned with the vertical, V, polarization eigenmode). This was done because the birefringence present in the waveguides fabricated in fused silica by our femtosecond writing technique prevents the observation of the sharp spectral features of these devices. Furthermore, these sharp features may also be used to measure the waveguide birefringence by comparing the Bragg wavelengths obtained with linearly polarized probe light in the polarization eigenmodes of the sample. Figure. 4.13(a) shows the reflected spectra of a π-PSBGWs measured with light polarized in the horizontal, H, and the vertical, V, directions. From the polarization split observed in this figure, a birefringence value of $(7.5 \pm 0.3) \times 10^{-5}$ was inferred from the 80±3 pm wavelength difference measured.

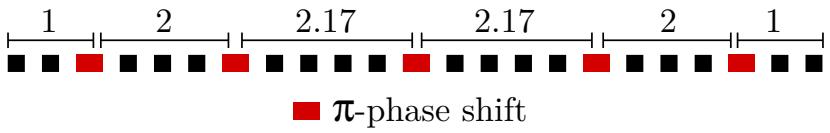

Figure 4.11: Schematic of a BGW with five cascaded π-shifts.

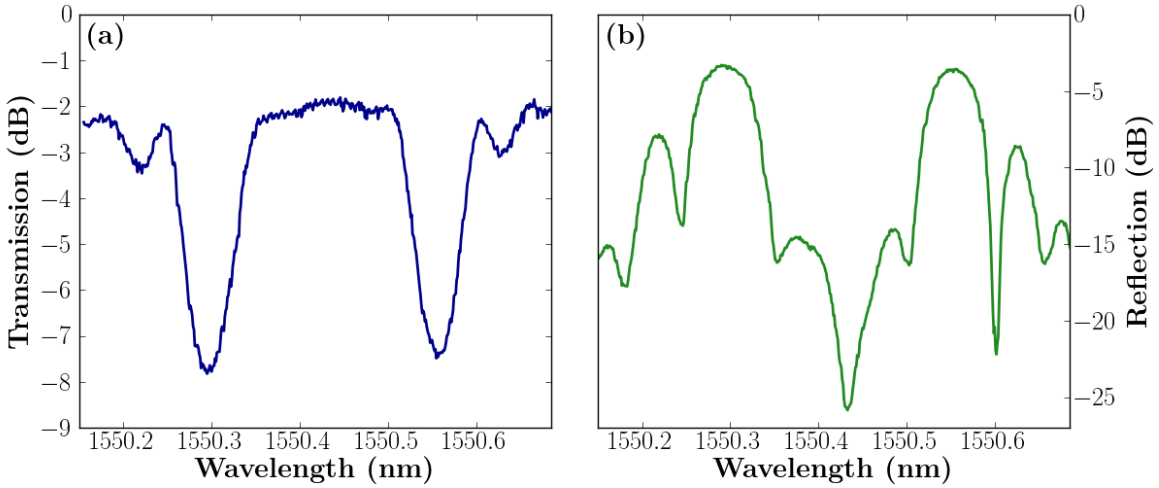

Figure 4.12: Spectra measured with vertically polarized light for transmission (a) and reflection (b) of a BGW with five cascaded π-phase shifts. *Courtesy of Jason R. Grenier [105].*

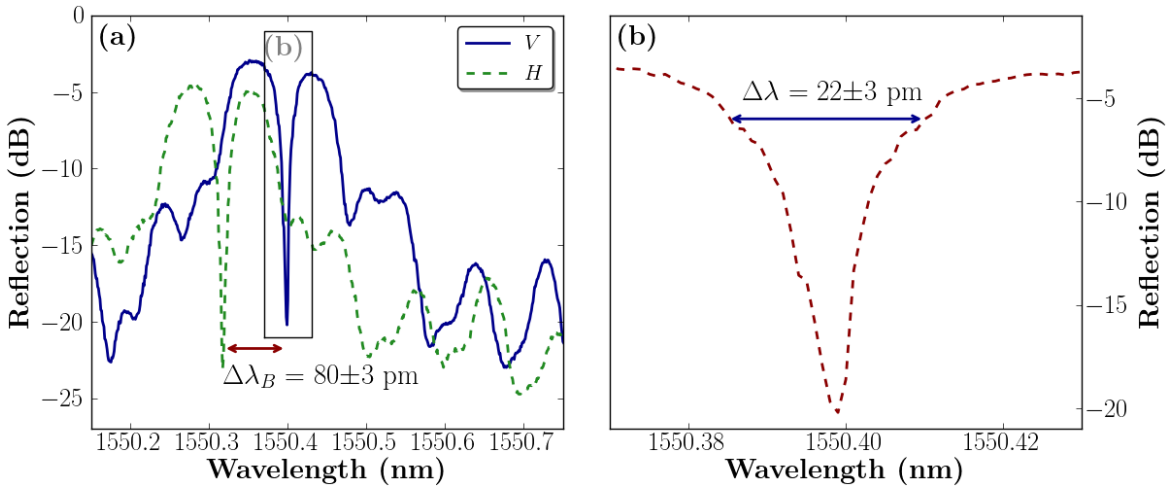

Figure 4.13: (a) Reflection spectra of a π-PSBGWs measured with vertical, V, (blue solid line) and horizontal, H, (green dashed line) polarized light. (b) V polarized reflection spectrum of the π-PSBGWs transmission line with a bandwidth of 22±3 pm measured at the 3 dB point. *Courtesy of Jason R. Grenier [105].*

All spectra were measured using the free-space setup described previously and with a swept wavelength system (JDS Uniphase SWS2000, which has a spectral resolution of 3 pm), and a detector (instead of the broadband source and the OSA).

4.4 Birefringence measurements

One of the key applications found for the BGWs in this work was the measurement of waveguide birefringence. The Bragg wavelength is dependent on the effective index of the waveguide mode (Bragg relation 4.2). Almost all the waveguides studied were shown to be single mode; however, they are also birefringent. Because of that birefringence, there is a polarization degeneracy in the fundamental waveguide mode, which in turn produces two Bragg reflections instead of one. If the birefringence is of the same order of magnitude, or larger, than the BGW bandwidth then this degeneracy becomes clear even when spectrally probing a BGW with unpolarized broadband light.

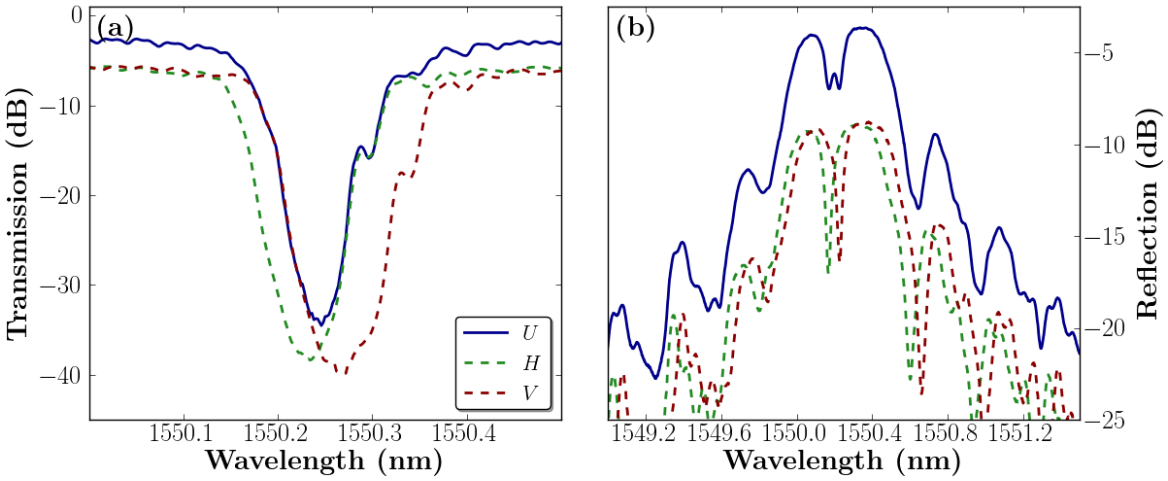

Figure 4.14: (a) BGW transmission spectra and (b) π-PSBGW reflection spectra, probed with unpolarized light, U, vertical, V, and horizontal, H, linearly polarized light.

A complete algorithm used to automatically determine the birefringence from the wavelength split of the two recorded transmission or reflection polarization eigenmodes is described in detail in Appendix A.

4.5 Conclusions

The femtosecond BGW writing technique was further improved, building on already established procedures, with computer controlled AOM modulation for the fabrication of chirped and phase-shifted Bragg gratings. This point-by-point fabrication technique has the ability to produce first order grating structures due to the temporal resolution provided by the AOM modulation, and to the spatial resolution provided by the non-linear absorption process. These devices have proven to be excellent tools for sensor applications and also for the measurement of waveguide birefringence, where the absolute results obtained complement and provide a clear advantage in comparison with more standard techniques, which produce degenerate results and phase ambiguities.

The radiation mode loss found for strong BGWs is currently being explored for the design of integrated edge filter devices, while the Bragg grating writing system was demonstrated for fabrication in the cladding of optical fibers [107].

Devices were successfully used for pulse shaping applications [91], demonstrating the ability to implement a temporal Fourier transformer, in both amplitude and phase, of picosecond optical pulses, enabling the opportunity to explore more complex ultrafast pulse processing devices.

Phase-shift BGWs were demonstrated [105, 108] with sharp features from π-shift gratings with bandwidths as small as 22 pm. This precise control may enable the design of high resolution sensors or the ability to perform integrated temporal differentiation of optical signals [109].

Chapter 5

Birefringent waveguides in fused silica

In this chapter, the waveguide birefringence[1] *was explored for the development of functional polarization devices, such as polarization beam splitters and wave retarders.*

The effects of the laser interactions with the material and the origins of the birefringence were studied and the presence of nanogratings, formed in the waveguide core and oriented perpendicularly to the writing laser polarization, was found to contribute strongly to the waveguide birefringence, depending on their orientation with respect to the waveguide writing direction. The introduction of stress inducing laser modification tracks was employed for further birefringence control.

[1]The birefringence is defined as the difference between the index of refraction between two eigenaxes of polarization. For the purpose of this work, the birefringence will be the difference between the *effective* index of two waveguide polarization eigenmodes and referred to as Δn or Δn_{eff}.

5.1 Background

Directional couplers with a low polarization dependence have been demonstrated in borosilicate glass (Corning Eagle2000) [6], where heat accumulation effects have been shown to yield low birefringence waveguides [23]. In fused silica, however, heat accumulation effects do not occur for the same laser writing conditions found to be optimum in borosilicate glass, leading to less symmetric waveguides where stresses have been found to affect the birefringence and the waveguides loss [42, 110, 111]. Further, waveguides fabricated in fused silica show birefringence that depends strongly on both the polarization and the intensity of the writing beam [112]; in addition, it has been shown that there is a strong correlation between the laser induced nanogratings and the waveguide form birefringence [113, 114, 115].

The strong induced birefringence created by the nanograting effects has already been explored in bulk glasses and used for the formation of computer generated holograms [116, 117], polarization diffraction gratings [118], birefringent elements [119], and the use of this technology for 5D optical storage has been suggested [120].

Fused silica is the material of choice for telecommunication and other optical applications due to its high transmission and stability. Hence, understanding and controlling the formation of nanogratings is essential if we are to exploit polarization control in three-dimensional integrated circuits. By carefully controlling the laser exposure parameters, such as pulse energy, scanning speed and polarization, the waveguide birefringence can be controlled and applied to fabricate polarization dependent devices. Such devices have recently been proposed [121] for application in integrated quantum entanglement experiments [122, 123], where beam splitters have been formed in bulk fused silica or borosilicate glasses as an alternative to lithographic processing of silica-on-silicon optical circuits [124].

5.2 Wave retarders

In this section, a controlled polarization retardance in the 1250 nm to 1650 nm wavelength region is demonstrated using waveguides and Bragg grating waveguides (BGWs) fabricated with the methods described in Section 2.1. Such devices open the possibility to integrate, using a single fabrication step, polarization splitters and waveguide wave plates in bulk glass, paving the way for more complex and highly stable polarization devices to be integrated into three-dimensional optical circuits. Such polarization control is further required for differential polarization phase-shift keying in optical communication [125], quantum key distribution [126, 127] for cryptography applications and quantum computing [128].

5.2.1 Fabrication

The waveguides were fabricated using the femtosecond laser fabrication system described in Section 2.1. Exposure conditions tested were 300 fs pulse width, 500 kHz repetition rate and pulse energy between 80 nJ and 200 nJ at $\lambda = 522$ nm center wavelength. The beam was focused 75 µm below the surface of the fused silica substrates (Corning 7980, 50.8 mm × 25.4 mm × 1 mm with all faces optically polished) with a 0.55 NA aspheric lens. The sample was scanned at a constant speed of 0.27 mm/s, producing 24.5 mm long waveguides parallel to the short edge of the substrate.

The writing beam polarization state at the focus was oriented with a half-wave plate in the laser path to be either parallel (along the y-axis) or perpendicular (along the x-axis) with respect to the scanning direction as shown in Fig. 5.1, manipulating the form birefringence induced by the laser generated nanogratings.

BGWs were fabricated with the same laser exposure setup and with the addition of the acousto-optic modulator (AOM) in the laser path, as described in Chapter 4. The AOM frequency was varied from 595 Hz to 470 Hz to provide tuning of the waveguide Bragg reflection peak from 1300 nm to 1650 nm.

5.2.2 Characterization methods

The birefringence of the waveguides was determined by two complementary techniques both using free space, end-fire coupling of broadband light into the end facet of the

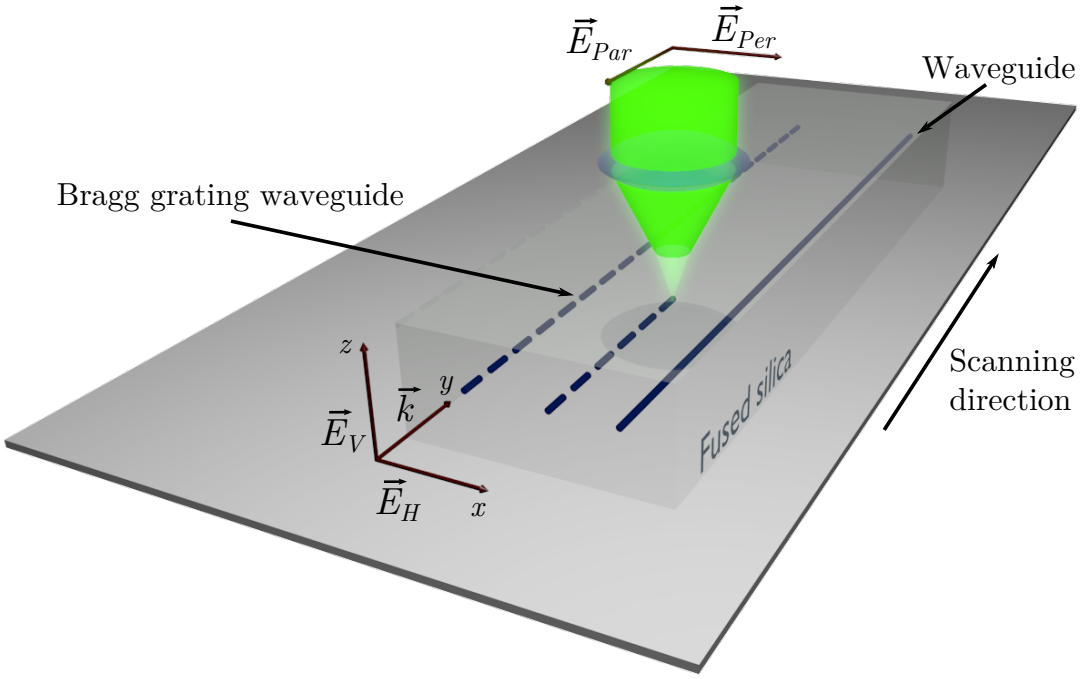

Figure 5.1: Schematic diagram of the waveguide fabrication, where $\vec{E}_{Par}$ and $\vec{E}_{Per}$ represent the parallel and perpendicular polarizations of the writing laser, respectively. $\vec{E}_V$ and $\vec{E}_H$ indicate the electric field orientation of Vertical, V, and Horizontal, H, waveguide polarization modes, respectively.

waveguide with an aspheric objective lens (New Focus, 30×, 0.4 NA) according to the the setup shown in Fig. 2.7.

In the first approach, the spectral splitting of the Bragg resonance in the BGWs was measured between the two perpendicular polarization modes, vertical, V (along the z-axis, slow axis, corresponding to the TM mode), and horizontal, H (along the x-axis, fast axis, corresponding to the TE mode), as defined in Fig. 5.1. The spectral splitting was measured by coupling a broadband light source (Agilent 83437A, 1250 nm to 1700 nm) to the waveguide and recording the light transmitted, reflected, or both, using an optical spectrum analyzer (OSA), Ando 6317B, set at 0.01 nm resolution. The polarization was controlled by rotating a broadband polarizer (Thorlabs LPNIR). Following the Bragg relation $\lambda_B = 2n_{\text{eff}}\Lambda$, where λ_B is the reflected Bragg wavelength, n_{eff} is the effective index of the mode and Λ is the period of the grating, one can obtain the waveguide birefringence, $\Delta n_{\text{eff}} = n_{\text{eff},V} - n_{\text{eff},H}$, according to Equation 5.1.

$$\Delta n_{\text{eff}} = \frac{\Delta\lambda_B}{2\Lambda} \tag{5.1}$$

Here, $\Delta\lambda_B$ is the difference between the Bragg resonance of the vertically and horizontally polarized modes which are the eigenmodes of the waveguide. The algorithm used for the extraction of the birefringence value from the recorded spectra is described in detail in Appendix A.

A second, more accurate measurement of the waveguide birefringence was made by using the crossed polarizers method. A broadband unpolarized light source was launched into a waveguide after passing a linear polarizer oriented at 45° with respect to the x-axis (Fig. 5.1); an OSA, set to a resolution of 2 nm, measured the waveguide output after passing a second broadband linear polarizer in two orthogonal orientations (45° and 135°).

The total waveguide output power, $P_o = P_{pm} + P_{cm}$, is split into parallel power P_{pm} and crossed power P_{cm} components measured at the respective 45° and 135° analyzer positions, which depend on the waveguide retardance, δ (Equation 5.2), according to Equation 5.3 and Equation 5.4 where the normalized powers P_p and P_c are defined.

$$\delta = \frac{2\pi L}{\lambda}\Delta n_{\text{eff}} \tag{5.2}$$

$$P_p = \frac{P_{pm}}{P_o} = \frac{1}{2}(1 + \cos\delta) \tag{5.3}$$

$$P_c = \frac{P_{cm}}{P_o} = \frac{1}{2}(1 - \cos\delta) \tag{5.4}$$

A similar birefringence analysis was presented in [112]. The retardance introduced by the waveguide can then be determined from Equation 5.5 within an ambiguous phase order of $m = 0, 1, 2, 3, ...$ to yield the birefringence, Δn_{eff}, as calculated by Equation 5.6, where, λ is the wavelength and L is the waveguide length.

$$\delta = \pm \arccos(P_p - P_c) + m2\pi \tag{5.5}$$

$$\Delta n_{\text{eff}} = \frac{\lambda\delta}{2\pi L} \tag{5.6}$$

The $m2\pi$ phase ambiguity and the $\pm$ sign in the arccosine function of the crossed polarizers method (Equation 5.5) can be solved by the less precise method of Bragg grating resonance splitting (Equation 5.1) which scales linearly with the waveguide birefringence.

To assess the various contributions to the total waveguide coupling and propagation loss, the intensity profile of the modes propagating in the waveguides was recorded by launching light from a tunable laser (Photonetics Tunics-BT) with a single mode fiber (SMF) into the waveguides and imaging the output onto a charge-coupled device (CCD) camera (Spiricon SP-1550M) through a 60× magnification lens.

5.2.3 Results

Laser exposure conditions in a range of 90 nJ to 160 nJ pulse energy for parallel writing polarization yielded waveguides with moderately low propagation losses, α, (0.3 dB/cm to 1.4 dB/cm) with a mode field diameter (MFD) that matches quite well to the 10.4 µm MFD of a SMF-28 fiber as indicated in Table 5.1. Table 5.2 summarizes the waveguide data for writing with perpendicular laser polarization; similar values of MFD were obtained but with 6-fold increase in propagation loss for the best waveguides. The propagation losses were adjusted for the small mode mismatch loss shown in Table 5.1 and Table 5.2. The difference between the MFD for vertical and horizontal polarized modes is below the 0.5 µm uncertainty of the measurements.

Table 5.1: Waveguide properties for various pulse energy exposure conditions for parallel polarization of the writing laser

Pulse Energy (nJ)	MFD (x, y) (µm)	Coupling loss (dB)	Propagation loss, α (dB · cm^{-1})
90	11.2, 11.7	0.04	1.4
130	9.0, 10.2	0.05	0.3
160	8.5, 10.2	0.09	0.6

Figure 5.2 shows the transmission spectra of two BGWs written with parallel (along y-axis) and perpendicular (along x-axis) polarization of the writing laser and spectrally probed with vertical (along z-axis) and horizontal (along x-axis) input polarized light.

Table 5.2: Waveguide properties for various pulse energy exposure conditions for perpendicular polarization of the writing laser

Pulse Energy (nJ)	MFD (x, y) (µm)	Coupling loss (dB)	Propagation loss, α (dB · cm^{-1})
90	Poor guiding	Poor guiding	Poor guiding
130	11.1, 11.8	0.04	2.4
160	12.1, 12.7	0.14	1.9

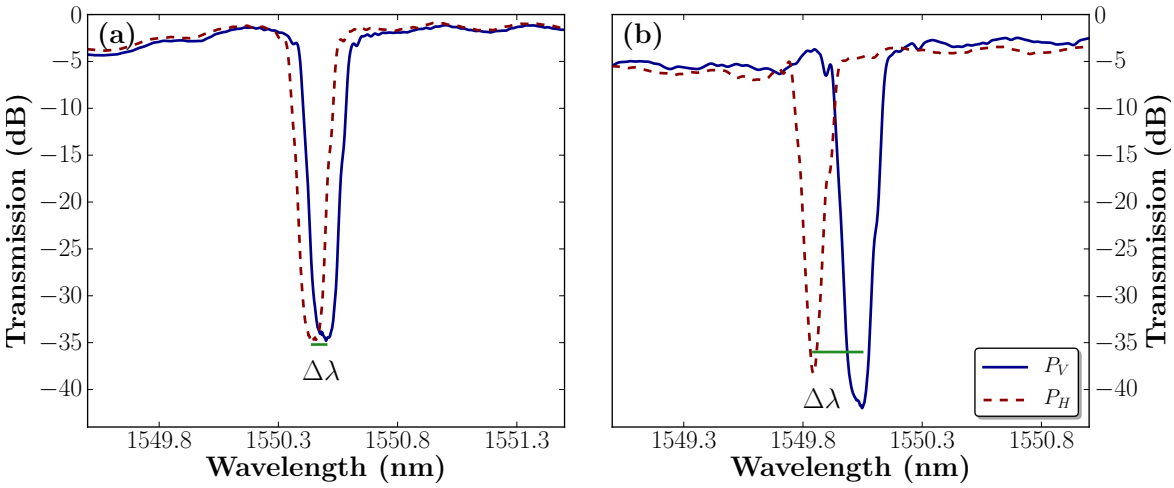

Figure 5.2: Transmission spectra of two BGWs written with parallel (a) and perpendicular (b) polarizations of the writing laser with 160 nJ pulse energy and probed with vertical polarized light (– blue solid line) and horizontal polarized light (- - red dashed line).

The birefringence present in the waveguides, Δn_{eff}, can be calculated directly from the spectral splitting, $\Delta\lambda$, from Equation 5.1. Birefringence values of $(4.7 \pm 0.5) \times 10^{-5}$ and $(1.7 \pm 0.1) \times 10^{-4}$ were found for the examples in Fig. 5.2 for parallel and perpendicular writing laser polarizations, respectively. The BGWs spectral response was relatively strong, introducing up to a 30% discrepancy between the birefringence values calculated with the BGW splitting method on segmented waveguides and the values determined with the crossed polarizers technique on continuous waveguides.

For the 1550 nm BGWs resonance, the perpendicular polarization of the writing laser induces a larger birefringence due to the strong form birefringence associated with this nanograting orientation, as well as a higher propagation loss, as can be seen by comparing Table 5.1 with Table 5.2.

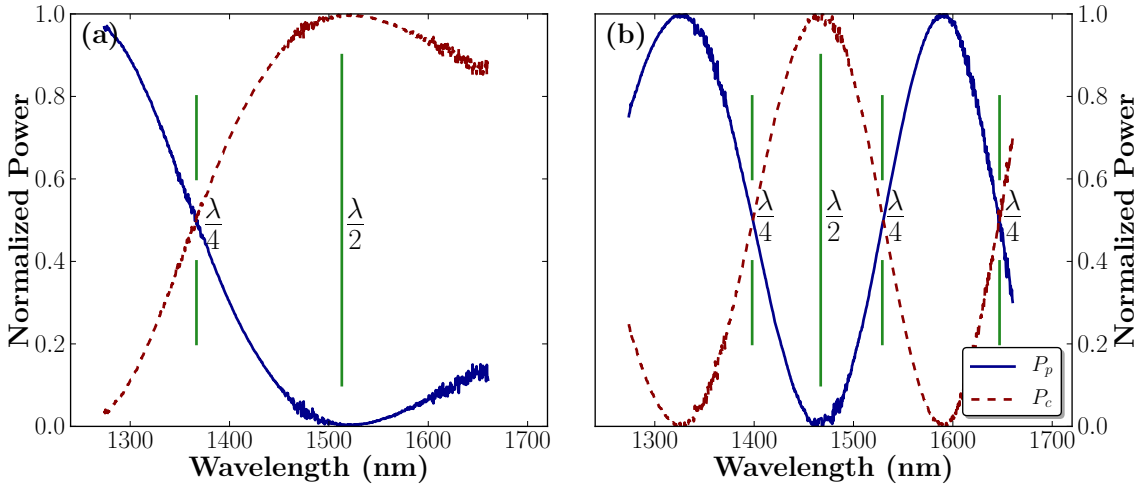

Figure 5.3: Normalized spectrum for P_p (– blue solid line) and P_c (- - red dashed line) for (a) parallel and (b) perpendicular polarizations of the writing laser with 160 nJ pulse energy and for 45° linearly polarized input light. The $\lambda/4$ and $\lambda/2$ markers indicate wavelengths where the waveguide behaves as quarter-wave and half-wave retarders.

Figure 5.3 shows the measured values of the normalized transmission for the parallel (P_p) and crossed (P_c) powers using a 45° linear polarized input. The values for the transmitted power, P_p and P_c, measured with the crossed polarizer technique and calculated using Equation 5.3 and Equation 5.4, respectively, are shown in Fig. 5.3 as a function of the wavelength. The waveguides operate as half-wave retarders, as indicated in the figure when the value of P_c is 1 and the value for P_p is 0 for linearly polarized input light along a 45° orientation in respect to the eigenaxes. The quarter-wave retardation conditions are also identified for the case when both P_p and P_c are equal (0.5 in Fig. 5.3). For parallel polarization writing (Fig. 5.3(a)) a half-wave retarder behavior is noted at 1513 nm and a quarter-wave retarder is noted at 1365 nm. Strong form birefringence in the perpendicular polarization case (Fig. 5.3(b)) yields a half-wave retarder at 1467 nm and three quarter-wave retarders at 1400 nm, 1530 nm, and 1646 nm.

Fig. 5.4 shows, as an example, the solutions of Equation 5.6 for the case of perpendicular writing polarization with 160 nJ of pulse energy and for m between 2 and 5. The red circles (●) represent the results obtained using four BGWs with different periodicity and indicate the correct choice for the birefringence from the crossed polarizers method, as highlighted by the broadened yellow line.

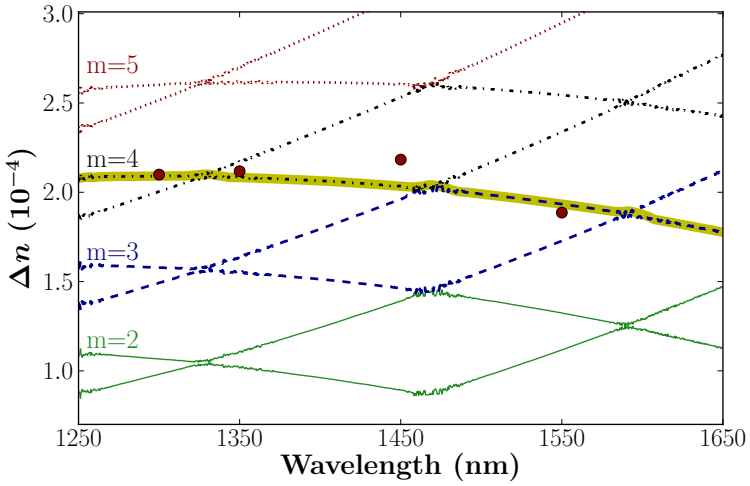

Figure 5.4: Results from the crossed polarizers method and from the Bragg grating waveguide shift method for a 25.4 mm long waveguide. The various lines represent the ambiguous birefringence values obtained from the crossed polarizers method, with values of m equal to 2, 3, 4, and 5. Each of these is split into two lines due to the $\pm$ sign ambiguity of the arccosine function. The red circles (●) represent the results obtained using four BGWs. The highlighted line is the correct birefringence result.

Birefringence values assessed from the Bragg grating polarization splitting are plotted across the 1300 nm to 1650 nm spectrum in Fig. 5.5(a) together with the birefringence values calculated from Equation 5.5 and Equation 5.6 from the data of the crossed polarizers technique in Fig. 5.3.

The phase ambiguity of Equation 5.5 was resolved definitively by adjusting the sign and order, m, for all wavelengths to match the calculated data with the Bragg grating data. The $\approx 1 \times 10^{-5}$ discrepancy between the data from the two methods, which is attributed to the physical difference of continuous versus segmented waveguides, is smaller than the phase adjustment (sign and order m) discrepancy of up to 5×10^{-5} in birefringence, thus providing non-ambiguous phase determination for the crossed polarizers data.

There is a significant difference in the birefringence values ranging from 1×10^{-5} to 5×10^{-5} for parallel writing, in contrast with values of 1.6×10^{-4} to 2.2×10^{-4} for perpendicular writing laser polarizations (160 nJ pulses at a constant scanning speed of 0.27 mm/s were used in both cases).

Figure 5.5(b) demonstrates the strong dependence of waveguide birefringence on the laser pulse energy for the parallel polarization exposure. The birefringence is higher (7×10^{-5}) at lower exposures (90 nJ and 110 nJ); however, the trend over a larger

spectrum suggests that the waveguide birefringence reaches a maximum at a specific wavelength that shifts towards lower values for decreasing laser pulse energies.

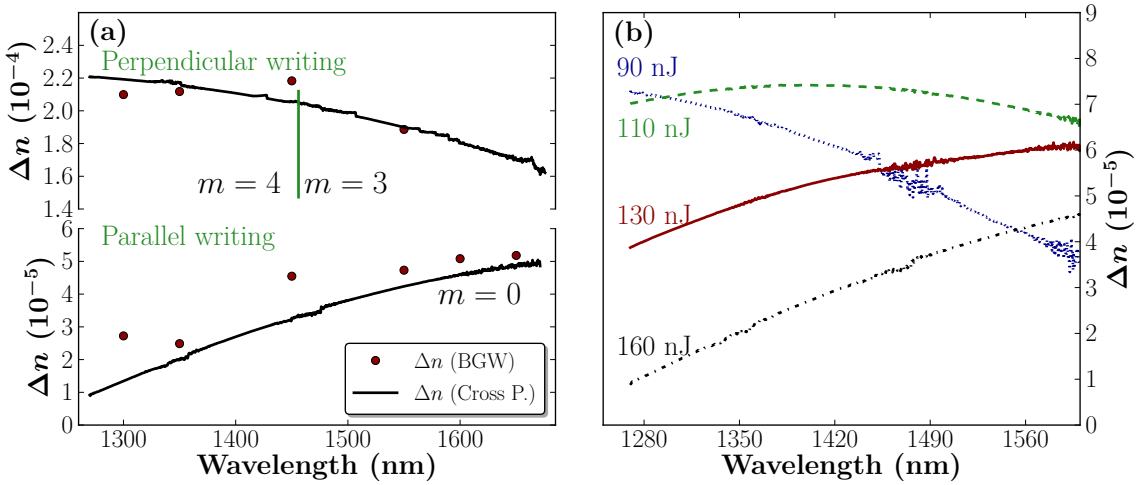

Figure 5.5: Birefringence as a function of the wavelength for (a) perpendicular and parallel polarizations of the writing laser with 160 nJ pulse energy and 0.27 mm/s scanning speed (averaged over 5 samples) and (b) various laser pulse energies for parallel polarized writing at 0.27 mm/s scanning speed.

The minimum length required for a quarter-wave or a half-wave retarder can be found from Equation 5.7, where $n_{\text{eff}}(\lambda)$ is the wavelength dependent birefringence shown in Fig. 5.5.

$$L_{\text{QWP}}(\lambda) = \frac{\lambda}{4\Delta n_{\text{eff}}(\lambda)}; \quad L_{\text{HWP}}(\lambda) = \frac{\lambda}{2\Delta n_{\text{eff}}(\lambda)} \tag{5.7}$$

Furthermore, the minimum length equations can also provide insight for the design of broadband wave plates. If the relative variation of birefringence is the same as the relative variation of wavelength (Equation 5.8), then there is a length, L, for which the retardance is constant and given by Equation 5.9, with WP representing the wave retarder type (WP = 1/2 for a half-wave and WP = 1/4 for a quarter-wave plate).

$$\frac{d\Delta n_{\text{eff}}}{\Delta n_{\text{eff}}} = \frac{d\lambda}{\lambda} \tag{5.8}$$

$$L = \text{WP}\frac{\lambda}{\Delta n_{\text{eff}}} \tag{5.9}$$

For waveguides fabricated with 110 nJ of pulse energy (Fig 5.5(b)), the condition of Equation 5.8 is met for a band between 1250 nm and 1315 nm, as shown in Fig 5.6. Across this band the length is constant and the retardance variation (phase variation) was measured to be better than ± 0.005 rad.

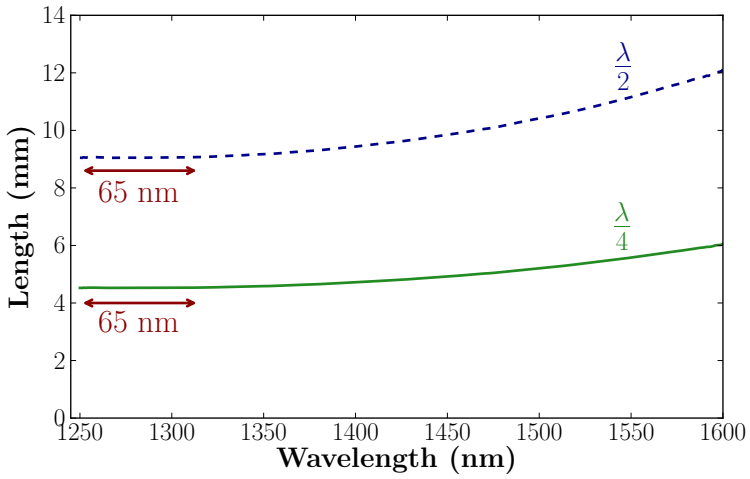

Figure 5.6: Waveguide length required for quarter-wave and half-wave retarders as a function of wavelength (written with 110 nJ pulse energy).

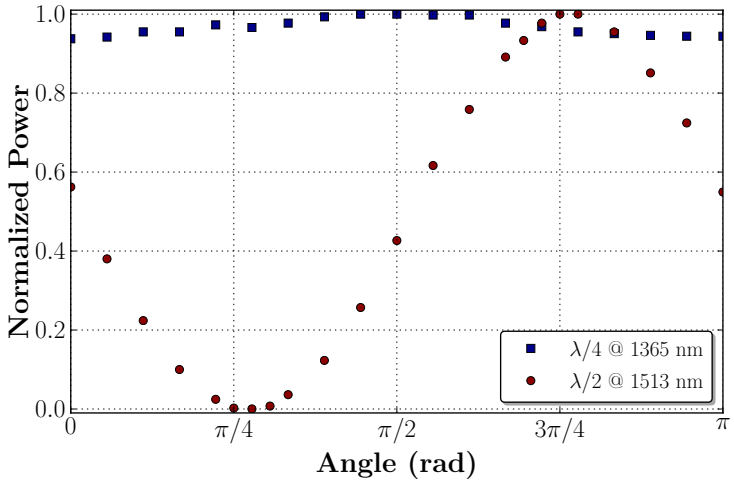

Figure 5.7: Polarization analyzer response of a quarter-wave (■ blue square) and a half-wave retarder (● red circle) response of a 25.4 cm long waveguide fabricated with parallel polarized 160 nJ pulses.

Using a 5 mW linearly polarized broadband source oriented at 45°, the waveguide characterized in Fig. 5.3(a) was analyzed with a linear polarizer as a function of angle

yielding the quarter-wave and the half-wave behavior plots at 1365 nm and 1513 nm, respectively, as shown in Fig. 5.7.

The 95% to 100% power variation at 1365 nm is very close to the ideal quarter-wave plate operation, while the output at 1513 nm shows the expected sinusoidal power variation with linear polarized light output at $3\pi/4$ angle having 35 dB contrast to the power measured with orthogonal polarization at $\pi/4$ angle.

5.2.4 Discussion

As shown in Fig. 5.5, the waveguide birefringence varies strongly with wavelength and this can favor the fabrication of broadband wave retarders. Such a device requires a linear increase in the birefringence (Δn_{eff}) with respect to the wavelength such that the retardance (δ) remains constant over a given band. This condition is available for the case of 110 nJ pulse energy in Fig. 5.5(b), where a half-wave plate can be implemented with a 9.06 mm long waveguide and a quarter-wave plate with a 4.53 mm long waveguide, with an expected 65 nm band centered at 1283 nm and within a phase variation of $\pm$ 0.005 rad. Further tuning of the exposure condition may allow us to broaden and extend such wave plates to other spectral windows. The wave plates were heated from 20 ℃ to 70 ℃ with no measurable change in birefringence. Therefore, the wave plates are stable for probe intensities low enough not to produce significant changes in temperature.

For the present 25.4 mm long waveguides, the wave retarders formed with parallel polarization of the writing laser were zero-order ($m = 0$ Fig. 5.7), while the retarders fabricated with perpendicular polarization of the writing laser were third-order and fourth-order wave plates. In the former case, the total insertion loss of the device was 1.5 dB, while in the latter case, a zero-order half-wave retarder would only require approximately a 4 mm long waveguide at 1550 nm wavelength, which would result in a much more favorable 0.8 dB insertion loss. Therefore, perpendicular polarization of the writing beam is preferred for making more compact and lower loss wave plates, but this advantage may be less favorable depending on the laser pulse energy (Fig. 5.5(b)) and the required MFD of the waveguide, which is also dependent on the laser pulse energy.

More generally, the data presented here demonstrate that quarter-wave and half-wave plate waveguides can be optimized for a given wavelength to offer low loss, mode

matching, and short device length. With femtosecond fabrication, it is possible to insert specific retardance on-the-fly at key positions in optical circuits, or produce low and high birefringence waveguides for arbitrary tuning of its polarization dependence characteristics.

5.3 Polarization beam splitters

Integrated beam splitters in fused silica and borosilicate glass substrates have been used to demonstrate the potential for femtosecond written optical components to measure entangled photons [122, 123] that may be essential in quantum computation and other application areas such as quantum key distribution [126] and differential polarization phase-shift keying for optical communication systems [125]. A key requirement for that objective is the development of highly stable polarization splitting optics that can be integrated into three dimensional optical circuits. This section describes how birefringent waveguides can be used to implement a polarization splitting directional coupler with spectral responses designed for wavelength division multiplexing (WDM) operation in the C and L telecom bands.

5.3.1 Theoretical analysis

A schematic of the directional couplers developed is shown in Fig. 5.8. The coupling ratio r of a directional coupler is defined in Equation 5.10, where P_1 and P_2 are the powers measured at the output ports (input arm and opposite arm, respectively).

$$r = \frac{P_2}{P_1 + P_2} \tag{5.10}$$

The coupling ratio follows the relation for symmetric coupling in Equation 5.11, where K is the coupling coefficient, ϕ is the phase accumulated in the bending regions of the directional coupler, and L is the length of the coupling region. K and ϕ are both wavelength and polarization dependent; therefore, r will also be dependent on the wavelength.

$$r = \sin^2(KL + \phi) \tag{5.11}$$

To develop a high extinction ratio polarization beam splitter, a large difference between the coupling ratios of the orthogonal polarization modes is required. This difference is given by a polarization splitting contrast factor, $\Delta r = |r_V - r_H|$. Using Equation 5.11, this contrast factor expands to:

$$\Delta r = |\sin[(K_V - K_H)L + \phi_V - \phi_H] \sin[(K_V + K_H)L + \phi_V + \phi_H]| \tag{5.12}$$

where r_V and r_H are the coupling ratios for vertical and horizontal polarized light, respectively. Suitable values for L and λ can be found to maximize the polarization splitting contrast factor in Equation 5.12 once appropriate values for the vertical polarization (K_V and ϕ_V) and horizontal polarization (K_H and ϕ_H) coupling coefficients have been engineered in the waveguide writing procedure.

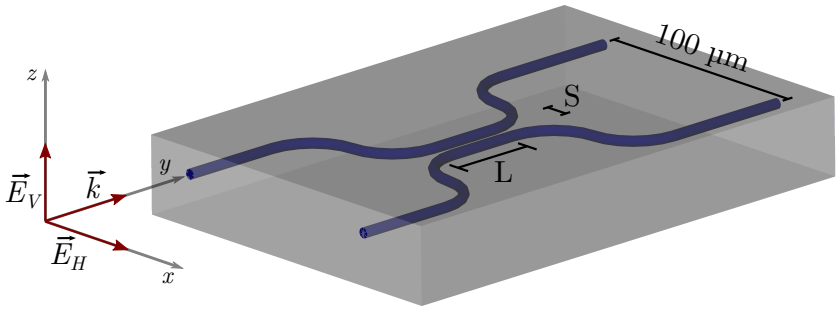

Figure 5.8: Schematic diagram of the polarization beam splitter. E_V and E_H indicate the electric field orientation of Vertical, V, and Horizontal, H, polarized light, respectively.

5.3.2 Fabrication

The femtosecond laser system used for the fabrication of the directional couplers was described in Section 2.1. The second harmonic beam at $\lambda = 522$ nm with a 300 fs pulse duration was focused into the fused silica glass to a 1.6 µm spot diameter ($1/e^2$ intensity) in a plane 75 µm below the surface with a 0.55 NA aspheric lens. Low loss optical waveguides were generated with a 150 nJ pulse energy while scanning the sample at a constant speed of 0.27 mm/s. The writing beam polarization state at the focus was linear and oriented to be parallel or perpendicular with respect to the scanning direction by using a half wave plate. These exposure conditions yielded a MFD of 9.6 µm x 9.0 µm for polarization parallel to the scanning direction, which closely matches the circular MFD of a single mode fiber (10.4 µm), yielding very low coupling loss (0.03 dB/facet) due to mode mismatch for fiber-to-facet coupling

when using index matching oil. The total insertion losses are therefore mostly due to waveguide propagation loss.

Following prior work in borosilicate glass [129], the directional couplers in fused silica were studied for a center-to-center waveguide separation distance, S, varied between 5 µm and 15 µm, and coupling length, L, varied between 0 mm and 20 mm. The waveguide S-bends were designed with a 100 mm radius of curvature that added negligible extra loss when compared to the loss of straight waveguides.

To accurately determine the birefringence in these waveguides, the Bragg grating shift technique described in Appendix A was used. Within each set of waveguides, a BGW was written with periodicity of 540 nm using an AOM operating at 500 Hz.

5.3.3 Characterization Methods

After fabrication, the coupling ratio of the directional couplers was characterized by using the free space end-fire coupling setup described in Section 2.2 and shown in Fig. 2.7. Light from a broadband unpolarized source (Agilent 83437A, 1250 nm to 1700 nm) was coupled into one waveguide arm of the coupler with an aspheric objective lens (New Focus, 30×, 0.4 NA). A broadband polarizer (Thorlabs LPNIR) was used in the free space region (between the source and the device) to excite vertically or horizontally polarized modes designated by V (along the z-axis) and H (along the x-axis), respectively, as shown in Fig. 5.8.

The powers at each output port (P_1 and P_2) were measured for both vertical and horizontal polarizations as functions of wavelength with an OSA (Ando 6317B) set to a resolution of 2 nm. The resulting power spectra were used in Equation 5.10 to calculate the coupling ratio as a function of the wavelength for each polarization. The intensity profile of the modes propagating in the waveguides at 1560 nm were measured as described in Section 2.3.

5.3.4 Results

Figure 5.9 shows the transmission spectra of two BGWs written with parallel (along y-axis) and perpendicular (along x-axis) polarization of the writing laser and spectrally probed with vertical (along z-axis) and horizontal (along x-axis) input polarized light. From the shift in the Bragg wavelength, the birefringence, Δn_{eff}, can be determined

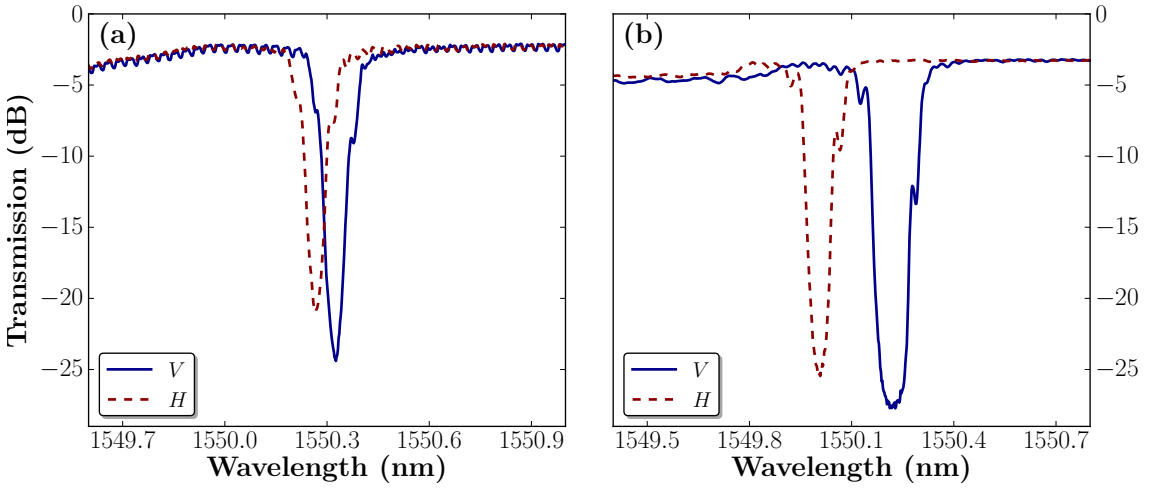

Figure 5.9: Transmission spectra of two BGWs written with parallel (along y-axis) polarization (left) and perpendicular (along x-axis) polarization (right). Vertical polarized (– blue solid line) and horizontal polarized (- - red dashed line).

from Equation 5.1, where $\Delta\lambda_B$ is the observed polarization shift in the Bragg wavelength and $\Lambda = 540$ nm is the grating period.

Birefringence values of $(5.2 \pm 0.5) \times 10^{-5}$ and $(2.1 \pm 0.1) \times 10^{-4}$ were found at 1550 nm wavelength for parallel and perpendicular writing polarizations, respectively, for the case of isolated waveguides. Higher birefringence could result for waveguides in the coupling region from the additional asymmetric stresses induced by a nearby parallel waveguide[2]. Birefringence values also vary (±30%) with the strength of the BGW and further depend on wavelength and on other exposure conditions such as energy per pulse. The higher birefringence associated with perpendicular writing also corresponds to a higher loss of 1.2 dB/cm. In the following work we have concentrated on the parallel polarization writing condition which produces lower propagation losses (0.7 dB/cm).

The measured coupling ratio of directional couplers fabricated with $S = 8\,\mu$m waveguide separation is shown in Fig. 5.10 as a function of interaction length. The data were fitted to Equation 5.11 for each wavelength using a Levenberg-Marquardt least squares algorithm to generate the coupling parameters K and ϕ that are shown as a function of the wavelength in Fig. 5.11 for both H and V polarizations. The average difference between the K values for the two polarizations indicates an approximately 5% polarization difference.

[2]The effect of the asymmetric stresses will be studied in Section 5.4.

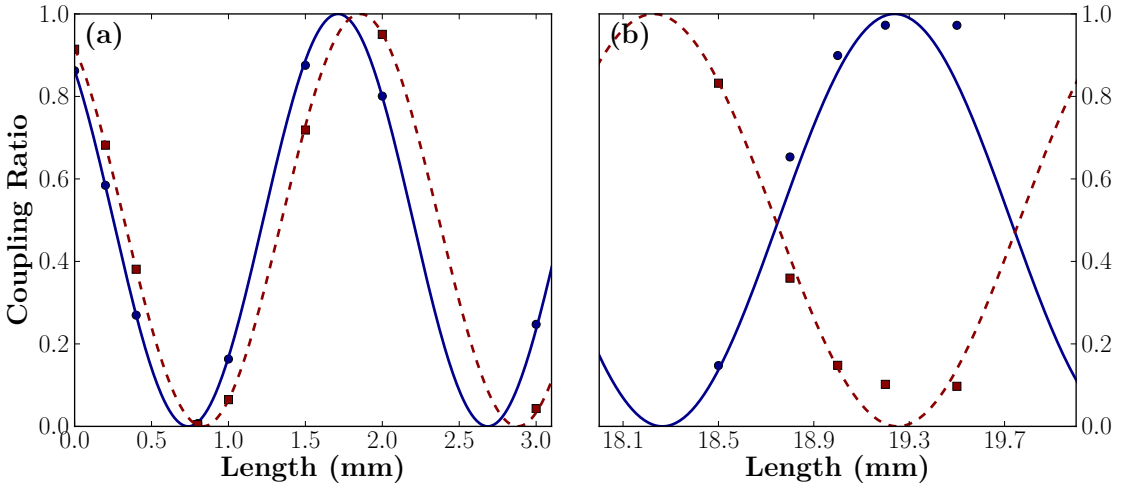

Figure 5.10: Measured coupling ratio, r, as a function of coupling length for vertical polarized (● blue circle) and horizontal polarized (■ red square) modes together with calculated fits (solid and dashed lines).

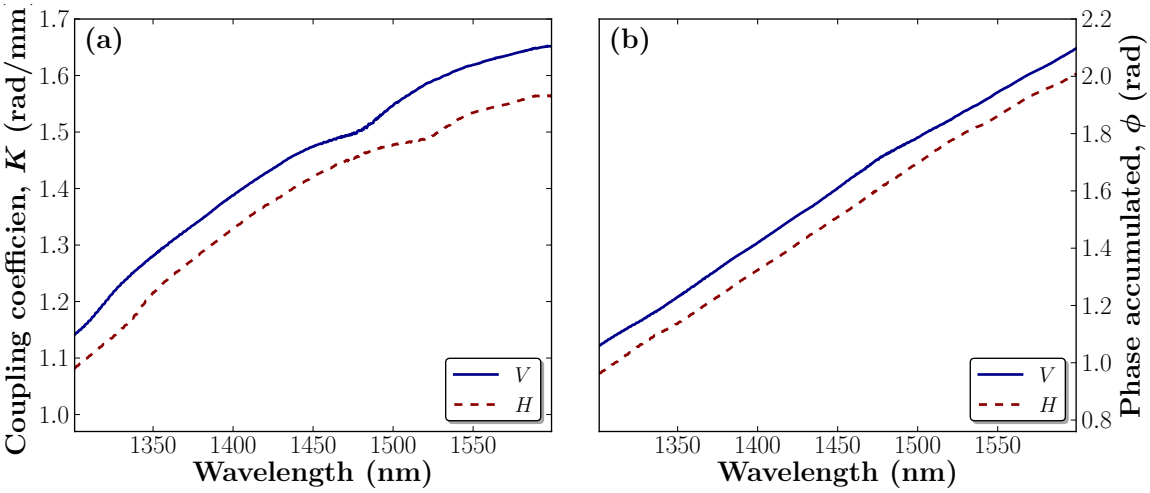

Figure 5.11: Calculated K and ϕ as a function of wavelength for vertical polarized (– blue solid line) and horizontal polarized (- - red dashed line) modes and $S = 8\,\mu\text{m}$ waveguide separation.

The experimentally determined values of K and ϕ were used to calculate the polarization splitting contrast factor (Equation 5.12) as a function of the interaction length and wavelength for each waveguide separation tested. The values of Δr are shown in Fig. 5.12 for two sets of couplers with waveguide separations of 5 µm and 8 µm. For 15 µm waveguide separation, weak coupling would have required excessively long coupling lengths to achieve polarization splitting.

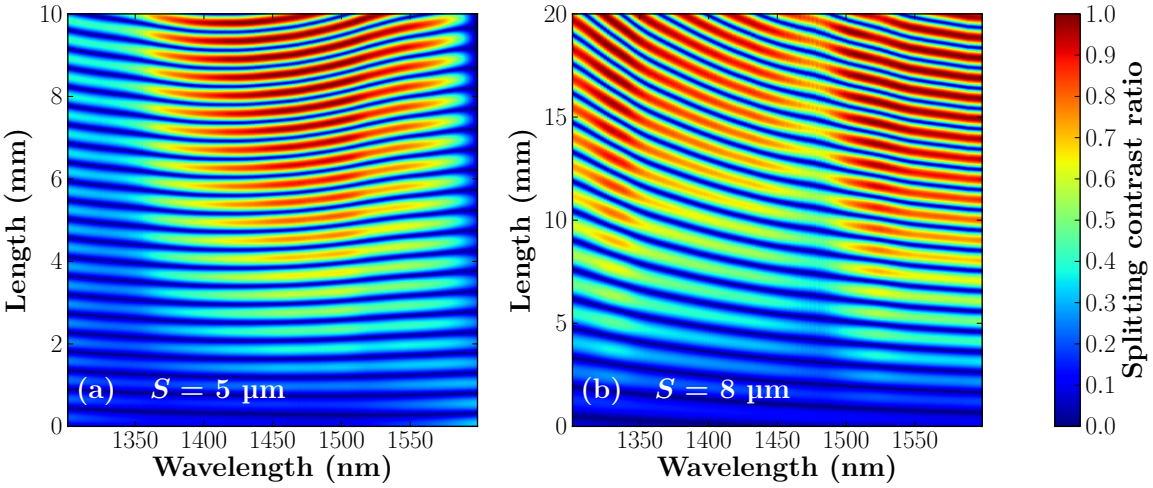

Figure 5.12: Splitting contrast factor, Δr, for directional couplers with 5 µm waveguide separation (a) and 8 µm waveguide separation (b).

By analyzing Fig. 5.12, it is possible to find values for the coupling length that offer very high polarization splitting contrast factor, Δr, greater than 95% for several wavelengths. For a coupler with 5 µm waveguide separation and longer than 7 mm interaction length, it is possible to find relatively strong polarization splitting for specific wavelengths in the range of 1400 nm to 1550 nm. For 8 µm waveguide separation, an interaction length of more than 12 mm is necessary to find strong polarization spitting at select wavelengths between 1300 nm and 1600 nm. However, because the 'fringes' in Fig. 5.12 are not perfectly horizontal, the polarization splitting occurs in a narrow bandwidth. For example, a polarization extinction ratio greater than 15 dB is available across an ≈10 nm bandwidth at 1478 nm with a polarization splitter of 5 µm separation and 9.5 mm interaction length, or at 1505 nm for a directional coupler of 8 µm separation and a 19 mm interaction length.

As a practical demonstration, Fig. 5.13 shows a plot of the power measured at both P_1 and P_2 output ports as a function of the input polarization angle, for a wavelength of 1484.00 nm ± 0.05 nm in a device with a coupling length of 19.2 mm and a coupler center-to-center separation of 8 µm. Aligned with the polarization angle, one also sees images of the output beam profile at both ports (P_1 and P_2) oscillating with this angle and yielding maximum polarization contrast at the $\frac{\pi}{2}$ radian and π radian positions, for horizontally and vertically polarized light, respectively.

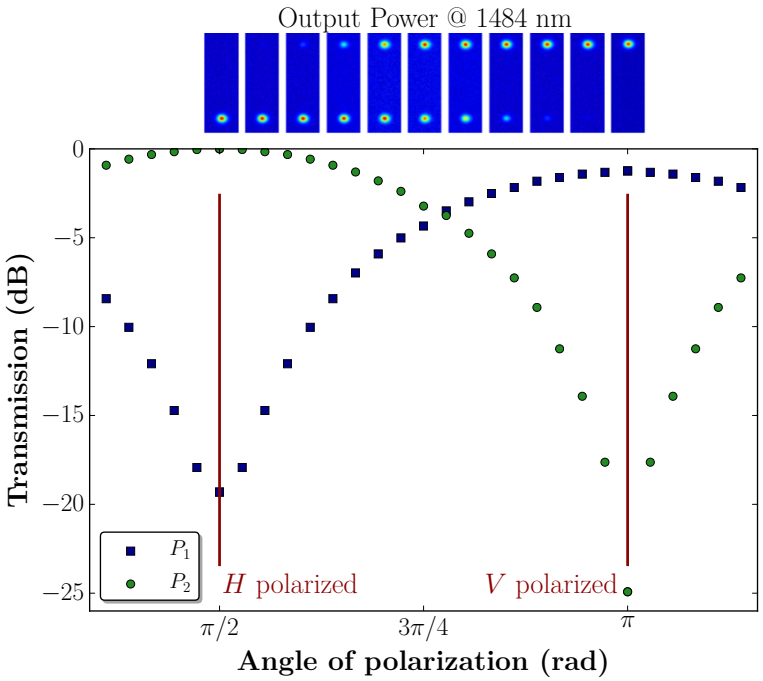

Figure 5.13: Output power and mode profile as a function of the angle of polarization at 1484 nm, for the same arm as the input (P_1, ■ blue square) and for the opposite arm (P_2, ● green circle).

5.3.5 Discussion

Figure. 5.14 shows a rendering of a directional coupler with the input light controlled by a polarizer, to work as a polarization beam slitter.

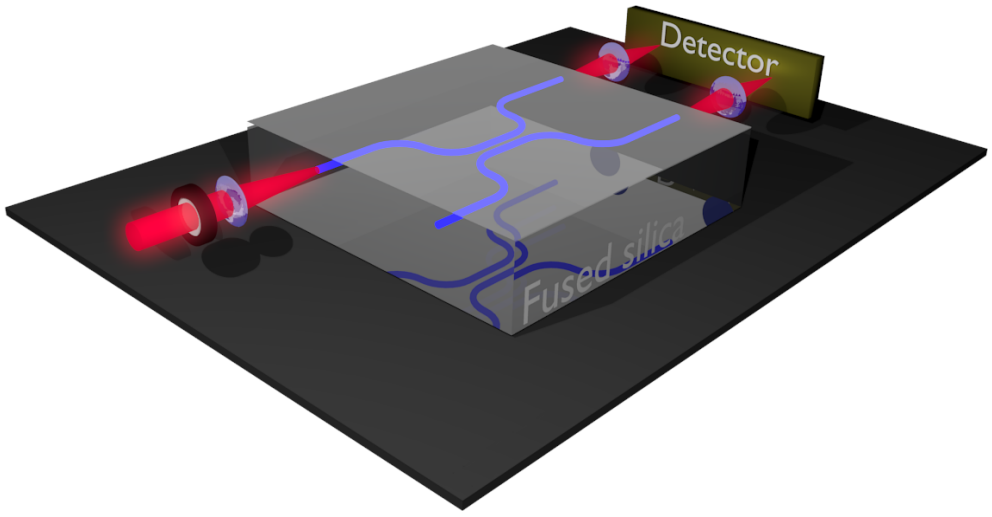

Figure 5.14: 3D rendering of a directional coupler used as polarization beam splitter.

For a coupler device with a center-to-center separation of 8 µm and an interaction length of 19.2 mm, the results in Fig. 5.13 show that moderately high extinction ratios of -19 dB and -24 dB are possible for the H and V polarizations, respectively. The analysis of the coupling ratio data shown in Fig. 5.12 further permits one to find multiple combinations of wavelengths and coupler lengths for a given waveguide separation that offer high polarization extinction ratios in narrow spectral bands. Furthermore, extending these splitters to other waveguide separations offers additional degrees of freedom for controlling K and ϕ spectral values for obtaining wide spectral coverage across the full telecom band tested here. One can further optimize the bending radius of the directional couplers in the same way as performed in today's planar light circuits in order to produce polarization beam splitters with even wider broadband response. Extending the bandwidth of the present polarization beam splitters may also be possible with this femtosecond laser writing technique by following the same design principles described in [129, 130].

The present polarization splitting coupler was based on the lower birefringence waveguides ($\Delta n_{\text{eff}} = 5.2 \times 10^{-5}$ for parallel polarization writing) that offered the lowest propagation loss of 0.7 dB/cm (with Bragg grating) or 0.5 dB/cm (without Bragg grating). The strong polarization extinction of 19 dB to 24 dB seen here, together with the 10 nm bandwidth for $\approx$ 15 dB polarization contrast, are comparable to the results reported for polarization splitting in PCF optical fiber [131] or in planar lightwave circuits [132]. However, the present laser writing approach required long coupling lengths of up to 20 mm to enable complete separation of the polarization modes. An alternative approach that exploits the 4-fold higher form birefringence in waveguides fabricated with perpendicularly polarized laser light promises more compact polarization beam splitters. Here, a shorter waveguide length may compensate for the additional propagation loss found for such highly birefringent waveguides (i.e., 0.5 dB/cm additional loss in BGWs fabricated with perpendicular versus parallel laser writing polarization) that may be developed by the same design and analysis methods presented in this section.

Developing new laser processes that can lower birefringence in the present waveguides would, on the other hand, enable the fabrication of polarization insensitive waveguides which may allow the single step fabrication of both polarization free and polarization dependent devices for highly functional integration onto the same circuit platform. It may be possible that higher repetition rates can be used with femtosecond laser writing in fused silica to drive heat accumulation effects similar to the ones observed

in borosilicate glass to reduce waveguide birefringence [23]. Despite the 5.2×10^{-5} birefringence observed in the present fused silica waveguides, polarization independent beam splitters can also be developed by using very short or zero-length directional couplers as demonstrated in [123]. Lastly, tuning the radius of the S-bend waveguide region offers further latitude in shaping the spectral response of both the high and low polarization splitting waveguide couplers for specific application requirements.

5.4 Stress induced birefringence tuning

Femtosecond laser exposure produces form and stress birefringence in glasses, mainly controlled by laser polarization and pulse energy, which leads to challenges in certain applications where polarization mode dispersion or polarization splitting is critical for the desired performance of optical devices. In this section, laser modification tracks with different positioning near the waveguides vicinity were applied to preferentially stress the laser-written waveguides and explore the possibility of tuning the waveguide birefringence in devices fabricated in bulk fused silica glass by femtosecond laser exposure. Polarization splitting in BGWs showed that the laser modification tracks controllably add or subtract stress to the pre-existing waveguide birefringence, demonstrating independence from the nanograting induced form birefringence and the contributions from material stress. Stressing regions offer tunable birefringence from $\sim$0 up to 4.35×10^{-4}, possibly enabling great flexibility in designing polarization dependent devices, as well as making polarization insensitive devices.

5.4.1 Background

As seen in Section 5.2 and Section 5.3, the two major sources of birefringence in waveguides fabricated by femtosecond laser exposure are anisotropic material stress and form birefringence. Laser written waveguides in glasses [133] and crystals [134, 135] have shown various degrees of birefringence due to the asymmetry of the non-linear laser-material interactions in the focal volume of the femtosecond laser that cause material stress [42, 110], as well as much stronger form birefringence due to laser-induced nanograting structures [113, 120]. The alignment of nanogratings with the waveguide propagation vector, which is controlled by the laser polarization direction with respect to the writing direction, offers a strong influence over the waveguide

birefringence. Heat accumulation in borosilicate glass [23] has shown to produce lower birefringence due to radial stress regions as opposed to the more asymmetric stress produced in fused silica [136, 137]; however, these features remain unexplored in most glasses.

The femtosecond fabrication technique is very attractive for single step fabrication of three-dimensional integrated optical circuits [4]; however, the birefringence inherent to this process in fused silica may be detrimental for certain applications, such as integrated quantum entanglement experiments [122, 123] or traditional optical communication systems where a low birefringence is desired to reduce polarization mode dispersion. Birefringence remains an important property to control in order to address these issues. For example, in [123] researchers demonstrated the use of borosilicate glass waveguides, with reported low intrinsic birefringence of 7×10^{-5}, to reduce polarization dependency of directional couplers. However, the higher birefringence observed for ultrafast laser-written waveguides fabricated in fused silica limits their application in two-photon quantum walk experiments due to polarization dependent coupling [138]. Another aspect of ultrafast laser-written waveguides that has been identified as a challenge towards integrated optical circuits for quantum experiments is the ellipticity of the waveguide modes, even despite the low birefringence provided by materials other than fused silica [139].

While a diminished birefringence has been a major objective to meet the need for polarization insensitive devices, many other applications require a strong polarization dependence, including those in quantum optics [121, 127]. For this and other purposes, prior work on polarization beam splitters [140] and zero-order wave retarders [141] have already harnessed the weak birefringence properties of ultrafast fabricated optical waveguides in fused silica, and would benefit from means to increase their birefringence.

In silicon-on-insulator platforms, the application of stress to modify the properties of waveguides has been used [142] and found to reduce birefringence values from $\sim 10^{-3}$ to $\sim 10^{-5}$, as demonstrated in ridge waveguides [143]. In this work, the possibility of tuning the waveguide birefringence in fused silica was explored by inducing stress with femtosecond laser fabricated modification tracks formed parallel to the waveguides. Exploiting this stress, together with the form birefringence generated by the laser-formed nanogratings, allowed the prospects of either increasing or decreasing the waveguide birefringence. This induced stress technique also provides a way of tuning the waveguide mode ellipticity, thereby improving the symmetry for directional coupler designs. The flexibility provided by this method adds another degree of freedom in

the design of integrated optical devices, serving as a facile method for tailoring strong and perhaps also zero birefringence devices, that can be strategically positioned in a three dimensional optical circuit for even broader applications.

5.4.2 Device fabrication

Waveguides with stress inducing laser modified tracks were written with the femtosecond laser system described in Section 2.1 ($\lambda = 522$ nm with 300 fs pulses at 500 kHz with $M^2 = 1.35$). The laser was focused to a 1.6 µm diameter spot ($1/e^2$ intensity) with a 0.55 NA aspheric lens (New Focus, 40×), 75 µm below the surface of 1 mm thick fused silica glass (Corning 7980 with all sides optically polished). The sample was scanned along either of the 25.4 mm or 12.7 mm lengths to define the waveguides.

Laser exposures of 150 nJ pulse energy and 0.268 mm/s scanning speed were selected [8] to offer moderately low propagation loss and a MFD comparable with that of SMFs for low fiber to waveguide coupling loss. Laser modification tracks that induced varying degrees of stress were fabricated with identical waveguide writing conditions but with pulse energies varied from 100 nJ to 250 nJ to study their effect on the waveguide propagation constant and birefringence. Because the laser modified tracks also served as waveguides, different laser exposure energies were necessary to guarantee propagation constant mismatch with the center waveguide and to inhibit evanescent coupling. In this way, the stress tracks could be positioned as close as 10 µm from the waveguide before coupling or multi-mode guiding effects were discernible.

An AOM was used to modulate the laser to form burst trains that produce the BGWs that work as waveguides under test, as described in Chapter 4. A modulation frequency of 500 Hz, together with a 0.268 mm/s scan speed, yielded a grating period of 536 nm for a 1550 nm Bragg resonance wavelength. Again, the characterization methods described in Appendix A were used to measure the polarization splitting of BGWs spectral responses to provide an unambiguous measurement of the waveguide birefringence and effective index [84, 144].

Two orthogonal stress tracks orientations were tested, to examine horizontal and vertical stress symmetries acting against the center optical waveguide, as indicated in Fig. 5.15. The asymmetric cross-sectional structure (3 µm wide × 16 µm high) formed by the present lens is expected to yield significantly different degrees of birefringence for these horizontal (Fig. 5.15 right inset) and vertical (Fig. 5.15 left inset) configurations.

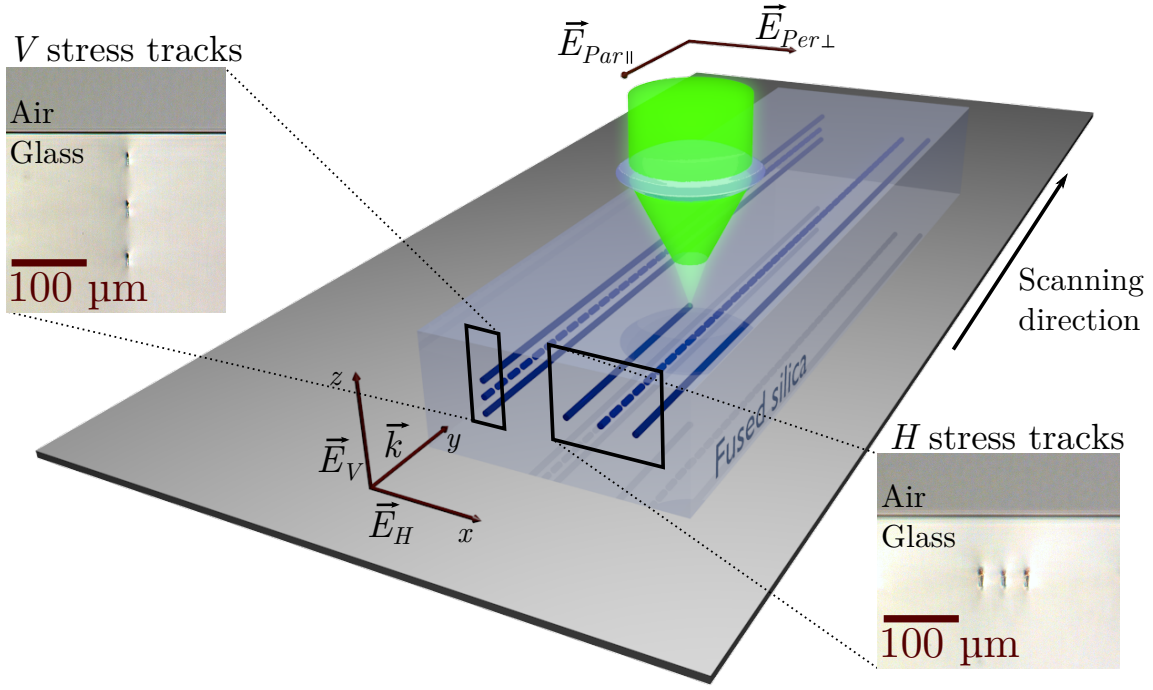

Figure 5.15: Schematic arrangement for birefringence control where $\vec{E}_V$ and $\vec{E}_H$ indicate the electric field orientation for Vertical, V, and Horizontal, H, waveguide polarization eigenmodes, while $\vec{E}_{Par\parallel}$ and $\vec{E}_{Per\perp}$ represent the parallel and perpendicular polarizations of the writing laser, respectively. The insets show microscope end view images of the Bragg grating waveguides, sandwiched between vertical (left) and horizontal (right) stress tracks.

The insets also show the position of the waveguide and the stress tracks relative to the glass surface. The separation of stress tracks from the waveguide was varied from 4 µm to 70 µm, measured from center to center. For the vertical geometry, the bottom track was written first, followed by the BGW and then the top track, in order to avoid laser beam propagation through a modified structure before reaching its focus. All tracks were written using the same scanning direction to avoid the non-reciprocal "quill" effects [43, 145]. Finally, to orient the nanograting planes either parallel or perpendicular to the waveguide direction, the writing laser polarization was aligned perpendicular (along the x-axis), $\vec{E}_{Per\perp}$, or parallel (along the y-axis), $\vec{E}_{Par\parallel}$, respectively, by using a half-wave plate.

5.4.3 Characterization Methods

The waveguide eigenmodes in the BGWs were designated as vertical, V (along the z-axis, slow axis, corresponding to the TM mode) and horizontal, H (along the x-axis,

fast axis, corresponding to the TE mode). The axis orientation and modes designation in respect to the rest of the experimental setup is also shown in Fig. 5.15.

The devices with different stress geometries were characterized according to morphology (to visually connect the guiding zones with the observable stress fields in the material), MFDs and losses (to assess the effects of the stress tracks on the scattering losses and on the waveguide modes), birefringence and mode effective index (to determine the influence of material stress on the total waveguide birefringence and also to determine which polarization modes are most affected).

5.4.4 Morphology

The morphology of the stress-modified waveguides was assessed through optical microscopy, resulting in the images shown in Fig. 5.16 for horizontal and vertical "stressing" geometries. The figures show stress tracks fabricated with 200 nJ pulse energy, parallel polarization of the writing laser, and 30 µm and 40 µm center-to-center separation, respectively, for the horizontal and vertical geometries.

In the images shown in Figs. 5.16(a) and 5.16(d), a strong white region in the center is visible, suggesting the presence of a positive refractive index difference with respect to the unmodified glass. The mode profile inset shown above Fig. 5.16(d) is observed to propagate along these higher refractive index regions. Birefringence can be observed around the laser modified tracks, as seen in Figs. 5.16(b), 5.16(c), 5.16(e), and 5.16(f), which were obtained by placing the same devices between two crossed polarizers, with their orientations represented by the green crosses in the picture. While the underlying stress appears small with the polarizers in vertical and horizontal orientations in Figs. 5.16(b) and 5.16(e), a strong stress region in the horizontal direction is visible in Figs. 5.16(c) and 5.16(f). These results indicate a preferential orientation in the asymmetric horizontal stress generated by the femtosecond laser exposure and suggests that the horizontal stress geometry might produce a stronger effect in the waveguide birefringence than the vertical alignment of the stress tracks with the BGWs. These stress regions also suggest a localized densification of the material which has been found to be partially responsible for the refractive index change [133]. Similar stress affected areas have been found in crystals [135] with densified waveguiding regions formed outside the modification track also by femtosecond laser exposure, which produces stress induced waveguiding as opposed to our work where the stress is used to modify the properties of the laser written waveguides.

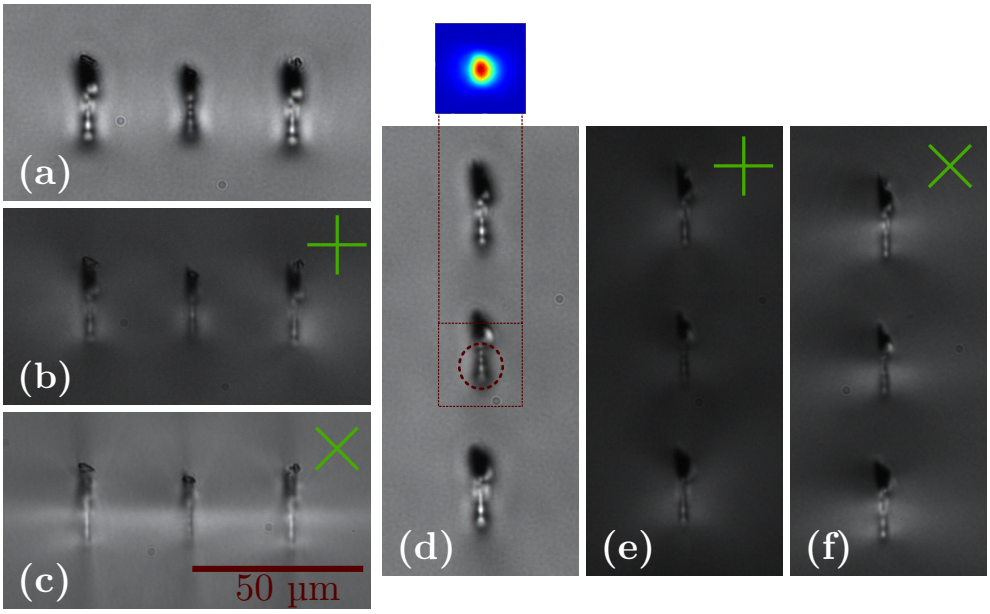

Figure 5.16: Optical microscope images of the end facets of the waveguides with the horizontal stress geometry (a, b, c) and the vertical stress geometry (d, e, f).
(a, d) Unpolarized picture with illumination adjusted to observe the waveguide regions. (b, e) Images with two crossed polarizers parallel and perpendicular to the glass surface. (c, f) Images with two crossed polarizers both at 45° angle to the glass surface. In all the crossed polarizers pictures the green cross indicates the orientation of the polarizers. A mode profile is also shown with its position indicated relative to the waveguide structure.

5.4.5 Mode size and losses

The intensity mode profiles were recorded with 1560 nm light coupled from a tunable laser (Photonetics Tunics-BT) into the various waveguides and the output imaged onto a CCD camera (Spiricon SP-1550M) through a 60× magnification lens. There was no measurable difference between the modes recorded with different polarizations of the input light.

The MFD measured for the reference BGW, without stress tracks and written with parallel polarized light ($\vec{E}_{Par\|}$), has a value of (9.8 µm × 11.2 µm) ± 0.2 µm, while horizontal stress tracks fabricated with 200 nJ of pulse energy and separated by 15 µm yields a MFD of (9.9 µm × 11.2 µm) ± 0.2 µm. The modes recorded for the perpendicular polarization of the writing laser generally followed the same trend although here, because the mode sizes are larger, the presence of the stress tracks slightly reduced the MFD.

Table 5.3: MFDs, for reference waveguides, BGWs, and examples with different stress track geometries.

Device	MFD ($x \times z$) µm ± 0.2 µm	
	Parallel $\vec{E}_{Par\parallel}$	Perpendicular $\vec{E}_{Per\perp}$
Uniform waveguide	9.5×11.0	11.3×11.3
Isolated BGW	9.8×11.2	12.7×12.2
H-Stress(15 µm; E = 200 nJ)	9.9×11.2	11.4×11.4
V-Stress(30 µm; E = 200 nJ)	10.0×11.4	11.9×11.3
V-Stress(20 µm; E = 250 nJ)	12.1×10.8	–

There is no noteworthy variation of the mode size when either horizontal of vertical stress tracks are present, with the exception of a larger mode size of (12.1 µm × 10.8 µm) ± 0.2 µm that was found using parallel polarization of the writing laser, with vertical stress geometry, written with 250 nJ of pulse energy and with a separation of 20 µm. These examples of recorded mode profiles are shown as inset images in Fig. 5.18 and Fig. 5.19, with laser exposure conditions defined therein. A non-BGW waveguide, fabricated without AOM modulation and with parallel polarization of the writing laser, has a slightly smaller (9.5 µm × 11.0 µm) ± 0.2 µm MFD. The differences between unmodulated waveguides and BGWs, in terms of birefringence, losses and MFDs, have been presented previously [140, 141]; however, the trends and the magnitude of the changes recorded here have also been shown to hold true for both waveguide devices. The MFDs of BGWs for different stress tracks geometry, writing conditions and polarization of the writing laser are summarized in Table 5.3.

The measured MFDs were used together with the 10.4 µm×10.4 µm MFD expected for a SMF at 1550 nm to estimate a coupling loss of (0.02±0.02) dB/facet for all the waveguides written with parallel polarization of the writing laser, while a (0.05±0.03) dB/-facet loss was found for the higher energy case mentioned above. For the perpendicular writing polarization ($\vec{E}_{Per\perp}$) the coupling losses varied from (0.03±0.02) dB/facet for a uniform waveguide to (0.14±0.04) dB/facet for the isolated BGW. The modal mismatch losses were used to offset the insertion loss data to determine the waveguide propagation loss.

Propagation losses in the waveguide fabricated with the perpendicular writing polarization were higher than the losses obtained by having the fabrication laser polarized parallel to the waveguide direction. Using the $\vec{E}_{Per\perp}$ polarization yielded

(1.1±0.1) dB/cm loss for BGWs and (0.9±0.1) dB/cm for unmodulated waveguides, while the $\vec{E}_{Par\|}$ polarization produced unmodulated waveguides with (0.5±0.1) dB/cm loss and BGWs with (0.8±0.1) dB/cm loss. Although the device made with vertical tracks at 250 nJ pulse energy and with a separation of 20 µm had a MFD compatible with the other waveguides, this fabrication condition was very close to a condition of significant coupling, which resulted in propagation losses of (1.4±0.1) dB/cm. All losses were measured at 1560 nm wavelength with the tunable laser source and with oil matched fiber coupling on both ends.

5.4.6 Birefringence and effective indices

The waveguide birefringence, was calculated from the Bragg wavelength splitting between two polarization eigenmodes, as described in Appendix A, using Equation A.1.

Based on the characterization system described in Section 2.2, the Bragg resonances were recorded with a light source (Thorlabs ASE-FL7002, 1520 nm to 1620 nm) and end-fire coupled into the BGWs while an oil matched fiber collected the output into an OSA (Ando 6317B) with a resolution of 0.01 nm. The input polarization of the free space propagating light was aligned to the V or H axis by rotating a broadband polarizer (Thorlabs LPNIR).

For reference, the Bragg resonant reflection spectra for waveguides written with parallel and perpendicular laser polarizations, are given in Fig. 5.17(a) and Fig. 5.17(b), respectively. The results show a 70.6 pm and a 201.4 pm wavelength split between the polarization eigenmodes from which birefringence values of $(6.6 \pm 0.4) \times 10^{-5}$ and $(1.88 \pm 0.04) \times 10^{-4}$, respectively, were inferred at 1550 nm. These values have proven to be repeatable within the reported $\pm 0.4 \times 10^{-5}$ uncertainty.

Figure 5.17(c) demonstrates a BGW with two horizontal stress tracks fabricated with 250 nJ pulses and a separation of 20 µm, yielding a birefringence of $(2.05 \pm 0.04) \times 10^{-4}$, a 3-fold increase versus the reference value shown in Fig. 5.17(a). A value of $(4.13 \pm 0.04) \times 10^{-4}$ from a 443.2 pm wavelength split was calculated from Fig. 5.17(d) for a BGW fabricated with perpendicular polarization and stress tracks made with 200 nJ pulses and separated by 13 µm.

Figure 5.18 and Fig. 5.19 show the measured birefringence as a function of the stress inducing tracks separation from the center BGWs, together with the result plotted at ∞ separation (without stress tracks), which represents the relevant reference BGW

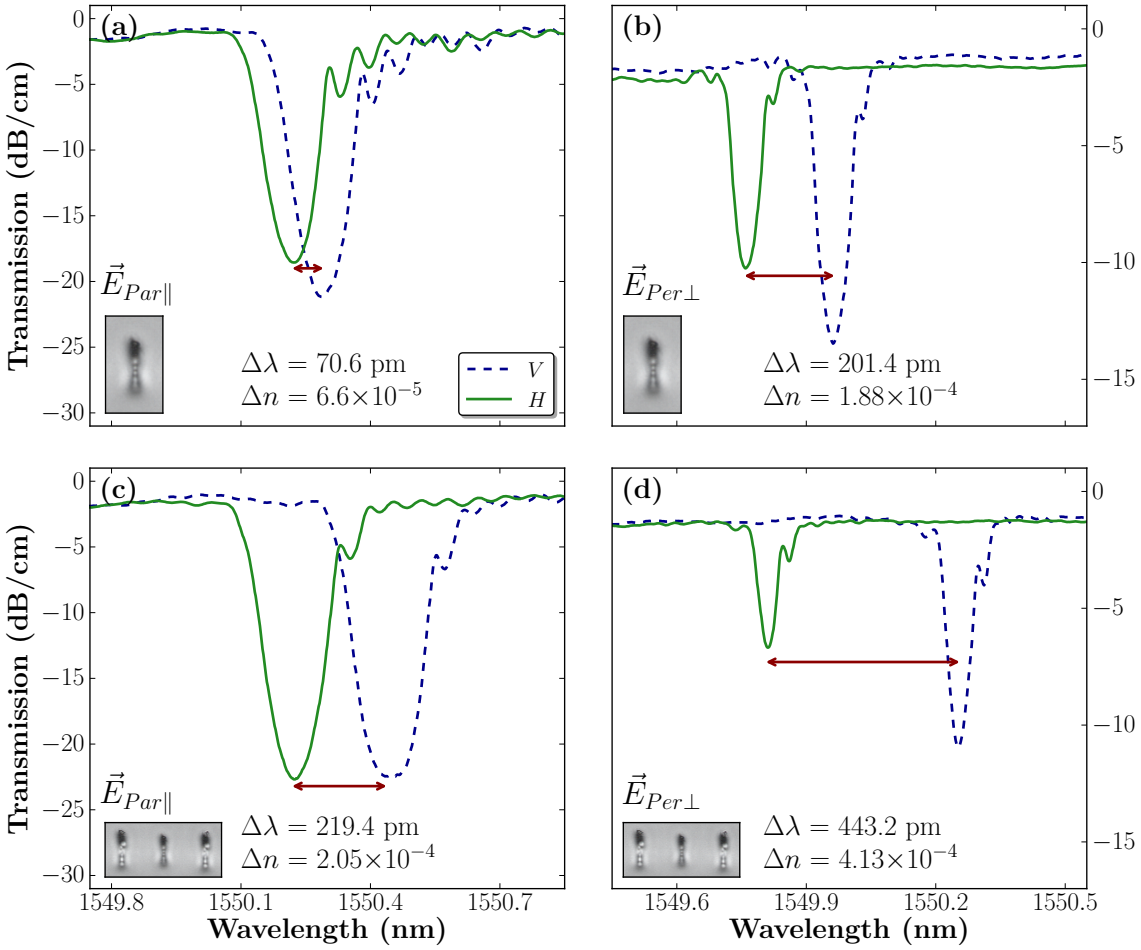

Figure 5.17: V and H polarized transmission spectra for BGWs fabricated with 150 nJ of pulse energy and written with parallel (a, c) and perpendicular (b, d) polarizations of the writing laser (a) Reference BGW, with parallel polarization writing. (b) Reference BGW, with perpendicular polarization writing. (c) BGW stressed by two 250 nJ tracks in the horizontal configuration with 20 µm separation. (d) BGW stressed by two 200 nJ tracks in the horizontal configuration with 13 µm separation.

birefringence for each fabrication condition. Figure 5.18 clearly shows that the stress tracks written closer to the BGW produced a stronger effect in the birefringence. The horizontal geometry approach in Fig. 5.18(a) demonstrates the possibility to obtain a birefringence of $\Delta n = 2.52 \times 10^{-4}$, up to a 4-fold increase when compared with the 6.6×10^{-5} present in the reference waveguide. Here, stress tracks with the highest tested pulse energy (250 nJ) and a narrow separation of 15 µm from the BGW were applied. Figure 5.18(b) shows the possibility of decreasing the birefringence by using the vertical geometry approach. In this case, it was possible to reduce the birefringence to a value as low as 1.5×10^{-5} by using stress tracks written with 200 nJ pulses and separated

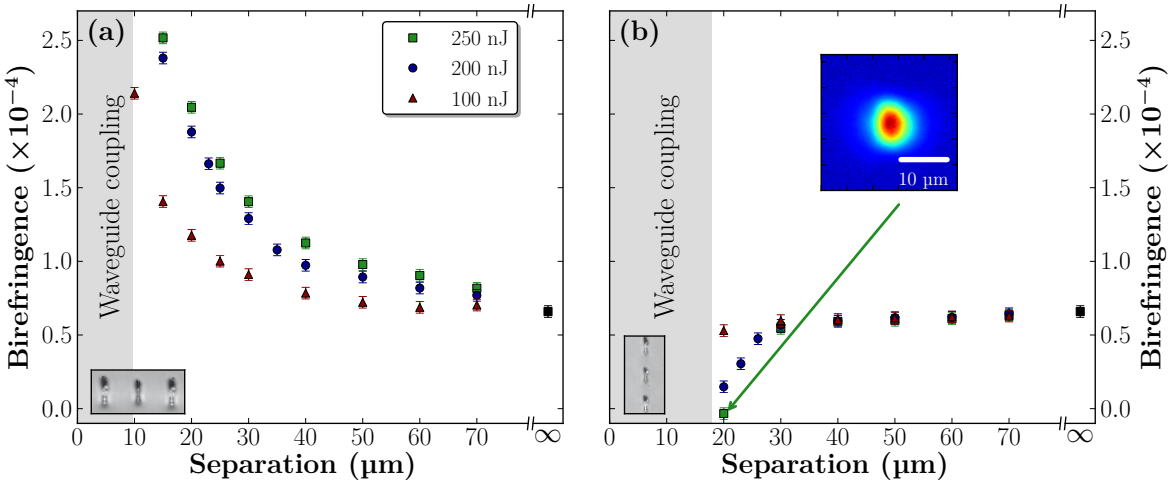

Figure 5.18: Birefringence as a function of the stress tracks separation for (a) horizontal geometry and (b) vertical geometry, and various applied laser energies. The black squares at ∞ separation represent the reference birefringence measured for a single BGW without stress modification.

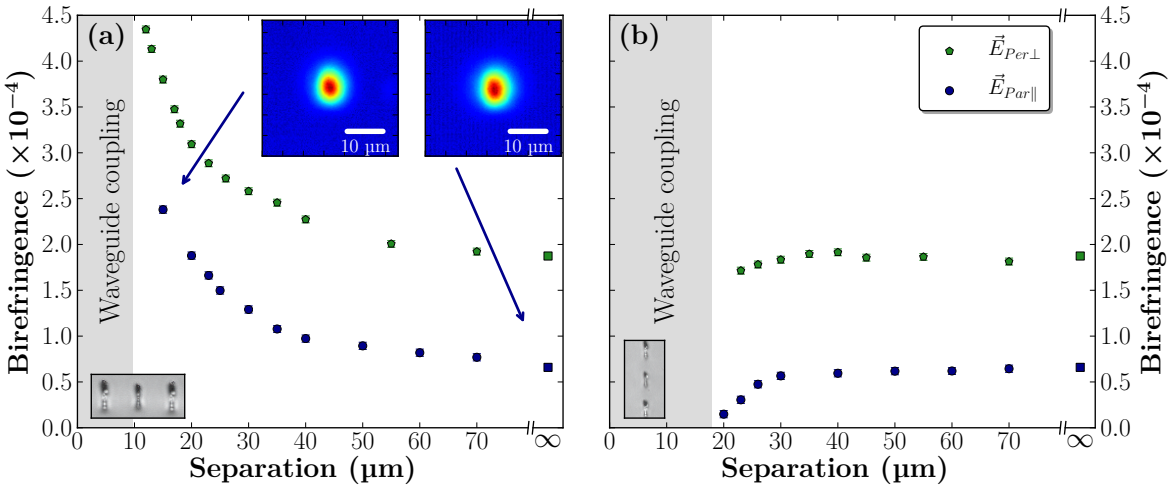

Figure 5.19: Birefringence as a function of the stress track separation for (a) horizontal geometry and (b) vertical geometry, for 200 nJ pulse energy. The blue circles are the results for fabrication with parallel polarization of the writing laser, $\vec{E}_{Par\parallel}$, while the green pentagons are the results for the perpendicular polarization, $\vec{E}_{Per\perp}$, case. The squares at ∞ separation represent the reference BGWs for both writing polarizations.

by 20 µm from the waveguide. Values below the uncertainty of the measurements, $< 4 \times 10^{-6}$, can be reached by using the strongest (250 nJ) stress tracks and the same 20 µm separation.

As seen before [141], the presence of nanogratings aligned parallel to the ultrafast fabricated waveguide (perpendicular polarized laser) greatly increases the waveguide

birefringence. In Fig. 5.19, a birefringence comparison is made between waveguides written with parallel and perpendicular polarizations of the writing laser to study the influence of their stress inducing laser tracks. The birefringence shown as a function of the stress tracks separation clearly follows the same trend for both parallel and perpendicular polarizations of the writing laser. Furthermore, in both cases the stress tracks fabricated with 200 nJ of pulse energy yielded similar increases of 1.72×10^{-4} and 1.93×10^{-4} for the parallel and the perpendicular polarization cases, respectively, when the stress separation was 15 µm in the horizontal geometry approach (Fig. 5.19(a)). Otherwise, differing decreases of 0.35×10^{-4} and 0.17×10^{-4} were found for the vertical stress approach, for the parallel and the perpendicular polarization cases, respectively.

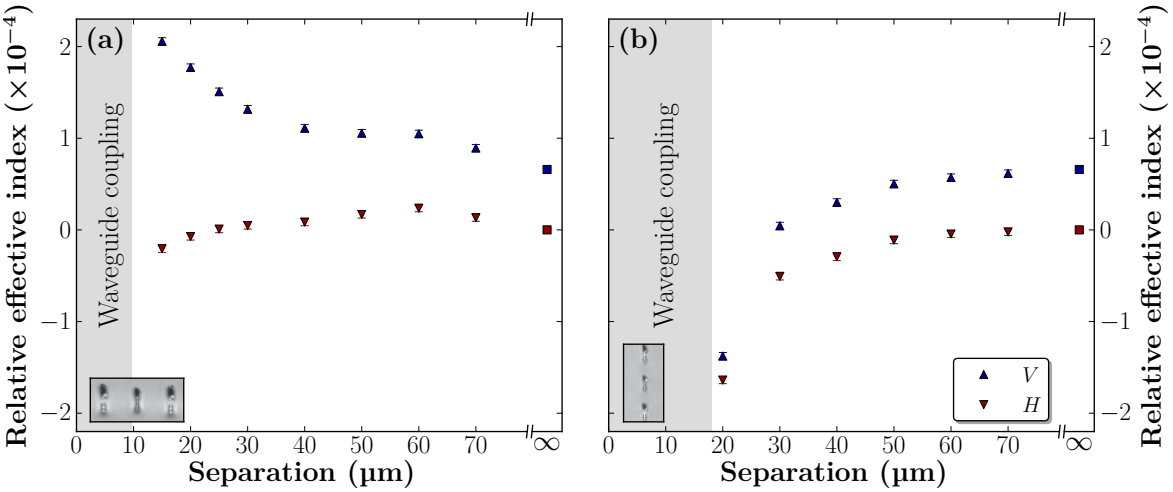

Figure 5.20: Relative effective index of the BGWs, with respect to the effective index of the reference H mode (1.4454), for both V (blue triangles) and H (red inverted triangles) polarization modes as a function of the stress tracks separation. (a) is for the horizontal geometry and (b) is for the vertical geometry, both made with the parallel polarized writing laser and stress tracks produced with 200 nJ pulse energy.

The influence on the individual mode effective indices for both V and H waveguide polarization modes is presented in Fig. 5.20, for varying stress track separations and different stressing geometry. For the horizontal geometry, Fig. 5.20(a) shows that the horizontal material stress produces a large increase in the V mode effective index while a slight decrease is noted in the H mode propagation constant. Figure 5.20(b) shows the results for the vertical stress geometry case, where both V and H modes showed a decrease in the effective index as the modification tracks were fabricated closer to the BGW. The difference between the effective indices for V and H modes in Fig. 5.20 corresponds to the birefringence values reported in Fig. 5.19 and Fig. 5.18.

Only separations above 10 µm for the horizontal approach and above 20 µm for the vertical approach yielded useful birefringence shifts, as shorter distances produced non-negligible coupling between the BGWs and the stress tracks. This coupling region is noted in Fig. 5.18, Fig. 5.19 and Fig. 5.20 by a gray shaded area on the plots. The insets in Fig. 5.18 and Fig. 5.19 show the mode profiles for a select number of devices, supporting the earlier statement that there is no significant change in the mode sizes due to the presence of the stress inducing laser modification lines for the case of parallel polarization of the writing laser. The relatively small separations achieved before significant coupling occurs are due to the fact that the stress inducing tracks were fabricated with different laser pulse energies than the waveguides and therefore have different mode propagation constants.

5.4.7 Discussion

The horizontal tracks were found to add stresses that produced more than a 3-fold increase in the waveguide birefringence (Fig. 5.18(a)), while leaving the overall mode profile of the waveguide largely unaffected, as evidenced by the nearly unchanging elliptical-like mode profile elongated along the z-axis direction (9.9 µm × 11.2 µm) ± 0.2 µm (Table 5.3). The stress modification was most pronounced for the V polarization mode, as noted by the asymmetric response of increasing (decreasing) effective index for vertical (horizontal) polarizations in Fig. 5.20(a). In contrast, the vertical stress tracks reduced the waveguide birefringence (Fig. 5.18(b), Fig. 5.19(b)) while also showing an effective refractive index decrease with decreasing separation for both polarization modes (Fig. 5.20(b)). The mode profile sizes were also little affected for this case, except in the limit of 20 µm separation and with 250 nJ exposure, where the mode ellipticity was reversed, being elongated along the x-axis (12.1 µm × 10.8 µm) ± 0.2 µm (Table 5.3). In this way, such vertical stress tracks offer a new direction for creating symmetric mode waveguides to compensate for asymmetric focusing conditions. Previous methods for fabrication of waveguides with symmetric modes included slit beam shaping [146], astigmatic beam focusing with cylindrical lenses [147], among others. Alternatively, the stress bars will offer a way to tune the mode ellipticity with advantages when designing three-dimensional directional couplers, where the same or different coupling coefficient may be desirable between waveguides that are in or out of plane.

The BGWs can act as sensors of the stresses surrounding the tracks and can be used to probe the stress fields in the material. The data presented is consistent with the observations made from Fig. 5.16, with the horizontal modification tracks adding stresses and inducing a preferential increase in the effective index of the V polarization modes to increase the birefringence, while the vertical modification tracks diminish the waveguide birefringence in the BGWs under test. Based on the results shown in Fig. 5.19, nearly the same directions and shifts were observed independently of the weak birefringence produced by parallel polarization or the strong form birefringence provided by the perpendicular polarization of the writing laser. The material stress seen in Fig. 5.16, together with the results shown in Fig. 5.19, do not affect the nanogratings but rather superimposes their asymmetric stress field onto the waveguides.

The coincidence of the birefringence shifts found for both writing polarization conditions (Fig. 5.19) suggests that the laser stress inducing effects are independent of the writing laser polarization. The nanograting generated form birefringence is only present in the perpendicular polarization case, which is in agreement with the expected nanograting orientation, as the nanogratings generated by the parallel polarized writing have no periodicity components in any of the V and H polarization directions. In contrast, the induced birefringence due to material stress is equally present in both cases.

With the inclusion of stress tracks surrounding the waveguides, it is now possible to tune the birefringence from $< 4 \times 10^{-6}$ up to $2.52{\times}10^{-4}$ with parallel polarization of the writing laser, and from $1.71{\times}10^{-4}$ up to $4.35{\times}10^{-4}$ with perpendicular polarization of the writing laser. The higher birefringence values made available may permit the design of shorter components for polarization beam splitters [140] or wave retarders [141]. Table 5.4 summarizes the characteristics of a zero-order half-wave plate calculated with the birefringence values for each writing condition, and with the total insertion losses projected for that device based on the calculated length and on the propagation losses. A zero-order half-wave plate with as little as 1.8 mm length is possible to be obtained with this technique, which represents more than a two fold decrease in length compared to previous results [141].

The Bragg grating splitting technique was able to unambiguously determine the birefringence, Δn_{eff}, with spectral measurements and with an uncertainty of $\pm 4 \times 10^{-6}$. With the exception of the non-birefringent waveguide, all the waveguides shown have losses comparable to the ones found for single waveguides, without stress inducing

Table 5.4: Summary of maximum and minimum birefringence and minimum zero-order half-wave plate lengths for different waveguide writing conditions.

Writing laser polarization	$\Delta n_{\text{original}}$ ($\pm 4\times10^{-6}$)	$\Delta n_{\max}$ | $\Delta n_{\min}$ ($\pm 4\times10^{-6}$)	Zero-order half-wave plates	
			Minimum length (mm)	Insertion loss (dB)
Para. $\vec{E}_{Par\parallel}$	6.6×10^{-5} ↗	$< 4\times10^{-6}$ (V-stress)	–	–
	→	→	11.7	0.6
	↘	2.52×10^{-4} (H-stress)	3.1	0.2
Perp. $\vec{E}_{Per\perp}$	1.88×10^{-4} ↗	1.71×10^{-4} (V-stress)	–	–
	→	→	4.3	0.3
	↘	4.35×10^{-4} (H-stress)	1.8	0.2

tracks, (1.1±0.1) dB/cm for BGWs and (0.9±0.1) dB/cm for unmodulated waveguides produced with perpendicular, $\vec{E}_{Per\perp}$, and (0.8±0.1) dB/cm for BGWs and (0.5±0.1) dB/cm for unmodulated waveguides produced with parallel, $\vec{E}_{Par\parallel}$, polarization of the writing laser.

The zero birefringence condition found with the closest vertical stress tracks offers a unique opportunity to explore low polarization mode dispersion waveguides. However, the almost 2-fold higher losses found for this stressed waveguide is much higher than found in other laser formed fused silica waveguides, warranting further exploration of laser exposure conditions to provide waveguide birefringence of 10^{-6}.

In order to further increase the range of birefringence values available, closer spacing between the waveguides and the stress tracks could be explored with weaker stressing structures that will neither couple evanescently nor coalesce into a multi-mode waveguide. Alternatively, even stronger laser pulse energies than those available here could be tested to induce stronger birefringence modification effects. More precise diagnostic tools may facilitate demonstration of much lower waveguide birefringence than it was possible to measure here. Post thermal annealing may be explored to further tune this low waveguide birefringence through stress relaxation [42].

There is a significant advantage for many applications to use low birefringent waveguides in order to avoid polarization mode dispersion, while there is also the opportunity to explore higher birefringence values in order to design shorter polarization dependent devices, like the polarization beam splitters and wave retarders. The flexibility of increasing or decreasing the birefringence opens up the option of tuning

the original waveguide birefringence by judicious placing of stress tracks of varying strengths along an optical circuit, without significantly affecting the waveguide mode or the propagation loss, offering more design options in combining various degrees of birefringent and non-birefringent waveguides for integration into more complex polarization devices.

Other geometric arrangements of the stressing tracks could be explored to change the eigenaxes of the polarization modes, perhaps enabling the design of polarization devices to work in different orthogonal directions other than the vertical and horizontal shown here (45° to the current eigenmodes, for example).

5.5 Conclusions

We successfully demonstrated the first femtosecond laser formed buried optical waveguides behaving as discrete quarter-wave and half-wave plates. A 35 dB polarization contrast was found for a half-wave retarder, while there was only a 5% power variation for a quarter-wave device. In this chapter, we further demonstrated two complementary techniques to accurately measure the birefringence in femtosecond laser formed waveguides, and used these techniques to study the birefringence dependence on wavelength and exposure conditions. These retarder devices may prove to be important for future integration into optical circuits required in quantum entanglement experiments and on-chip quantum optics applications.

Femtosecond laser induced birefringence in fused silica waveguides was harnessed here for the first time, to the best of our knowledge, to demonstrate polarization beam splitting in buried optical circuits. Moderately strong extinction ratio of up to -24 dB was noted for 2 cm long devices. The polarization beam splitters are sufficiently wavelength selective to be attractive for WDM application, and promise to open new directions for creating polarization dependent devices in three dimensional optical circuits. However, the means to extend the bandwidth for such polarization splitting will require further design and laser process development.

The integration of the present polarization splitters inside bulk glass defines a highly attractive platform for creating stable and highly functional polarization-dependent optical circuits required today in optical communication and quantum entanglement systems.

This chapter demonstrated the use of stressing tracks in two orientations that enhance or diminish birefringence, with values ranging from $< 4 \times 10^{-6}$ up to 4.35×10^{-4}. There is a negligible effect on mode profiles and waveguide losses by the presence of stress tracks, except in the limit of closely written vertical tracks with the maximum energy available; however, this last condition offers the opportunity to create a symmetric mode profile.

This stress inducing technique provides the ability to master the birefringence effects, which is an area of three-dimensional laser writing that has not been fully explored in the past, and yet shown to be important for advanced integration of femtosecond written optical circuits. The measurements and fabrication techniques shown add more flexibility to modify three-dimensional circuits to insert low birefringence waveguides together with strong polarization devices so as to make a whole range of operations available for the design of compact devices, like polarization beam splitters and wave retarders. While polarization devices may be of key importance for the fabrication of integrated quantum entanglement experiments, the ability to reduce such birefringence may also be of interest, by providing ways of connecting different components with little polarization mode dispersion, which can be favorable for quantum measurements by reducing decoherence of entangled photon pairs or to improve the performance of optical communication systems.

Final conclusions and future work

Femtosecond laser writing of optical devices was explored during this work for the successful demonstration of fiber Bragg gratings (FBGs) in suspended core fibers (SCFs) for temperature and strain sensing, direct point-by-point writing of first order Bragg grating waveguides (BGWs) with chirped and phase shifted spectra for sensing and time domain pulse shaping and control of waveguide birefringence for the fabrication of polarization integrated devices, namely zero-order wave plates and polarization beam splitters.

The FBGs demonstrated in SCFs represent an important step to enable the design of fiber devices in non-photosensitive fibers, which can open the possibility of producing sensing devices or Bragg gratings in fibers that are otherwise difficult to functionalize, such as many different designs of photonic crystal fibers or active material fibers. The SCFs used here were shown to be useful for simultaneous determination of temperature and strain, taking advantage of different suspended core geometries that provided different sensitivity to temperature while maintaining the same sensitivity to strain.

The further development of a point-by-point writing system for the fabrication of BGWs opened the possibility of fast prototyping and flexible design of spectral responses with application in sensors and optical communication. The microfluidic capabilities already established for this platform can take advantage from the advances presented here towards the fabrication of integrated lab-on-a-chip devices with scientific and medical applications that can greatly benefit from the progress on these areas. As a proof of principle, chirped Bragg gratings were demonstrated for application in temporal pulse shaping, acting as a Fourier transformer, while phase shifted Bragg gratings were successfully fabricated with very narrow 22 pm features that can be used for sensing, for distributed feedback laser cavities, or for spectral shaping for optical communications, such as in wavelength division multiplexing devices. Regardless of the demonstrations provided here, the most important aspect of the system is the

flexibility that the computer controlled acousto-optic modulator (AOM) offers for the design of arbitrary spectral features and fast prototyping. Future developments may provide accurate simulation of the relationship between the AOM power modulation and the resulting refractive index modulation in the waveguides, enabling even easier prototyping in a one step fabrication of devices with multiple features, such as frequency modulation, arbitrary phase definition, and apodization.

The sharp features demonstrated in the phase shifted BGWs allowed accurate measurement of waveguide birefringence, which was further studied to determine its writing parameters dependence, as well as the birefringence dispersion characteristics. It was found that the birefringence in femtosecond generated waveguides in fused silica is mostly influenced by the presence of nanogratings located in the waveguide core, which depend on the writing laser polarization, and by the presence of material stress around the core, which happens due to the nonlinear and anisotropic nature of the writing process. Control of the birefringence was explored by changing the writing laser parameters as well as by inducing stress in the material around the core. Birefringence tuning was found to be possible in a range from 10^{-6} to 10^{-4}, enabling both polarization independent and polarization dependent operation. This birefringence was also explored for fabrication of zero-order wave plates, with a 35 dB polarization contrast for a half-wave device and a 5% power variation for a quarter-wave retarder. The design of directional couplers with polarization dependent coupling enabled the fabrication of integrated polarization beam splitters with a -24 dB polarization extinction ratio.

The flexible BGW fabrication, and the polarization control technique demonstrated here, can be readily applied in the development of functional devices in different materials. This provides an ideal tool to access multiple platforms, such as different fiber geometries and active laser materials. One such platform is the cladding of optical fibers. The fiber cladding is not accessible through traditional lithographic fabrication techniques, but can be used for waveguide fabrication with ultrafast direct laser writing technologies. This platform is already widely deployed for photonics technologies applications and can be harnessed for the fabrication of integrated optical waveguides. Devices written in the cladding of optical fibers, together with the ability to design microfluidic structures, further opens the prospects of developing integrated components for lab-on-a-fiber applications in sensing, biophotonics, optofluidics, and telecommunication, as well as polarization devices for fiber lasers and microstructuring for nonlinear applications.

The on-chip polarization control provides the ability to fabricate quantum optic devices with polarization encoding. This approach may be useful in the design of quantum cryptography transmitters and receivers, complex polarization entanglement experiments, and ultimately, quantum gates for optical computing circuits.

Appendix A

Bragg grating shift detection algorithm

The wavelength peak in the spectrum produced by a Bragg grating waveguide (BGW) follows the Bragg relation $\lambda_B = 2\Lambda n_{\text{eff}}$, where λ_B is the reflected Bragg wavelength, n_{eff} is the effective index of the waveguide mode, and Λ is the periodicity of the grating structure. From the Bragg resonance peak it is possible to calculate the effective index of the mode. The birefringence is defined by the difference between the effective indices of the eigenmodes (Vertical and Horizontal in this case), $\Delta n_{\text{eff}} = n_V - n_H$. From the Bragg relation, the birefringence was determined using the difference between the Bragg wavelength peak in Equation A.1.

$$\Delta n_{\text{eff}} = \frac{\Delta \lambda_B}{2\Lambda} \tag{A.1}$$

For accurate determination of λ_B, the experimentally recorded BGW transmission spectra for the two polarization eigenmodes were used. The two modes were selected by adjusting the input polarizer and the transmission spectra were recorded by coupling the output light into the optical spectrum analyzer (OSA). In Equation A.2, $V(\lambda)$ and $H(\lambda)$ are the transmission spectra of a BGW for vertical and horizontal polarizations of the input light, $S(\Delta\lambda)$ is the square difference between the $H(\lambda)$ and $V(\lambda)$ transmission spectra as a function of the $\Delta\lambda$ shift of the H$(\lambda + \Delta\lambda)$ spectrum.

$$S(\Delta\lambda) = \sum_{\lambda=\lambda_{\min}}^{\lambda_{\max}} [V(\lambda) - H(\lambda + \Delta\lambda)]^2 \tag{A.2}$$

The wavelength difference between the $V(\lambda)$ and $H(\lambda)$ spectra, $\Delta\lambda_0$, was calculated with Equation A.3 by determining the minimum of $S(\Delta\lambda)$. Fig. A.1(a) shows the original spectra for $V(\lambda)$ and $H(\lambda)$, while Fig. A.1(b) plots $S(\Delta\lambda)$ as a function of the wavelength shift applied to the $H(\lambda)$ spectrum.

$$\min[S(\Delta\lambda)] = S(\Delta\lambda_0) \tag{A.3}$$

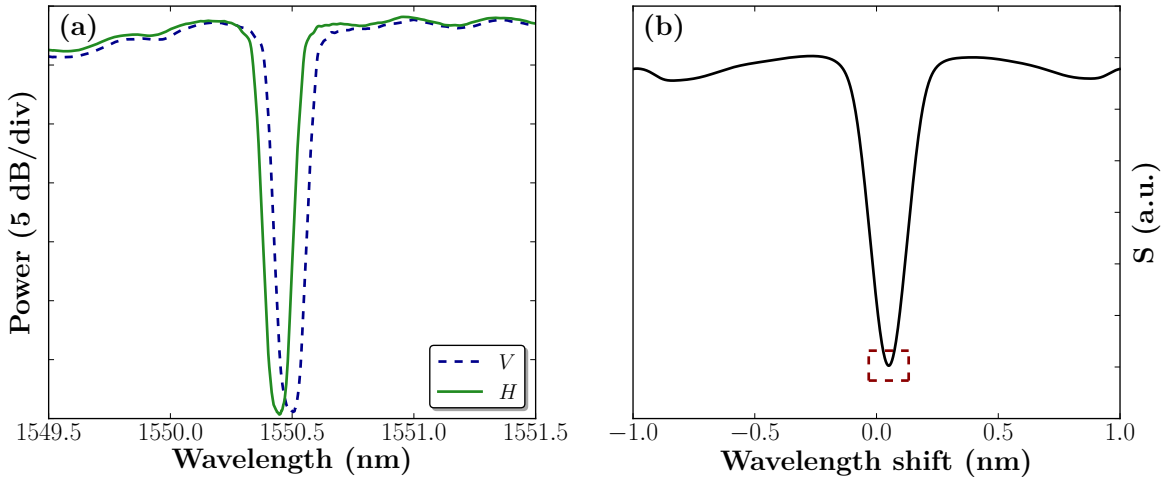

Figure A.1: (a) Original BGWs transmission spectra for vertical and horizontal polarization probing. (b) Sum of the squared differences, $S(\Delta\lambda)$, from Equation A.2.

For a more precise determination of $\Delta\lambda_0$, the three minimum points of $S(\Delta\lambda)$ (red box in Fig. A.1(b)), were specified according to Equation A.4, Equation A.5, and Equation A.6, and are plotted in Fig. A.2(a).

$$S^- = S(\Delta\lambda_0 - \delta_\lambda) \tag{A.4}$$

$$S^+ = S(\Delta\lambda_0 + \delta_\lambda) \tag{A.5}$$

$$\min(S) = S(\Delta\lambda_0) \tag{A.6}$$

The resolution of this measurement was further improved by calculating a correction factor, μ, defined in Equation A.7, which interpolates between the discrete $S(\Delta\lambda)$ data provided by the OSA, with the instrument limited step size being $\delta_\lambda = 0.002$ nm.

$$\mu = \frac{S^- - S^+}{2[S^- + S^+ - 2S_{\min}]} \tag{A.7}$$

The best value for the wavelength shift, $\Delta\lambda_B$, was determined by Equation A.8.

$$\Delta\lambda_B = \Delta\lambda_0 + \mu\delta_\lambda \tag{A.8}$$

This wavelength shift was added to the λ-axis of the $H(\lambda)$ spectrum and plotted together with the unshifted $V(\lambda)$ spectrum in Fig. A.2(b) to demonstrate the close overlapping of the the two spectra, confirming the accuracy of this method.

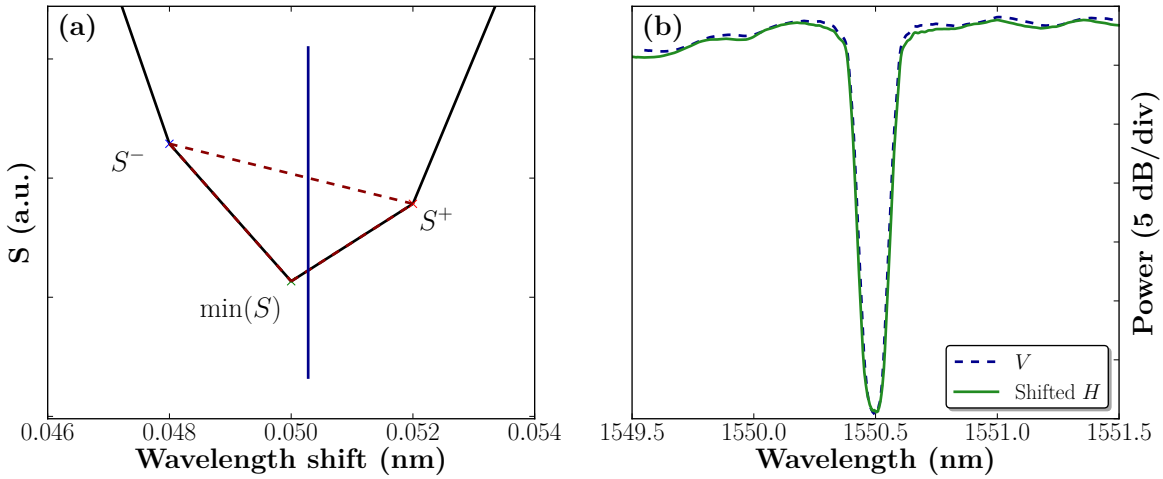

Figure A.2: (a) Zoomed plot of the minimum of the sum of the squared differences showed in Fig. A.1(b). The vertical line represents the corrected minimum point of function $S(\Delta\lambda_0)$ used to determine $\Delta\lambda_B$. (b) BGWs transmission spectra for vertical and horizontal polarizations with the horizontal polarization spectrum shifted by the best fitted value for birefringent wavelength shift, $\Delta\lambda_B$.

The *python* code showed in Code Listing 1 was used to implement this algorithm. The use of *Scipy* package routines greatly improves the execution time of the code,

making it ideal for automated BGW shift detection. The results presented here were computed in less than 50 ms with a 2.20 GHz processor.

The *bgwshift* function defined in Code Listing 1 takes the two spectra as arguments and returns the following variables:

- The input spectra cropped to an even size if their length is odd;
- The calculated shift, *delta*, between the two spectra with the same units as the λ-axis in the original spectra data;
- An array of the square differences, *sqrsum*, between the two spectra as a function of the $\Delta\lambda$ shift;
- The correction factor, μ, shown in Equation A.7, that accounts for the discrete nature of the experimental data;
- The middle point of the *sqrsum* array used to fold the *sqrsum* in its center so that the middle point in the plots represent zero wavelength shift.

```
from scipy import array, zeros, roll

def bgwshift(spec1, spec2):

    if spec1.shape[1] % 2: # Resize the spectra if their size is odd
        spec1 = array([(spec1[0][0:-1]), (spec1[1][0:-1])])
        spec2 = array([(spec2[0][0:-1]), (spec2[1][0:-1])])

    size = spec1[0].size
    sqrsum = zeros(size) # Creates an array with the same size as the spectra

    for j in range(size):
        shifted_spec2 = roll(spec2[1], j)
        sqrdiff = (spec1[1] - shifted_spec2)**2
        sqrsum[j] = sqrdiff.sum()

    mid = size/2 # Middle point used to fold the sqrsum array.

    # Folding sqrsum in its center.
    # After this step, the middle point represents no shift between spec1 and spec2
    sqrsum = roll(sqrsum, mid)
    minpoint = sqrsum.argmin()

    sminus   = float(sqrsum[minpoint-1])
    smin     = float(sqrsum[minpoint])
    splus    = float(sqrsum[minpoint+1])

    correction = (sminus - splus) / (sminus + splus - 2*smin) / 2
    correction_value = (spec1[0][minpoint]-spec1[0][minpoint-1])*correction
    delta = spec1[0][minpoint]-spec1[0][mid] + correction_value

    return spec1, spec2, delta, sqrsum, correction, mid
```

Code Listing 1: *bgwshift* function implemented in python.

Appendix B

Fused silica substrate

Fused silica, also known as fused quartz or quartz glass, was the material of choice for most of the work presented in this thesis, mostly due to the low loss (high transmission, Fig. B.1) of this material at infrared wavelengths, as well as the availability as high quality substrates.

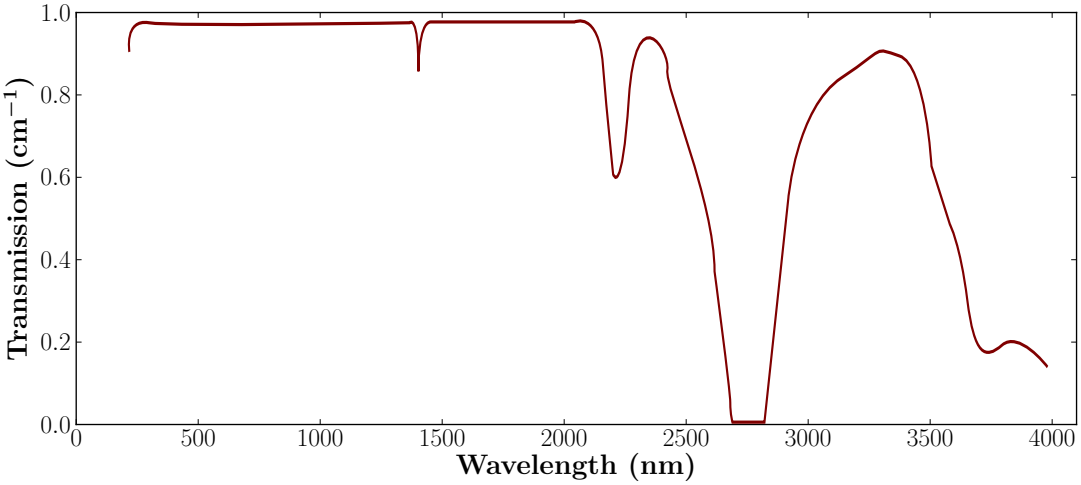

Figure B.1: Transmission spectrum of Corning 7980 fused silica glass as provided by the manufacturer (*Corning Incorporated*).

The most important physical quantity to consider when studying the optical properties of a transparent material is the index of refraction. The refractive index and the dispersion of fused silica can be described by Equation B.1, where $n(\lambda)$ is the refractive index as a function of the wavelength, λ is the wavelength, and B_1, B_2, B_3 and C_1, C_2, C_3 are the empirically determined Sellmeier coefficients [148] listed in Table B.1.

$$n^2(\lambda) = 1 + \frac{B_1\lambda^2}{\lambda^2 - {C_1}^2} + \frac{B_2\lambda^2}{\lambda^2 - {C_2}^2} + \frac{B_3\lambda^2}{\lambda^2 - {C_3}^2} \tag{B.1}$$

This approximation is valid for room temperature (20℃) and for the spectral region between 0.21 µm and 3.71 µm [148], where fused silica is transparent. This expression was later shown to be also valid for the spectral region between 3 µm and 6.7 µm [149]. In Table B.1 the Sellmeier coefficients are shown for standard fused silica as well as for Corning 7980, a high purity silica manufactured by flame hydrolysis, which is the material used in this thesis for the fabrication of integrated waveguides in bulk glass by femtosecond laser writing. Despite the difference in the Sellmeier coefficients, the difference between standard fused silica and the Corning 7980 glass, as determined by the Sellmeier equation B.1, is less than 5×10^{-5} for wavelengths shorter than 1600 nm. The data presented for Corning 7980 fused silica are provided by the manufacturer.

Table B.1: Sellmeier coefficients for fused silica

Sellmeier coefficients	Standard Fused silica	Corning 7980
B_1	0.6961663	0.683740494
B_2	0.4079426	0.420323613
B_3	0.8974794	0.585027480
C_1	0.0684043 µm	0.0678493087 µm
C_2	0.1162414 µm	0.1157449161 µm
C_3	9.8961610 µm	8.0307703989 µm

Table B.2 summarizes properties of fused silica that are relevant for the application in optics and photonics presented in this thesis.

Table B.2: Summary of fused silica properties

Property	Value
Density	2.203 g/cm^3
Coefficient of thermal expansion*	5.5×10^{-7} K^{-1}
Softening point	1665 ℃
Annealing point	1140 ℃
Strain point	1070 ℃

*Average from 20 ℃ to 320 ℃.

The refractive index is also dependent on the temperature. Following the same approach taken for room temperature, at each temperature it is possible to calculate

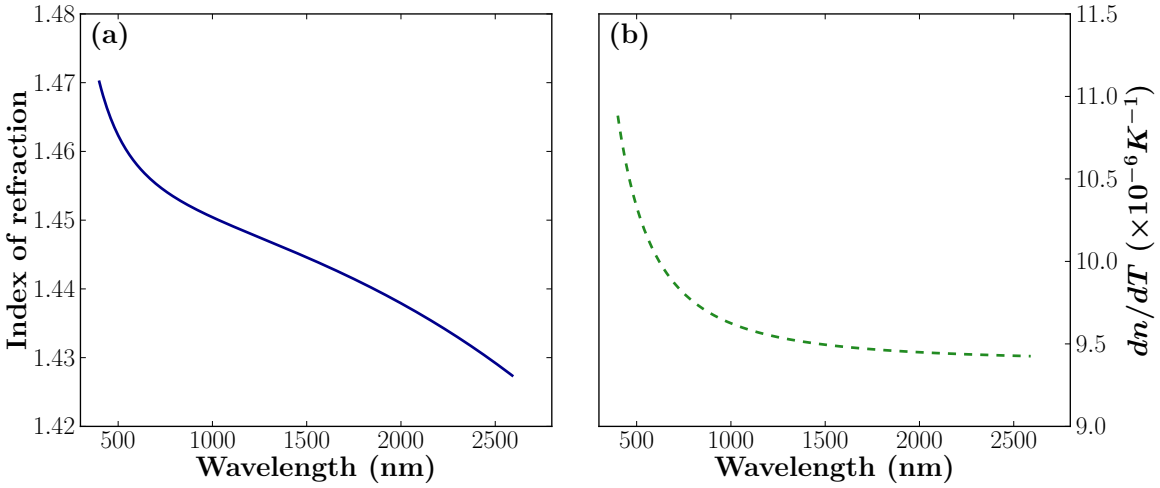

Figure B.2: Fused silica index of refraction (a) and thermo-optical coefficient (b) as a function of wavelength.

suitable Sellmeier coefficients. Furthermore, these coefficients can also be empirically modeled as functions of temperature.

$$n^2(\lambda) = 1 + \sum_{i=1}^{3} \frac{S_i(T).\lambda^2}{\lambda^2 - C_i(T)^2} \tag{B.2}$$

Equation B.2 was experimentally determined for wavelengths ranging from 400 nm to 2.6 µm, and temperatures between 30 K and 300 K [72]. The Sellmeier coefficients, $S_i(T)$ and $C_i(T)$, in Equation B.2 are determined with Equation B.3 and Equation B.4, with a fourth order temperature dependence model with the coefficients S_{ij} and C_{ij} presented in Table B.3.

$$S_i(T) = \sum_{j=0}^{4} S_{ij} T^j \tag{B.3}$$

$$C_i(T) = \sum_{j=0}^{4} C_{ij} T^j \tag{B.4}$$

Table B.3: S_{ij} and C_{ij} coefficients for the temperature dependent Sellmeier equation

Temperature term	S_1	S_2	S_3	Units
T^0, Constant term	1.10127	1.78752×10^{-5}	7.93552×10^{-1}	
T^1	-4.94251×10^{-5}	4.76391×10^{-5}	-1.27815×10^{-3}	K^{-1}
T^2	5.27414×10^{-7}	-4.49019×10^{-7}	1.84595×10^{-5}	K^{-2}
T^3	-1.59700×10^{-9}	1.44546×10^{-9}	-9.20275×10^{-8}	K^{-3}
T^4	1.75949×10^{-12}	-1.57223×10^{-12}	1.48829×10^{-10}	K^{-4}
	C_1	C_2	C_3	
T^0, Constant term	-8.90600×10^{-2}	2.97562×10^{-1}	9.34454	µm
T^1	9.08730×10^{-6}	-8.59578×10^{-4}	-7.09788×10^{-3}	$\mu\mathrm{m\,K}^{-1}$
T^2	-6.53638×10^{-8}	6.59069×10^{-6}	1.01968×10^{-4}	$\mu\mathrm{m\,K}^{-2}$
T^3	7.77072×10^{-11}	-1.09482×10^{-8}	-5.07660×10^{-7}	$\mu\mathrm{m\,K}^{-3}$
T^4	6.84605×10^{-14}	7.85145×10^{-13}	8.21348×10^{-10}	$\mu\mathrm{m\,K}^{-4}$

Appendix C

Tools and software

This thesis was prepared in LaTeX and it was based on the template available at the website of the Department of Computer Science of the Faculty of Science of the University of Porto. The template was further modified by the author, and a full version is available online: www.luisfernandes.org.

Plots and data analysis were preformed entirely using the Python programing language. This language is very flexible and provides an excellent platform for simple calculations as well as data plots, while also possessing the scalability, through python modules, required for advanced computations and implantation of complex algorithms.

The SciPy and the NumPy modules are examples of such python modules and were used for most of these computations, namely and most importantly, for the implementations of the Levenberg-Marquardt least square algorithm, which is part of the SciPy optimization and root finding (scipy.optimize) package. These modules also provide fast computation of arrays and matrices for processing large amounts of data, which was proven to be particularly useful for processing of spectral data.

The Matplotlib python module was used to produce all the plot representations of data and functions, as this module also provides a lot of flexibility to best design ways of effectively present the experimental results, together with high quality graphics. The PyVISA module was extensively used to interface laboratory equipment with the computer through the GPIB interface, greatly improving the data collection procedure in terms of speed and reliability.

Vector graphics for schematic pictures were designed with Inkscape, while three dimensional graphic and animation rendering was performed using FreeCAD and Blender.

All these tools are open source software and are, in the authors opinion, some of the best tools for professional design of high quality pictures, and provide accurate data analysis for scientific manuscript preparation purposes.

References

[1] K. Levenberg, "A method for the solution of certain non-linear problems in least squares." *Quarterly of Applied Mathematics*, vol. 2, pp. 164–168, 1944.
Referenced in page(s): 25

[2] D. W. Marquardt, "An Algorithm for Least-Squares Estimation of Nonlinear Parameters," *Journal of the Society for Industrial and Applied Mathematics*, vol. 11, no. 2, pp. 431–441, 1963.
Referenced in page(s): 25

[3] E. Hecht, *Optics*, 4th ed. Addison-Wesley, 2001.
Referenced in page(s): 26

[4] S. Nolte, M. Will, J. Burghoff, and A. Tuennermann, "Femtosecond waveguide writing: a new avenue to three-dimensional integrated optics," *Applied Physics A: Materials Science and Processing*, vol. 77, no. 1, pp. 109–111, 2003.
Referenced in page(s): 30, 31, 112

[5] A. M. Kowalevicz, V. Sharma, E. P. Ippen, J. G. Fujimoto, and K. Minoshima, "Three-dimensional photonic devices fabricated in glass by use of a femtosecond laser oscillator," *Optics Letters*, vol. 30, no. 9, pp. 1060–1062, 2005.
Referenced in page(s): 30, 31

[6] S. M. Eaton, W. J. Chen, H. Zhang, R. Iyer, J. Li, M. L. Ng, S. Ho, J. S. Aitchison, and P. R. Herman, "Spectral loss characterization of femtosecond laser written waveguides in glass with application to demultiplexing of 1300 and 1550 nm wavelengths," *Lightwave Technology, Journal of*, vol. 27, no. 9, pp. 1079–1085, 2009.
Referenced in page(s): 30, 31, 92

[7] K. M. Davis, K. Miura, N. Sugimoto, and K. Hirao, "Writing waveguides in glass with a femtosecond laser," *Optics Letters*, vol. 21, no. 21, pp. 1729–1731, 1996.
Referenced in page(s): 31, 33, 59

[8] H. Zhang, S. M. Eaton, and P. R. Herman, "Single-step writing of Bragg grating waveguides in fused silica with an externally modulated femtosecond fiber laser," *Optics Letters*, vol. 32, no. 17, pp. 2559–2561, 2007.
Referenced in page(s): 31, 44, 74, 75, 113

[9] R. Osellame, N. Chiodo, G. D. Valle, S. Taccheo, R. Ramponi, G. Cerullo, A. Killi, U. Morgner, M. Lederer, and D. Kopf, "Optical waveguide writing with a diode-pumped femtosecond oscillator," *Optics Letters*, vol. 29, no. 16, pp. 1900–1902, 2004.
Referenced in page(s): 31

[10] M. Ams, P. Dekker, G. D. Marshall, and M. J. Withford, "Monolithic 100 mW Yb waveguide laser fabricated using the femtosecond-laser direct-write technique," *Optics Letters*, vol. 34, no. 3, pp. 247–249, 2009.
Referenced in page(s): 31, 37, 73

[11] K. Suzuki, V. Sharma, J. G. Fujimoto, E. P. Ippen, and Y. Nasu, "Characterization of symmetric [3 x 3] directional couplers fabricated by direct writing with a femtosecond laser oscillator," *Optics Express*, vol. 14, no. 6, pp. 2335–2343, 2006.
Referenced in page(s): 31

[12] M. H. Hong, B. Luk'Yanchuk, S. M. Huang, T. Ong, L. H. Van, and T. C. Chong, "Femtosecond laser application for high capacity optical data storage," *Applied Physics A: Materials Science and Processing*, vol. 79, no. 4, pp. 791–794, 2004.
Referenced in page(s): 31

[13] B. C. Stuart, M. D. Feit, S. Herman, A. M. Rubenchik, B. W. Shore, and M. D. Perry, "Nanosecond-to-femtosecond laser-induced breakdown in dielectrics," *Physical Review B*, vol. 53, pp. 1749–1761, 1996.
Referenced in page(s): 33

[14] C. B. Schaffer, A. Brodeur, and E. Mazur, "Laser-induced breakdown and damage in bulk transparent materials induced by tightly focused femtosecond laser pulses," *Measurement Science and Technology*, vol. 12, no. 11, p. 1784, 2001.
Referenced in page(s): 33, 38

[15] H. Misawa and S. Juodkazis, *3D Laser Microfabrication: Principles and Applications*. John Wiley & Sons, 2006.
Referenced in page(s): 33

[16] R. R. Gattass and E. Mazur, "Femtosecond laser micromachining in transparent materials," *Nature Photonics*, vol. 2, no. 4, pp. 219–225, 2008.
Referenced in page(s): 33, 34

[17] R. Osellame, G. Cerullo, and R. Ramponi, *Femtosecond Laser Micromachining*, ser. Topics in Applied Physics. Springer-Verlag, 2012, vol. 123.
Referenced in page(s): 33

[18] M. J. Madou, *Fundamentals of Microfabrication: The Science of Miniaturization*. CRC Press, 2002.
Referenced in page(s): 34

[19] S. Kawata, H. B. Sun, T. Tanaka, and K. Takada, "Finer features for functional microdevices," *Nature*, vol. 412, no. 6848, pp. 697–698, 2001.
Referenced in page(s): 34

[20] N. Tétreault, G. von Freymann, M. Deubel, M. Hermatschweiler, F. Pérez-Willard, S. John, M. Wegener, and G. A. Ozin, "New Route to Three-Dimensional Photonic Bandgap Materials: Silicon Double Inversion of Polymer Templates," *Advanced Materials*, vol. 18, no. 4, pp. 457–460, 2006.
Referenced in page(s): 35

[21] S. Eaton, H. Zhang, P. R. Herman, F. Yoshino, L. Shah, J. Bovatsek, and A. Arai, "Heat accumulation effects in femtosecond laser-written waveguides with variable repetition rate," *Optics Express*, vol. 13, no. 12, pp. 4708–4716, 2005.
Referenced in page(s): 35

[22] C. B. Schaffer, J. F. García, and E. Mazur, "Bulk heating of transparent materials using a high-repetition-rate femtosecond laser," *Applied Physics A: Materials Science and Processing*, vol. 76, no. 3, pp. 351–354, 2003.
Referenced in page(s): 35

[23] S. M. Eaton, H. Zhang, M. L. Ng, J. Li, W. J. Chen, S. Ho, and P. R. Herman, "Transition from thermal diffusion to heat accumulation in high repetition rate femtosecond laser writing of buried optical waveguides," *Optics Express*, vol. 16, no. 13, pp. 9443–9458, 2008.
Referenced in page(s): 35, 37, 92, 111, 112

[24] K. Sokolowski-Tinten, J. Bialkowski, A. Cavalleri, M. Boing, H. Schueler, and D. von der Linde, "Dynamics of femtosecond-laser-induced ablation from solid surfaces," in *Proceedings of SPIE*, vol. 3343, 1998, p. 46.
Referenced in page(s): 35

[25] L. Shah, J. Tawney, M. Richardson, and K. Richardson, "Femtosecond laser deep hole drilling of silicate glasses in air," *Applied surface science*, vol. 183, no. 3-4, pp. 151–164, 2001.
Referenced in page(s): 35

[26] Y. Li, K. Itoh, W. Watanabe, K. Yamada, D. Kuroda, J. Nishii, and Y. Jiang, "Three-dimensional hole drilling of silica glass from the rear surface with femtosecond laser pulses," *Optics Letters*, vol. 26, no. 23, pp. 1912–1914, 2001.
Referenced in page(s): 35

[27] E. Vanagas, J. Kawai, D. Tuzhilin, I. Kudryashov, A. Mizuyama, K. G. Nakamura, K.-I. Kondo, S.-y. Koshihara, M. Takesada, K. Matsuda, S. Juodkazis, V. Jarutis, S. Matsuo, and H. Misawa, "Glass cutting by femtosecond pulsed irradiation," *Journal of Microlithography, Microfabrication, and Microsystems*, vol. 3, p. 358, 2004.
Referenced in page(s): 35

[28] F. Ahmed, M. Lee, H. Sekita, T. Sumiyoshi, and M. Kamata, "Display glass cutting by femtosecond laser induced single shot periodic void array," *Applied Physics A: Materials Science and Processing*, vol. 93, no. 1, pp. 189–192, 2008.
Referenced in page(s): 35

[29] D. Strickland and G. Mourou, "Compression of amplified chirped optical pulses," *Optics Communications*, vol. 56, no. 3, pp. 219–221, 1985.
Referenced in page(s): 36

[30] A. Marcinkevičius, S. Juodkazis, M. Watanabe, M. Miwa, S. Matsuo, H. Misawa, and J. Nishii, "Femtosecond laser-assisted three-dimensional microfabrication in silica," *Optics Letters*, vol. 26, no. 5, pp. 277–279, 2001.
Referenced in page(s): 36

[31] C. Hnatovsky, R. S. Taylor, E. Simova, V. R. Bhardwaj, D. M. Rayner, and P. B. Corkum, "Polarization-selective etching in femtosecond laser-assisted microfluidic channel fabrication in fused silica," *Optics Letters*, vol. 30, no. 14, pp. 1867–1869, 2005.
Referenced in page(s): 36

[32] S. Kiyama, S. Matsuo, S. Hashimoto, and Y. Morihira, "Examination of Etching Agent and Etching Mechanism on Femotosecond Laser Microfabrication of Channels Inside Vitreous Silica Substrates†," *The Journal of Physical Chemistry C*, vol. 113, no. 27, pp. 11 560–11 566, 2009.
Referenced in page(s): 36

[33] S. Rajesh and Y. Bellouard, "Towards fast femtosecond laser micromachining of fused silica: The effect of deposited energy." *Optics Express*, vol. 18, no. 20, pp. 21 490–21 497, 2010.
Referenced in page(s): 37

[34] R. Taylor, C. Hnatovsky, and E. Simova, "Applications of femtosecond laser induced self-organized planar nanocracks inside fused silica glass," *Laser & Photonics Reviews*, vol. 2, no. 1-2, pp. 26–46, 2008.
Referenced in page(s): 37, 73

[35] C. Hnatovsky, R. S. Taylor, E. Simova, P. P. Rajeev, D. M. Rayner, V. R. Bhardwaj, and P. B. Corkum, "Fabrication of microchannels in glass using focused femtosecond laser radiation and selective chemical etching," *Applied Physics A: Materials Science and Processing*, vol. 84, no. 1, pp. 47–61, 2006.
Referenced in page(s): 37

[36] J. Siebenmorgen, T. Calmano, K. Petermann, and G. Huber, "Highly efficient Yb:YAG channel waveguide laser written with a femtosecond-laser," *Optics Express*, vol. 18, no. 15, pp. 16 035–16 041, 2010.
Referenced in page(s): 37

[37] F. M. Bain, A. A. Lagatsky, R. R. Thomson, N. D. Psaila, N. V. Kuleshov, A. K. Kar, W. Sibbett, and C. T. A. Brown, "Ultrafast laser inscribed Yb:KGd(WO4)2 and Yb:KY(WO4)2 channel waveguide lasers," *Optics Express*, vol. 17, no. 25, pp. 22 417–22 422, 2009.
Referenced in page(s): 37

[38] A. G. Okhrimchuk, V. K. Mezentsev, V. V. Dvoyrin, A. S. Kurkov, E. M. Sholokhov, S. K. Turitsyn, A. V. Shestakov, and I. Bennion, "Waveguide-saturable absorber fabricated by femtosecond pulses in YAG:Cr4+ crystal for Q-switched operation of Yb-fiber laser," *Optics Letters*, vol. 34, no. 24, pp. 3881–3883, 2009.
Referenced in page(s): 37

[39] A. G. Okhrimchuk, A. V. Shestakov, I. Khrushchev, and J. Mitchell, "Depressed cladding, buried waveguide laser formed in a YAG:Nd3+ crystal by femtosecond laser writing," *Optics Letters*, vol. 30, no. 17, pp. 2248–2250, 2005.
Referenced in page(s): 37

[40] K. Sugioka, Y. Cheng, and K. Midorikawa, "Three-dimensional micromachining of glass using femtosecond laser for lab-on-a-chip device manufacture," *Applied Physics A: Materials Science and Processing*, vol. 81, pp. 1–10, 2005.
Referenced in page(s): 37

[41] K. Yamada, W. Watanabe, T. Toma, K. Itoh, and J. Nishii, "In situ observation of photoinduced refractive-index changes in filaments formed in glasses by femtosecond laser pulses," *Optics Letters*, vol. 26, no. 1, pp. 19–21, 2001.
Referenced in page(s): 38

[42] V. R. Bhardwaj, P. B. Corkum, D. M. Rayner, C. Hnatovsky, E. Simova, and R. S. Taylor, "Stress in femtosecond-laser-written waveguides in fused silica," *Optics Letters*, vol. 29, no. 12, pp. 1312–1314, 2004.
Referenced in page(s): 39, 92, 111, 124

[43] W. Yang, P. G. Kazansky, and Y. P. Svirko, "Non-reciprocal ultrafast laser writing," *Nature Photonics*, vol. 2, no. 2, pp. 99–104, 2008.
Referenced in page(s): 39, 114

[44] L. Shah, A. Arai, S. Eaton, and P. R. Herman, "Waveguide writing in fused silica with a femtosecond fiber laser at 522 nm and 1 MHz repetition rate," *Optics Express*, vol. 13, no. 6, pp. 1999–2006, 2005.
Referenced in page(s): 45

[45] S. Eaton, "Contrasts in Thermal Dffusion and Heat Accumulation Effects in the Fabrication of Waveguides in Glasses using Variable Repetition Rate Femtosecond Laser," Ph.D. dissertation, 2008.
Referenced in page(s): 55

[46] H. Zhang, "Bragg grating waveguide devices: discovery, optimization, and application," Ph.D. dissertation, 2007.
Referenced in page(s): 55, 56

[47] J. C. Knight, T. A. Birks, P. S. Russell, and D. M. Atkin, "All-silica single-mode optical fiber with photonic crystal cladding," *Optics Letters*, vol. 21, no. 19, pp. 1547–1549, 1996.
Referenced in page(s): 58

[48] A. S. Webb, F. Poletti, D. J. Richardson, and J. K. Sahu, "Suspended-core holey fiber for evanescent-field sensing," *Optical Engineering*, vol. 46, p. 010503, 2007.
Referenced in page(s): 58

[49] M. C. P. Huy, G. Laffont, V. Dewynter, P. Ferdinand, P. Roy, J. L. Auguste, D. Pagnoux, W. Blanc, and B. Dussardier, "Three-hole microstructured optical fiber for efficient fiber Bragg grating refractometer," *Optics Letters*, vol. 32, no. 16, pp. 2390–2392, 2007.
Referenced in page(s): 58

[50] V. S. Afshar, S. C. Warren-Smith, and T. M. Monro, "Enhancement of fluorescence-based sensing using microstructured optical fibres," *Optics Express*, vol. 15, no. 26, pp. 17 891–17 901, 2007.
Referenced in page(s): 58

[51] L. Fu, B. K. Thomas, and L. Dong, "Efficient supercontinuum generations in silica suspended core fibers," *Optics Express*, vol. 16, no. 24, pp. 19 629–19 642, 2008.
Referenced in page(s): 58

[52] O. Frazao, J. M. Baptista, J. L. Santos, J. Kobelke, and K. Schuster, "Strain and temperature characterisation of sensing head based on suspended-core fibre in Sagnac interferometer," *Electronics Letters*, vol. 44, no. 25, pp. 1455–1456, 2008.
Referenced in page(s): 58

[53] H. R. Sørensen, J. B. Jensen, J. B. Jensen, F. Bruyere, and K. P. Hansen, "Practical hydrogen loading of air silica fibres," *Bragg Gratings, Poling and Photosensitivity*, pp. 247–249, 2005.
Referenced in page(s): 58

[54] N. Groothoff, J. Canning, E. Buckley, K. Lyttikainen, and J. Zagari, "Bragg gratings in air-silica structured fibers," *Optics Letters*, vol. 28, no. 4, pp. 233–235, 2003.
Referenced in page(s): 59

[55] B. O. Guan, D. Chen, Y. Zhang, H. J. Wang, and H. Y. Tam, "Bragg gratings in pure-silica polarization-maintaining photonic crystal fiber," *Photonics Technology Letters, IEEE*, vol. 20, no. 23, pp. 1980–1982, 2008.
Referenced in page(s): 59

[56] S. J. Mihailov, C. W. Smelser, D. Grobnic, R. B. Walker, P. Lu, H. Ding, and J. Unruh, "Bragg gratings written in all-SiO2 and Ge-doped core fibers with 800-nm femtosecond radiation and a phase mask," *Lightwave Technology, Journal of*, vol. 22, no. 1, pp. 94–100, 2004.
Referenced in page(s): 59

[57] M. Dubov, V. Mezentsev, I. Bennion, and D. N. Nikogosyan, "UV femtosecond laser inscribes a 300 nm period nanostructure in a pure fused silica," *Measurement Science and Technology*, vol. 18, p. L15, 2007.
Referenced in page(s): 59

[58] A. Dragomir, D. N. Nikogosyan, K. A. Zagorulko, P. G. Kryukov, and E. M. Dianov, "Inscription of fiber Bragg gratings by ultraviolet femtosecond radiation," *Optics Letters*, vol. 28, no. 22, pp. 2171–2173, 2003.
Referenced in page(s): 59

[59] K. Zagorulko, P. Kryukov, Y. Larionov, A. Rybaltovsky, E. Dianov, S. Chekalin, Y. Matveets, and V. Kompanets, "Fabrication of fiber Bragg gratings with 267 nm femtosecond radiation," *Optics Express*, vol. 12, no. 24, pp. 5996–6001, 2004.
Referenced in page(s): 59

[60] L. Fu, G. D. Marshall, J. A. Bolger, P. Steinvurzel, E. C. Magi, M. J. Withford, and B. J. Eggleton, "Femtosecond laser writing Bragg gratings in pure silica photonic crystal fibres," *Electronics Letters*, vol. 41, no. 11, pp. 638–640, 2005.
Referenced in page(s): 59

[61] M. G. Sceats, G. R. Atkins, and S. Poole, "Photolytic index changes in optical fibers," *Annual Review of Materials Science*, vol. 23, no. 1, pp. 381–410, 1993.
Referenced in page(s): 59

[62] L. Skuja, "Optically active oxygen-deficiency-related centers in amorphous silicon dioxide," *Journal of Non-Crystalline Solids*, vol. 239, no. 1, pp. 16–48, 1998.
Referenced in page(s): 59

[63] M. Livitziis and S. Pissadakis, "Bragg grating recording in low-defect optical fibers using ultraviolet femtosecond radiation and a double-phase mask interferometer," *Optics Letters*, vol. 33, no. 13, pp. 1449–1451, 2008.
Referenced in page(s): 59

[64] M. Becker, L. A. Fernandes, M. Rothhardt, S. Bruckner, K. Schuster, J. Kobelke, O. Frazao, H. Bartelt, and P. V. S. Marques, "Inscription of fiber Bragg grating arrays in pure silica suspended core fibers," *Photonics Technology Letters, IEEE*, vol. 21, no. 19, pp. 1453–1455, 2009.
Referenced in page(s): 60, 65

[65] M. L. Dockney, S. W. James, and R. P. Tatam, "Fibre Bragg gratings fabricated using a wavelength tuneable laser source and a phase mask based interferometer," *Measurement Science and Technology*, vol. 7, p. 445, 1996.
Referenced in page(s): 60

[66] C. Li, Y. M. Zhang, X. F. Tian, and B. H. Xiong, "Study of wedge-adjusted Talbot interferometer for writing fiber gratings with variable inscribed Bragg wavelengths," *Optical Engineering*, vol. 42, p. 3452, 2003.
Referenced in page(s): 60

[67] M. Becker, J. Bergmann, S. Brückner, M. Franke, E. Lindner, M. W. Rothhardt, and H. Bartelt, "Fiber Bragg grating inscription combining DUV sub-picosecond laser pulses and two-beam interferometry," *Optics Express*, vol. 16, no. 23, pp. 19 169–19 178, 2008.
Referenced in page(s): 60

[68] T. Geernaert, T. Nasilowski, K. Chah, M. Szpulak, J. Olszewski, G. Statkiewicz, J. Wojcik, K. Poturaj, W. Urbanczyk, M. Becker, M. Rothhardt, H. Bartelt, F. Berghmans, and H. Thienpont, "Fiber Bragg gratings in germanium-doped highly birefringent microstructured optical fibers," *Photonics Technology Letters, IEEE*, vol. 20, no. 8, pp. 554–556, 2008.
Referenced in page(s): 60

[69] Y. Wang, H. Bartelt, S. Brueckner, J. Kobelke, M. Rothhardt, K. Mörl, W. Ecke, and R. Willsch, "Splicing Ge-doped photonic crystal fibers using commercial fusion splicer with default discharge parameters," *Optics Express*, vol. 16, no. 10, pp. 7258–7263, 2008.
Referenced in page(s): 60

[70] R. C. Kamikawachi, I. Abe, A. S. Paterno, H. J. Kalinowski, M. Muller, J. L. Pinto, and J. L. Fabris, "Determination of thermo-optic coefficient in liquids with fiber Bragg grating refractometer," *Optics Communications*, vol. 281, no. 4, pp. 621–625, 2008.
Referenced in page(s): 67

[71] T. F. Retajczyk and A. K. Sinha, "Elastic stiffness and thermal expansion coefficients of various refractory silicides and silicon nitride films," *Thin Solid Films*, vol. 70, no. 2, pp. 241–247, 1980.
Referenced in page(s): 67

[72] D. B. Leviton and B. J. Frey, "Temperature-dependent absolute refractive index measurements of synthetic fused silica," in *Proceedings of SPIE*, vol. 6273, 2006, p. 62732K.
Referenced in page(s): 67, 139

[73] H. Bach and N. Neuroth, *The properties of optical glass*. Springer Verlag, 1995.
Referenced in page(s): 67

[74] A. Chryssis, S. S. Saini, S. M. Lee, and M. Dagenais, "Increased sensitivity and parametric discrimination using higher order modes of etched-core fiber Bragg grating sensors," *Photonics Technology Letters, IEEE*, vol. 18, no. 1, pp. 178–180, 2006.
Referenced in page(s): 67

[75] C. Kim and C. B. Su, "Measurement of the refractive index of liquids at 1.3 and 1.5 micron using a fibre optic Fresnel ratio meter," *Measurement Science and Technology*, vol. 15, p. 1683, 2004.
Referenced in page(s): 67

[76] K. O. Hill and G. Meltz, "Fiber Bragg grating technology fundamentals and overview," *Lightwave Technology, Journal of*, vol. 15, no. 8, pp. 1263–1276, 1997.
Referenced in page(s): 69

[77] W. Jin, W. C. Michie, G. Thursby, M. Konstantaki, and B. Culshaw, "Simultaneous measurement of strain and temperature: error analysis," *Optical Engineering*, vol. 36, p. 598, 1997.
Referenced in page(s): 70

[78] K. O. Hill, Y. Fujii, D. C. Johnson, and B. Kawasaki, "Photosensitivity in optical fiber waveguides: Application to reflection filter fabrication," *Applied Physics Letters*, vol. 32, no. 10, pp. 647–649, 1978.
Referenced in page(s): 73

[79] G. Meltz, W. W. Morey, and W. H. Glenn, "Formation of Bragg gratings in optical fibers by a transverse holographic method," *Optics Letters*, vol. 14, no. 15, pp. 823–825, 1989.
Referenced in page(s): 73

[80] H. Zhang and P. R. Herman, "Chirped Bragg Grating Waveguides Directly Written Inside Fused Silica Glass With an Externally Modulated Ultrashort Fiber Laser," *Photonics Technology Letters, IEEE*, vol. 21, no. 5, pp. 277–279, 2009.
Referenced in page(s): 73, 78

[81] C. Monat, P. Domachuk, and B. J. Eggleton, "Integrated optofluidics: A new river of light," *Nature Photonics*, vol. 1, no. 2, pp. 106–114, 2007.
Referenced in page(s): 73

[82] V. Maselli, J. R. Grenier, S. Ho, and P. R. Herman, "Femtosecond laser written optofluidic sensor: Bragg grating waveguide evanescent probing of microfluidic channel," *Optics Express*, vol. 17, no. 14, pp. 11 719–11 729, 2009.
Referenced in page(s): 73, 75

[83] R. Osellame, H. J. Hoekstra, G. Cerullo, and M. Pollnau, "Femtosecond laser microstructuring: an enabling tool for optofluidic lab-on-chips," *Laser & Photonics Reviews*, vol. 5, no. 3, pp. 442–463, 2011.
Referenced in page(s): 73

[84] H. Zhang, S. M. Eaton, J. Li, A. H. Nejadmalayeri, and P. R. Herman, "Type II high-strength Bragg grating waveguides photowritten with ultrashort laser pulses," *Optics Express*, vol. 15, no. 7, pp. 4182–4191, 2007.
Referenced in page(s): 75, 113

[85] T. Erdogan and J. E. Sipe, "Radiation-mode coupling loss in tilted fiber phase gratings," *Optics Letters*, vol. 20, no. 18, pp. 1838–1840, 1995.
Referenced in page(s): 76

[86] T. Erdogan, "Cladding-mode resonances in short- and long-period fiber grating filters," *Journal of the Optical Society of America A*, vol. 14, no. 8, pp. 1760–1773, 1997.
Referenced in page(s): 76

[87] Y. Liu, L. Zhang, and I. Bennion, "Fabricating fibre edge filters with arbitrary spectral response based on tilted chirped grating structures," *Measurement Science and Technology*, vol. 10, no. 1, p. L1, 1999.
Referenced in page(s): 76

[88] A. M. Vengsarkar, P. J. Lemaire, J. B. Judkins, V. Bhatia, T. Erdogan, and J. E. Sipe, "Long-period fiber gratings as band-rejection filters," *Lightwave Technology, Journal of*, vol. 14, no. 1, pp. 58–65, 1996.
Referenced in page(s): 76

[89] J.-L. Archambault, L. Reekie, and P. S. Russell, "100% reflectivity Bragg reflectors produced in optical fibres by single excimer laser pulses," *Electronics Letters*, vol. 29, no. 5, pp. 453–455, 1993.
Referenced in page(s): 76

[90] B. Malo, D. C. Johnson, F. Bilodeau, J. Albert, and K. O. Hill, "Single-excimer-pulse writing of fiber gratings by use of a zero-order nulled phase mask: grating spectral response and visualization of index perturbations," *Optics Letters*, vol. 18, no. 15, pp. 1277–1279, 1993.
Referenced in page(s): 76

[91] K. Dolgaleva, A. Malacarne, P. Tannouri, L. A. Fernandes, J. R. Grenier, J. S. Aitchison, J. Azaña, R. Morandotti, P. R. Herman, and P. V. S. Marques, "Integrated optical temporal Fourier transformer based on a chirped Bragg grating waveguide," *Optics Letters*, vol. 36, no. 22, pp. 4416–4418, 2011.
Referenced in page(s): 80, 81, 82, 83, 89

[92] B. H. Kolner, "Space-time duality and the theory of temporal imaging," *Quantum Electronics, IEEE Journal of*, vol. 30, no. 8, pp. 1951–1963, 1994.
Referenced in page(s): 80

[93] Y. C. Tong, L. Y. Chan, and H. K. Tsang, "Fibre dispersion or pulse spectrum measurement using a sampling oscilloscope," *Electronics Letters*, vol. 33, no. 11, pp. 983–985, 1997.
Referenced in page(s): 80

[94] M. A. Muriel, J. Azaña, and A. Carballar, "Real-time Fourier transformer based on fiber gratings," *Optics Letters*, vol. 24, no. 1, pp. 1–3, 1999.
Referenced in page(s): 80

[95] F. Coppinger, A. S. Bhushan, and B. Jalali, "Photonic time stretch and its application to analog-to-digital conversion," *Microwave Theory and Techniques, IEEE Transactions on*, vol. 47, no. 7, pp. 1309–1314, 1999.
Referenced in page(s): 80

[96] J. Chou, Y. Han, and B. Jalali, "Adaptive RF-photonic arbitrary waveform generator," *Photonics Technology Letters, IEEE*, vol. 15, no. 4, pp. 581–583, 2003.
Referenced in page(s): 80

[97] D. R. Solli, J. Chou, and B. Jalali, "Amplified wavelength-time transformation for real-time spectroscopy," *Nature Photonics*, vol. 2, no. 1, pp. 48–51, 2008.
Referenced in page(s): 80

[98] M. H. Asghari, Y. Park, and J. Azaña, "Complex-field measurement of ultrafast dynamic optical waveforms based on real-time spectral interferometry," *Optics Express*, vol. 18, no. 16, pp. 16 526–16 538, 2010.
Referenced in page(s): 80

[99] S. Thomas, A. Malacarne, F. Fresi, L. Poti, and J. Azaña, "Fiber-Based Programmable Picosecond Optical Pulse Shaper," *Lightwave Technology, Journal of*, vol. 28, no. 12, pp. 1832–1843, 2010.
Referenced in page(s): 80

[100] J. Azaña, L. R. Chen, M. A. Muriel, and P. W. E. Smith, "Experimental demonstration of real-time Fourier transformation using linearly chirped fibre Bragg gratings," *Electronics Letters*, vol. 35, no. 25, pp. 2223–2224, 1999.
Referenced in page(s): 82

[101] L. Lepetit, G. Chériaux, and M. Joffre, "Linear techniques of phase measurement by femtosecond spectral interferometry for applications in spectroscopy," *Journal of the Optical Society of America B*, vol. 12, no. 12, pp. 2467–2474, 1995.
Referenced in page(s): 82

[102] Y. Park, M. Scaffardi, A. Malacarne, L. Potì, and J. Azaña, "Linear, self-referenced technique for single-shot and real-time full characterization of (sub-)picosecond optical pulses," *Optics Letters*, vol. 35, no. 15, pp. 2502–2504, 2010.
Referenced in page(s): 82

[103] K. W. DeLong and R. Trebino, "Improved ultrashort pulse-retrieval algorithm for frequency-resolved optical gating," *Journal of the Optical Society of America A*, vol. 11, no. 9, pp. 2429–2437, 1994.
Referenced in page(s): 82

[104] C. Iaconis and I. A. Walmsley, "Spectral phase interferometry for direct electric-field reconstruction of ultrashort optical pulses," *Optics Letters*, vol. 23, no. 10, pp. 792–794, 1998.
Referenced in page(s): 82

[105] J. R. Grenier, L. A. Fernandes, J. S. Aitchison, P. V. S. Marques, and P. R. Herman, "Femtosecond laser fabrication of phase-shifted Bragg grating waveguides in fused silica," *Optics Letters*, vol. 37, no. 12, pp. 2289–2291, 2012.
Referenced in page(s): 86, 87, 89

[106] R. Zengerle and O. Leminger, "Phase-shifted Bragg-grating filters with improved transmission characteristics," *Lightwave Technology, Journal of*, vol. 13, no. 12, pp. 2354–2358, 1995.
Referenced in page(s): 85

[107] J. R. Grenier, L. A. Fernandes, P. V. S. Marques, J. S. Aitchison, and P. R. Herman, "Optical Circuits in Fiber Cladding: Femtosecond laser-written Bragg Grating Waveguides," in *CLEO:2011 - Laser Applications to Photonic Applications*. Optical Society of America, 2011, p. CMZ1.
Referenced in page(s): 89

[108] L. A. Fernandes, J. R. Grenier, P. R. Herman, J. S. Aitchison, and P. V. S. Marques, "Femtosecond Laser Writing of Phase-Shifted Bragg Grating Waveguides in Fused Silica," in *Femtosecond Laser Microfabrication*. Optical Society of America, 2009, p. LMTuC5.
Referenced in page(s): 89

[109] N. K. Berger, B. Levit, B. Fischer, M. Kulishov, D. V. Plant, and J. Azaña, "Temporal differentiation of optical signals using a phase-shifted fiber Bragg grating," *Optics Express*, vol. 15, no. 2, pp. 371–381, 2007.
Referenced in page(s): 89

[110] Y. Bellouard, T. Colomb, C. Depeursinge, M. Dugan, A. A. Said, and P. Bado, "Nanoindentation and birefringence measurements on fused silica specimen exposed to low-energy femtosecond pulses," *Optics Express*, vol. 14, no. 18, pp. 8360–8366, 2006.
Referenced in page(s): 92, 111

[111] M. Ams, G. D. Marshall, and M. J. Withford, "Study of the influence of femtosecond laser polarisation on direct writing of waveguides," *Optics Express*, vol. 14, no. 26, pp. 13 158–13 163, 2006.
Referenced in page(s): 92

[112] P. Yang, G. R. Burns, J. Guo, T. S. Luk, and G. A. Vawter, "Femtosecond laser-pulse-induced birefringence in optically isotropic glass," *Journal of Applied Physics*, vol. 95, p. 5280, 2004.
Referenced in page(s): 92, 95

[113] E. Bricchi, B. G. Klappauf, and P. G. Kazansky, "Form birefringence and negative index change created by femtosecond direct writing in transparent materials," *Optics Letters*, vol. 29, no. 1, pp. 119–121, 2004.
Referenced in page(s): 92, 111

[114] R. S. Taylor, C. Hnatovsky, E. Simova, P. P. Rajeev, D. M. Rayner, and P. B. Corkum, "Femtosecond laser erasing and rewriting of self-organized planar nanocracks in fused silica glass," *Optics Letters*, vol. 32, no. 19, pp. 2888–2890, 2007.
Referenced in page(s): 92

[115] G. Cheng, K. Mishchik, C. Mauclair, E. Audouard, and R. Stoian, "Ultrafast laser photoinscription of polarization sensitive devices in bulk silica glass," *Optics Express*, vol. 17, no. 12, pp. 9515–9525, 2009.
Referenced in page(s): 92

[116] W. Cai, A. R. Libertun, and R. Piestun, "Polarization selective computer-generated holograms realized in glass by femtosecond laser induced nanogratings," *Optics Express*, vol. 14, no. 9, pp. 3785–3791, 2006.
Referenced in page(s): 92

[117] D. G. Papazoglou and M. J. Loulakis, "Embedded birefringent computer-generated holograms fabricated by femtosecond laser pulses," *Optics Letters*, vol. 31, no. 10, pp. 1441–1443, 2006.
Referenced in page(s): 92

[118] M. Beresna and P. G. Kazansky, "Polarization diffraction grating produced by femtosecond laser nanostructuring in glass," *Optics Letters*, vol. 35, no. 10, pp. 1662–1664, 2010.
Referenced in page(s): 92

[119] L. Ramirez, M. Heinrich, S. Richter, F. Dreisow, R. Keil, A. V. Korovin, U. Peschel, S. Nolte, and A. Tünnermann, "Tuning the structural properties of femtosecond-laser-induced nanogratings," *Applied Physics A: Materials Science and Processing*, vol. 100, no. 1, pp. 1–6, 2010.
Referenced in page(s): 92

[120] Y. Shimotsuma, M. Sakakura, P. G. Kazansky, M. Beresna, J. Qiu, K. Miura, and K. Hirao, "Ultrafast Manipulation of Self-Assembled Form Birefringence in Glass," *Advanced Materials*, vol. 22, no. 36, pp. 4039–4043, 2010.
Referenced in page(s): 92, 111

[121] M. Lobino and J. L. O'Brien, "Entangled photons on a chip," *Nature*, vol. 469, no. 7328, pp. 43–44, 2011.
Referenced in page(s): 92, 112

[122] G. D. Marshall, A. Politi, J. C. Matthews, P. Dekker, M. Ams, M. J. Withford, and J. L. O'Brien, "Laser written waveguide photonic quantum circuits," *Optics Express*, vol. 17, no. 15, pp. 12 546–12 554, 2009.
Referenced in page(s): 92, 103, 112

[123] L. Sansoni, F. Sciarrino, G. Vallone, P. Mataloni, A. Crespi, R. Ramponi, and R. Osellame, "Polarization entangled state measurement on a chip," *Physical Review Letters*, vol. 105, no. 20, p. 200503, 2010.
Referenced in page(s): 92, 103, 111, 112

[124] A. Politi, M. J. Cryan, J. G. Rarity, S. Yu, and J. L. O'Brien, "Silica-on-silicon waveguide quantum circuits," *Science*, vol. 320, no. 5876, pp. 646–649, 2008.
Referenced in page(s): 92

[125] S. Betti, G. De Marchis, and E. Iannone, "Polarization modulated direct detection optical transmission systems," *Lightwave Technology, Journal of*, vol. 10, no. 12, pp. 1985–1997, 1992.
Referenced in page(s): 93, 103

[126] C. H. Bennett and G. Brassard, "Quantum cryptography: Public key distribution and coin tossing," in *Proceedings of IEEE International Conference on Computers, Systems and Signal Processing*, vol. 175. Bangalore, India, 1984.
Referenced in page(s): 93, 103

[127] J. L. O'Brien, A. Furusawa, and J. Vuckovic, "Photonic quantum technologies," *Nature Photonics*, vol. 3, no. 12, pp. 687–695, 2009.
Referenced in page(s): 93, 112

[128] J. L. O'Brien, "Optical quantum computing," *Science*, vol. 318, no. 5856, p. 1567, 2007.
Referenced in page(s): 93

[129] W. J. Chen, S. M. Eaton, H. Zhang, and P. R. Herman, "Broadband directional couplers fabricated in bulk glass with high repetition rate femtosecond laser pulses," *Optics Express*, vol. 16, no. 15, pp. 11 470–11 480, 2008.
Referenced in page(s): 105, 110

[130] R. Hereth and G. Schiffner, "Broad-band optical directional couplers and polarization splitters," *Lightwave Technology, Journal of*, vol. 7, no. 6, pp. 925–930, 1989.
Referenced in page(s): 110

[131] L. Zhang, C. Yang, C. Yu, T. Luo, and A. E. Willner, "PCF-based polarization splitters with simplified structures," *Lightwave Technology, Journal of*, vol. 23, no. 11, p. 3558, 2005.
Referenced in page(s): 110

[132] Y. Yue, L. Zhang, J. Y. Yang, R. G. Beausoleil, and A. E. Willner, "Silicon-on-insulator polarization splitter using two horizontally slotted waveguides," *Optics Letters*, vol. 35, no. 9, pp. 1364–1366, 2010.
Referenced in page(s): 110

[133] A. M. Streltsov and N. Borrelli, "Study of femtosecond-laser-written waveguides in glasses," *Journal of the Optical Society of America B*, vol. 19, no. 10, pp. 2496–2504, 2002.
Referenced in page(s): 111, 115

[134] A. Rodenas, L. M. Maestro, M. O. Ramirez, G. A. Torchia, L. Roso, F. Chen, and D. Jaque, "Anisotropic lattice changes in femtosecond laser inscribed Nd^{3+}:MgO:$LiNbO_3$ optical waveguides," *Journal of Applied Physics*, vol. 106, no. 1, p. 013110, 2009.
Referenced in page(s): 111

[135] J. Siebenmorgen, K. Petermann, G. Huber, K. Rademaker, S. Nolte, and A. Tünnermann, "Femtosecond laser written stress-induced Nd: Y3 Al5 O12 (Nd: YAG) channel waveguide laser," *Applied Physics B: Lasers and Optics*, vol. 97, no. 2, pp. 251–255, 2009.
Referenced in page(s): 111, 115

[136] B. Poumellec, L. Sudrie, M. Franco, B. Prade, and A. Mysyrowicz, "Femtosecond laser irradiation stress induced in pure silica," *Optics Express*, vol. 11, no. 9, pp. 1070–1079, 2003.
Referenced in page(s): 112

[137] V. Kudriašov, E. Gaižauskas, and V. Sirutkaitis, "Birefringent modifications induced by femtosecond filaments in optical glass," *Applied Physics A: Materials Science and Processing*, vol. 93, no. 2, pp. 571–576, 2008.
Referenced in page(s): 112

[138] J. O. Owens, M. A. Broome, D. N. Biggerstaff, M. E. Goggin, A. Fedrizzi, T. Linjordet, M. Ams, G. D. Marshall, J. Twamley, M. J. Withford, and A. G. White, "Two-photon quantum walks in an elliptical direct-write waveguide array," *New Journal of Physics*, vol. 13, p. 075003, 2011.
Referenced in page(s): 112

[139] L. Sansoni, F. Sciarrino, G. Vallone, P. Mataloni, A. Crespi, R. Ramponi, and R. Osellame, "Two-Particle Bosonic-Fermionic Quantum Walk via Integrated Photonics," *Physical Review Letters*, vol. 108, no. 1, p. 010502, 2012.
Referenced in page(s): 112

[140] L. A. Fernandes, J. R. Grenier, P. R. Herman, J. S. Aitchison, and P. V. S. Marques, "Femtosecond laser fabrication of birefringent directional couplers as polarization beam splitters in fused silica," *Optics Express*, vol. 19, no. 13, pp. 11 992–11 999, 2011.
Referenced in page(s): 112, 117, 123

[141] L. A. Fernandes, J. R. Grenier, P. R. Herman, J. S. Aitchison, and P. V. S. Marques, "Femtosecond laser writing of waveguide retarders in fused silica for polarization control in optical circuits," *Optics Express*, vol. 19, no. 19, pp. 18 294–18 301, 2011.
Referenced in page(s): 112, 117, 120, 123

[142] M. M. Milosevic, P. S. Matavulj, B. D. Timotijevic, G. T. Reed, and G. Z. Mashanovich, "Design Rules for Single-Mode and Polarization-Independent Silicon-on-Insulator Rib Waveguides Using Stress Engineering," *Lightwave Technology, Journal of*, vol. 26, no. 13, pp. 1840–1846, 2008.
Referenced in page(s): 112

[143] D.-X. Xu, P. Cheben, D. Dalacu, A. Delâge, S. Janz, B. Lamontagne, M.-J. Picard, and W. N. Ye, "Eliminating the birefringence in silicon-on-insulator ridge waveguidesby use of cladding stress," *Optics Letters*, vol. 29, no. 20, pp. 2384–2386, 2004.
Referenced in page(s): 112

[144] L. A. Fernandes, J. R. Grenier, P. R. Herman, J. S. Aitchison, and P. V. S. Marques, "Femtosecond laser writing of polarization devices for optical circuits in glass," in *Proceedings of SPIE*, vol. 8247, 2012, p. 82470M.
Referenced in page(s): 113

[145] B. Poumellec, M. Lancry, J.-C. Poulin, and S. Ani-Joseph, "Non reciprocal writing and chirality in femtosecond laser irradiated silica," *Optics Express*, vol. 16, no. 22, pp. 18 354–18 361, 2008.
Referenced in page(s): 114

[146] M. Ams, G. Marshall, D. Spence, and M. Withford, "Slit beam shaping method for femtosecond laser direct-write fabrication of symmetric waveguides in bulk glasses," *Optics Express*, vol. 13, no. 15, pp. 5676–5681, 2005.
Referenced in page(s): 122

[147] G. Cerullo, R. Osellame, S. Taccheo, M. Marangoni, D. Polli, R. Ramponi, P. Laporta, and S. D. Silvestri, "Femtosecond micromachining of symmetric waveguides at 1.5 µm by astigmatic beam focusing," *Optics Letters*, vol. 27, no. 21, pp. 1938–1940, 2002.
Referenced in page(s): 122

[148] I. H. Malitson, "Interspecimen comparison of the refractive index of fused silica," *Journal of the Optical Society of America*, vol. 55, no. 10, pp. 1205–1208, 1965.
Referenced in page(s): 137, 138

[149] C. Z. Tan, "Determination of refractive index of silica glass for infrared wavelengths by IR spectroscopy," *Journal of Non-Crystalline Solids*, vol. 223, no. 1, pp. 158–163, 1998.
Referenced in page(s): 138